Dear Author,

Please correct your galley proofs carefully and return them no more than four days after the page proofs have been received.

Please limit corrections to errors already in the text; cost incurred for any further changes or additions will be charged to the author, unless such changes have been agreed upon by the editor.

The editors reserve the right to publish your article without your corrections if the proofs do not arrive in time.

Note that the author is liable for damages arising from incorrect statements, including misprints.

Please note any queries that require your attention. These are indicated with a Q in the PDF and a question at the end of the document.

Reprints may be ordered by filling out the accompanying form.

Return the reprint order form by fax or by e-mail with the corrected proofs, to Wiley-VCH : **advmat@wiley.com**

To avoid commonly occurring errors, **please ensure that the following important items are correct** in your proofs (please note that once your article is published online, no further corrections can be made):

- **Names** of all authors present and spelled correctly

- **Titles** of authors correct (Prof. or Dr. only: please note, Prof. Dr. is not used in the journals)

- **Addresses** and **postcodes** correct

- **E-mail address** of corresponding author correct (current email address)

- **Funding bodies** included and grant numbers accurate

- **Title** of article OK

- All **figures** included

- **Equations** correct (symbols and sub/superscripts)

Corrections should be made directly in the PDF file using the PDF annotation tools. If you have questions about this, please contact the editorial office. The corrected PDF and any accompanying files should be uploaded to the journal's Editorial Manager site.

WILEY

Author Query Form

Dear Author,

During the copyediting of your manuscript the following queries arose.

Please refer to the query reference callout numbers in the page proofs and respond to each by marking the necessary comments using the PDF annotation tools.

Please remember illegible or unclear comments and corrections may delay publication.

Many thanks for your assistance.

Query No.	Description	Remarks
Q1	Please confirm that forenames/given names (blue) and surnames/family names (vermilion) have been identified correctly.	
Q2	Biographies should be around 100 words and must include a concise career overview and current research interests. Family details, awards, patents, publications, etc., shouldn't be added.	
Q3	Please provide city name and postal code in affiliation 2.	
Q4	Please confirm that all panels in all figures (including the ToC) are your own, original work (not previously published), or please confirm that you have obtained permission to use them here and provide the full copyright information for each individual image as follows: Reproduced with permission.[Ref.] Copyright 'Year', 'Publisher' or in case of an open access article: Reproduced under the terms of the Creative Commons 'License information'.[Ref] Copyright 'year', 'The Authors or Company', published by 'Publisher'.	
Q5	Please note that footnotes are not permitted in table headings. So, they have been moved to the first column in Tables 3–5 and 8. Please check that this is OK or move to a more appropriate place.	

Author: Please confirm that Funding Information has been identified correctly.

Please confirm that the funding sponsor list below was correctly extracted from your article: that it includes all funders and that the text has been matched to the correct FundRef Registry organization names. If a name was not found in the FundRef registry, it may not be the canonical name form, it may be a program name rather than an organization name, or it may be an organization not yet included in FundRef Registry. If you know of another name form or a parent organization name for a "not found" item on this list below, please share that information.

| FundRef Name	FundRef Organization Name
Extramural Research Funding	
Spanish Ministry of Economy and Competitiveness	Ministerio de Economía, Industria y Competitividad, Gobierno de España
Generalitat Valenciana	Generalitat Valenciana

Heterogeneous Catalysis

A. Dhakshinamoorthy,* A. M. Asiri,
H. Garcia* 1900617

2D Metal-Organic Frameworks as Multifunctional Materials in Heterogeneous Catalysis and Electro/Photocatalysis
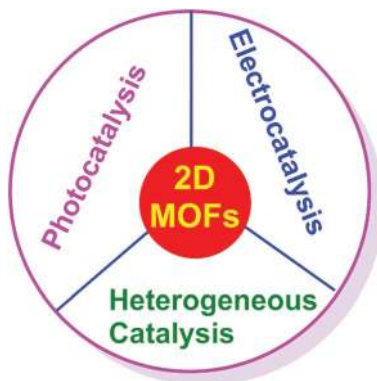
This review illustrates that available data indicate that 2D MOFs often exhibit higher catalytic activity compared to their respective 3D solids due to the absence of diffusion limitation to reach active sites, easy accessibility to active sites, and high population of active sites.

2D Metal-Organic Frameworks as Multifunctional Materials in Heterogeneous Catalysis and Electro/Photocatalysis

Amarajothi Dhakshinamoorthy, * Abdullah M. Asiri,* and *Hermenegildo Garcia**

Metal-organic frameworks (MOFs) are composed of particles with 3D geometry and are currently among the most widely studied heterogeneous catalysts. To further increase their activity, one of the recent trends is to develop related 2D materials with a high aspect ratio derived from a large lateral size and a small thickness. The present review summarizes the use of these 2D MOFs as catalysts, electrocatalysts, and photocatalysts illustrating the advantages of these 2D materials compared to analogous 3D MOFs. The state of the art is summarized in tables and, when possible, pertinent turnover numbers and frequencies. This enhanced activity of 2D MOFs derives from the accessibility of the active sites, the presence of a higher density of defects, and exchangeable coordination positions around MOFs, as well as from their ability to form thin films on electrodes or surfaces. The importance of providing convincing evidence of the stability of 2D MOFs under reaction conditions and general characterization data of the used 2D material after catalysis is highlighted. The last part of the review contains views regarding challenges in the field and new developments that can be expected.

1. Introduction

Metal-organic frameworks (MOFs) in which the structure encompasses metal nodes connected with rigid multipodal organic linkers are one type of crystalline porous material[1–4] that has become among the preferred heterogeneous catalysts for liquid phase reactions[5–16] and other reaction types.[17–19] The reasons for this wide use of MOFs in catalysis derive from a combination of positive factors, including a large versatility in the synthesis,[20] the possibility of postsynthetic modification,[21]

the large proportion of transition metals in their composition, the possibility of preparing MOFs with virtually any transition metal, the large surface area[22,23] and pore dimensions, and large variety of structures reported so far.[24] The deep knowledge on the formation of these materials and the possibility to design[25] one specific MOF that is suited for a given catalytic application has also allowed the control of the growth of the material,[26] the average particle size, the crystallinity, and the presence of structural defects.[27–29] In this regard, the presence of modulators during the synthesis combined with the understanding on the reversibility of the metal–ligand bonds during the synthesis has become a useful tool for controlling the crystallinity and the generation of defective sites.[30–32]

Connected with the control in the synthesis of MOFs, one of the possibilities that is currently attracting much interest are procedures for arresting the growth of the crystals in a 3D structure, allowing the synthesis of lamellar materials with 2D morphology and high lateral area-to-thickness aspect ratio.[33–37] It should be noted that the concept of 2D MOFs not only includes one-atom thick, single layered lamellar MOFs, but also those crystals with a high lateral to thickness aspect ratio crystallites that may still contain pores between the upper and bottom surfaces.

In a recent review, the methodology and strategies for the preparation of these 2D MOFs have been described,[34] particularly in comparison with the 3D analogs. **Scheme 1** illustrates various methods reported in the literature for the preparation of 2D MOFs using either top-down or bottom-up methodology. Authors are encouraged to refer to a dedicated review on the synthesis of 2D MOFs for a deep coverage of the preparation of these materials.[34]

2D MOFs may exhibit considerable advantages with respect to the 3D counterparts derived from the specific features of 2D morphology.[38–42] Specifically, fully exfoliated single layers of a 2D MOF will make every active site on its surface available to substrates and reagents without the diffusion limitations arising from the passage of these molecules through the internal pores in 3D materials. In addition to accessibility that can increase the catalytic activity with respect to 3D materials, other favorable features of 2D MOFs are that they can be considered as having defective, exchangeable coordination positions at the metal nodes that otherwise would be occupied by the linkers forming the 3D structure. The presence of defects

Prof. A. Dhakshinamoorthy
School of Chemistry
Madurai Kamaraj University
Madurai 625 021, Tamil Nadu, India
E-mail: admguru@gmail.com
Prof. A. M. Asiri, Prof. H. Garcia
Center of Excellence in Advanced Materials Research
King Abdulaziz University
Saudi Arabia
E-mail: hgarcia@qim.upv.es
Prof. H. Garcia
Departamento de Quimica and Instituto Universitario
de Tecnologia Quimica (CSIC-UPV)
Universitat Politecnica de Valencia
Av. De los Naranjos s/n, 46022 Valencia, Spain

The ORCID identification number(s) for the author(s) of this article can be found under https://doi.org/10.1002/adma.201900617.

and coordinatively unsaturated coordination positions around the metal ions are generally prerequisites to observe catalytic activity. Therefore, 2D MOFs should be, in principle, more efficient catalyst than 3D analogs that, however, are already considered highly efficient catalysts. In addition, the 2D morphology is especially suited for the formation of films[43,44] and coatings on surfaces rather than large 3D particles. The 2D morphology increases adhesion to the surface and increases the proportion of contact area between the 2D MOF and the substrate. Formation of these films is highly beneficial for certain applications such as electrocatalysis where conductive inert electrode has to be in contact with the electrocatalyst and photocatalysis where light penetration in opaque powders is limited to a few microns.[45,46] In electrocatalysis, thin films exhibit lower electrical resistance and considerably favor electron transport phenomena with the conductive electrode. In the case of photocatalysis, high efficiency in light harvesting requires that all the photoresponsive units should be exposed to the photons. Therefore, it is necessary to prepare films with a thickness commensurate with the light penetration depth. Since electro- and photocatalysis are gaining importance in the context of renewable electricity, conversion and utilization of natural sunlight as a primary energy source, the use of 2D MOFs appears as more convenient than the 3D analogs. **Table 1** summarizes the list of notable differences between 2D and 3D MOFs from the perspective of catalysis. Concerning Table 1, it should be commented that the chemical and thermal stability of 2D MOFs is frequently similar to those of their 3D analogs. The reason for this similar stability is the nature and strength of the coordinative metal–linker bonds that are the same in 3D than in 2D MOFs. Regarding stability, particularly respect to the possible benefits of the 2D morphology, a point that should be always addressed when using 2D materials as heterogeneous catalysts is possible variations in thickness under the reaction conditions, due to the occurrence of stacking and restructuring of the 2D material.

Another driver justifying the current interest of 2D materials in catalysis is the advent of graphenes as large area supports or as metal-free catalysts.[47–51] Graphenes, being a single one-atom-thick layer of carbons in hexagonal geometry, have been shown to establish strong metal–support interactions, and in this way, graphenes are good materials for supporting catalytically active nanoparticles (NPs).[52] Following this lead, there are also examples showing that other 2D materials including MOFs, besides being materials of intrinsic catalytic activity due to their metal content, can act as supports for metal NPs.[53] Also, in the field of electro- and photocatalysis, 2D materials such as metal dichalcogenides[54–56] and graphitic carbon nitride[57,58] have appeared as alternatives for the use of costly noble metals. It is very likely that 2D MOFs can also compete with noble metals as electrocatalysts and with semiconductors in photocatalysis. Although the use of 2D materials has been motivated basically by the wide availability of graphenes and related materials,[59,60] it was also in the related field of zeolites where the advantages of 2D materials were first demonstrated.[61] Zeolites are porous crystalline aluminosilicates that have many structural similarities to MOFs but with very different chemical composition. In the case of zeolites and due to the limitation in the available pore size in these materials, exfoliation and delamination of some zeolite precursors was found to result in the preparation of

Amarajothi Dhakshinamoorthy obtained his Ph.D. degree in 2009 from Madurai Kamaraj University, Tamil Nadu, India. Later, he worked as a postdoctoral researcher with Prof. Hermenegildo Garcia at the Technical University of Valencia for 4 years. Then, he returned to India and joined as UGC-Assistant Professor in June 2013 at School of Chemistry, Madurai Kamaraj University. His research interests include catalysis by metal-organic frameworks and graphene-related materials.

Abdullah M. Asiri received Ph.D. degree from University of Wales, College of Cardiff, UK, in 1995. He is the Head of the Chemistry Department at King Abdulaziz University since October 2009 and he is the founder and the Director of the Center of Excellence for Advanced Materials Research. He is a professor of organic photochemistry.

Hermenegildo Garcia is full Professor at the Instituto de Tecnología Química of the Technical University of Valencia and Honorary Adjunct Professor at the Center of Excellence in Advanced Materials Research of King Abdulaziz University. Prof. Garcia has been active in the field of heterogeneous catalysis working with porous catalysts and nanoparticles.

layered zeolites with accessible acid sites and without exhibiting the diffusion restrictions taking place in related 3D solids.[62] These precedents can anticipate what is expected to be the development of 2D MOFs in the field of heterogeneous catalysis. **Scheme 2** illustrates some of the best-studied 2D solids in heterogeneous catalysis, photocatalysis, and electrocatalysis that have shown superior performance compared to their analogous 3D materials derived from their unique morphological features.

In recent years, a series of reviews has been published on 2D MOF nanosheets[63–67] that specifically focused on synthetic
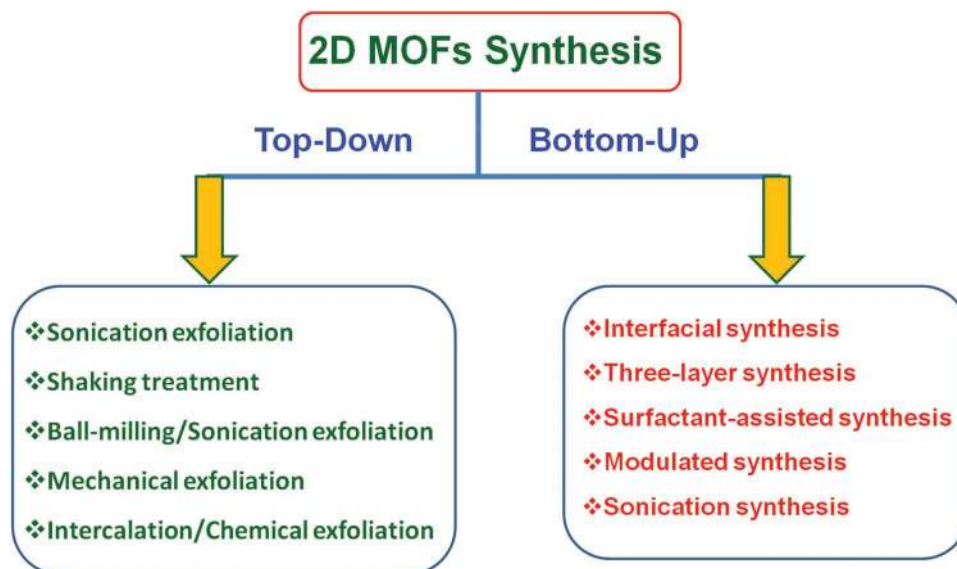
Scheme 1. General procedures for the synthesis of 2D MOFs either by top-down or bottom-up strategies.

methods including bottom-up and top-down approaches, applications of 2D MOFs in various fields such as CO_2 separation, as well as in photonic and electronic devices. There is, however, a need for a dedicated review emphasizing the multifunctional role of 2D MOFs in catalysis, electrocatalysis and photocatalysis.

Hence, the present manuscript summarizes the current state of the art in the use of 2D MOFs as heterogeneous catalysts and in electro- and photocatalysis. The structure and composition of these MOFs will be described briefly to show the nature of the active sites. **Scheme 3** summarizes possible active sites in 2D MOFs that can be responsible for promoting catalysis, photocatalysis and electrocatalysis. The main emphasis of this review is describing the activity of these materials, specifically in comparison with the 3D analog and in a few cases also with 1D counterparts and with related homogeneous catalysts. Examples will be given showing that, as anticipated, enhancement in the catalytic activity occurs as a consequence of the 2D morphology granting accessibility of reagents and promoting the

presence of active sites on the material. After general considerations on the synthesis of 2D MOFs using top-down and bottom-up approaches and the various spectroscopic and microscopic characterization tools for the 2D MOFs, the main body of the present article summarizes the current state of the art grouped in three main subsections covering the catalytic, electrocatalytic and photocatalytic activity of these materials. The last section summarizes the review and contains our viewpoint on future development of 2D MOFs in catalysis.

## 2. Synthesis and Characterization of MOF Nanosheets

As sketched in Scheme 1, there are two general strategies for the synthesis of 2D MOF nanosheets, namely, the top-down and the bottom-up methods. The top-down approach frequently involves exfoliation of layered bulk MOFs, breaking weak interlayer interactions such as van der Waals forces and hydrogen bonding within MOFs.[38] The bottom-up methodology is based on the synthesis of 2D MOF nanosheets from metal ions and organic linkers, arresting the growth of MOFs along the vertical

Table 1. Comparison between 2D and 3D MOFs ~~from catalysis~~ perspective.

Properties	2D MOFs	3D MOFs
Thickness	Nanometers	Nanometers to micrometers
Diffusion	Can be facile	May be difficult in some cases
Reaction rate	Order of 10^3 to 10^6	Order of 10^2 to 10^3
Accessible of active sites	Much easier	May be difficult
Surface area	Range of 200–400 $m^2\,g^{-1}$	>5000 $m^2\,g^{-1}$
Pore volume	Less than 1 nm	More than 1 nm
Postsynthetic modification	Possible	Possible
Chemical stability	Stable	Stable
Thermal stability	Stable	Stable
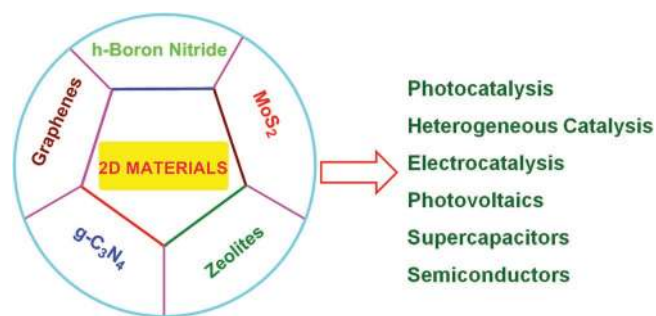
Scheme 2. Some widely studied 2D materials finding application in various fields.
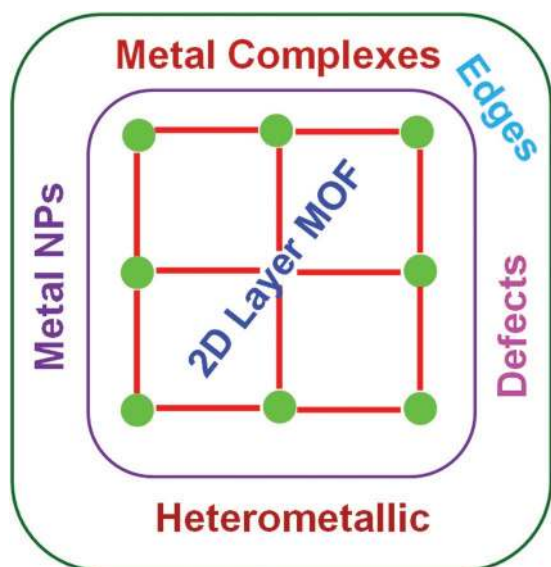
Scheme 3. Possible sites that can be present in 2D MOFs and can be active in catalysis, photocatalysis and electrocatalysis.

direction. For the purpose of the present review on the application of 2D MOFs in catalysis, the following sections will briefly summarize various methods for the synthesis of 2D MOF nanosheets, but the readers are referred to the existing reviews dedicated exclusively on detailed synthesis procedures.[34,36,63,68]

2.1. Top-Down Synthesis

The exfoliation method breaks the weak interlayer interaction to disassemble layered bulk 2D MOFs by mechanical forces, typically ultrasounds in a liquid medium, into a single or few-layered MOF nanosheets. In one of the examples, 2D $[Cu_2Br(IN)_2]_n$ (IN = isonicotinato) nanosheets were synthesized by breaking the interlayer π–π stacking with ultrasounds.[69] The successful formation of 2D MOFs was confirmed by atomic force microscopy (AFM) images which indicated a homogeneous dispersion of 2D nanosheets with a thickness of 5 ± 0.15 Å. This value was in good agreement with the theoretical thickness of the single atomic layer of $[Cu_2Br(IN)_2]_n$.

Two mixed-valence Fe-MOF [Fe(II)/Fe(III)] nanosheets were prepared by delaminating their bulk MOFs through sonication for 15 min in methanol resulting in the formation of nanosheets with a thickness of 7 nm.[70]

In some special cases, bulk MOFs can be delaminated by strong shaking. For example, ultrathin 2D $[Cu(bpy)_2(OTf)_2]$ (bpy = 4,4′-bipyridine; OTf = trifluoromethanesulfonate) MOF nanosheets with a thickness of 4–5 nm were obtained by shaking the solid in acetone, the resulting 2D Cu MOF nanosheets being larger and thinner than the analogous sample prepared by ultrasonication.[71]

Recently, Yang and co-workers have used wet ball milling and sonication as an effective approach for exfoliation of 2D $Zn_2(bim)_4$ MOFs (bim = benzimidazole).[38] The experimental results indicated that the thickness of $Zn_2(bim)_4$ nanosheet was 1.12 nm. In addition, ▭ image showed the formation

of ultrathin nanosheets. However, this method has some limitations. The exfoliated nanosheets are not stable either under the reaction conditions or upon storage due to the possibility of restacking. Further, the low yield of 2D MOFs is another drawback for practical applications. Hence, it is extremely important to develop further methodologies with adequate stabilization to overcome these issues in near future.

2.2. Bottom-Up Synthesis

This strategy is opposite and complementary to the above approach. The bottom-up method corresponds to the assembly of 2D MOF nanosheets from the respective metal ions and linkers. One of the fundamental challenges in this method is to selectively control the growth direction of the MOF crystals and especially to restrict the growth in the vertical direction.

One of the strategies often used under this category is called interfacial synthesis which involves the use of liquid/liquid or liquid/air interface to control the growth of MOF nanosheets. In one of these examples, the synthesis of nickel bis(dithiolene) nanosheets was achieved by reaction of nickel(II) acetate and benzenehexathiol at the liquid–air interface.[72] A thin layer of ethyl acetate solution containing benzenehexathiol was spread onto the surface of the aqueous solution containing nickel(II) acetate. The nanosheets were formed at the liquid–air interface upon evaporation of ethyl acetate. Scanning tunneling microscopy indicated the hexagonal pattern of single-layer nanosheets possessing a height of 0.6 nm. Recently, Gascon and co-workers have reported a strategy to obtain CuBDC nanosheets involving three-layer synthesis in high yield.[39] The synthesis medium consisted of three liquid layers prepared by vertically aligning a mixture of DMF and acetonitrile in different ratios. Interestingly, SEM, and AFM images showed the square-shape CuBDC nanosheets having lateral dimensions of 0.5–4 µm with the thicknesses range between 5 and 25 nm.

In a different methodology, a surfactant-assisted synthesis has also been reported for the preparation of ultrathin 2D MOF nanosheets with less than 10 nm thickness.[41] The key role of the surfactant is not only to control the growth of the MOFs along vertical direction, but, simultaneously assistance of MOF nanosheet dispersion in the liquid phase. As an example, Zn-TCPP (TCPP: tetrakis(4-carboxyphenyl)porphyrin) MOF was formed by coordination of $Zn_2(COO)_4$ paddlewheel metal nodes with four TCPP ligands.[73] A conventional synthesis in the absence of surfactant resulted in bulk Zn-TCPP crystals. In contrast, the use of poly(vinylpyrrolidone) as surfactant provided ultrathin Zn-TCPP nanosheets. The poly(vinylpyrrolidone) was able to preferentially attach over the surface of the MOFs by stabilizing the Zn-TCPP nanosheets, thwarting their growth along the vertical direction. AFM measurements showed the thickness of the Zn-TCPP nanosheets was 7.6 ± 2.6 nm.

It should be noted that the concept of surfactant in this bottom-up approach for the synthesis of 2D MOFs is frequently taken broadly, including in some cases ligand molecules able to coordinate with metal ions. Thus, in another precedent, MOF nanosheets were prepared by using bpy ligands (bpy = 4,4′-bipyridine) as surfactants.[74,75] The experimental results have shown that bpy molecules are pillared between the MOF

**ADVANCED
SCIENCE NEWS**

www.advancedsciencenews.com

**ADVANCED
MATERIALS**

www.advmat.de

nanosheets with uniform square-like morphology and the thickness of the nanosheets were around 43 nm. Similarly, Cu-MOF nanosheets were also reported using pyridine[76] as a kind of pillar molecule and in another precedent Hf-MOF nanosheets were prepared with the assistance of formic acid as a capping agent.[77] It was believed that these small molecules behave similarly as that of poly(vinylpyrrolidone) by binding on the surface of MOFs, impeding the growth of the crystallites along the vertical direction. In any case, care must be taken during the synthesis that these molecules should not block the active sites by strong coordination with the metal ions.

Template-assisted synthesis is another strategy reported for the synthesis of 2D MOFs. This method involves the in situ nucleation and growth of ultrathin 2D MOF nanosheets on the surface of certain supports.[78,79] One of the merits of this strategy is to achieve MOF nanosheets with increased macro/mesoporosity, improved conductivity or a growing number of catalytic centers. In one of these examples, template-assisted synthesis was employed for the fabrication of ultrathin 2D NiFe-MOF $(Ni_{0.8}\text{-}Fe_{0.2}(C_{12}H_6O_4)(H_2O)_4)$ nanosheets on Ni foam. AFM measurements of these nanosheets indicated their thickness of 3.5 nm.[80]

After having summarized some important methodologies for the synthesis of 2D MOFs, appropriate characterization techniques that are specifically used to determine the 2D morphology of the MOFs will be briefly commented. The reader is again referred to the existing literature for a more complete coverage of general characterization techniques.[34]

The best and more general technique to assess 2D morphology is microscopy. In transmission electron microscopy (TEM), the geometry of the particles and the layered configuration are imaged. Atomic force microscopy techniques with sub-nanometric vertical resolution can determine quantitatively the thickness of the sheets that can be correlated to the number of layers present in 2D MOF particles and their distribution. A high aspect ratio with nanometric thickness is a main feature for classifying the material as a 2D MOF. However, in some cases, no single layer 2D MOF is present in the material and, very commonly, 2D MOFs are formed by the stacking of several individual layers that are not agglomerated and that still may contain some internal porosity.

Due to the crystal structure, even though with a 2D configuration, XRD is still a very important technique for proving the ordering of the atoms within the nanosheets.[38] Crystallinity and strong metal linker interactions are two prerequisites for classifying these materials as MOFs. The former prerequisite can be determined by XRD.

Isothermal gas adsorption of 2D MOFs should determine the presence of residual internal surface area due to the presence of very minor porosity and considerably much larger contribution of external surface area. Because of the minimal porosity, standard surface area values for 2D MOFs range from 200 to 400 m^2 g^{-1}, which are significantly much lower values than the values that have been reported for 3D MOFs that can be well above 1000 m^2 g^{-1} and, in some cases, even above 3000 m^2 g^{-1} (see Table 1).

Relative to the catalytic activity, XPS analysis is a useful technique for quantifying the atomic ratio of the elements, the oxidation state of the metal components and the possible different environments for each of the metallic ions. Due to the 2D morphology of 2D MOFs and considering that XPS is a surface technique that probes only the most external layer in a material, the analytical data obtained in the present case by XPS should agree relatively well with the data from the bulk material, since most of the elements will now be monitored by XPS.

The coordination number and analysis of the coordination sphere of the metals present in the nodes or lattice satellite positions can be obtained, as in other types of solid materials, by analysis of the profiles of near edge (XANES) and extended fine structure (EXAFS) X-ray absorption. By exciting atomic core electrons, XANES and EXAFS provide unique information that can serve to determine the position of each metal in the framework and its oxidation state. These X-ray absorption techniques complement XRD and are particularly informative to determine the position of metals that are in small proportion in the material. Due to the selectivity, XANES and EXAFS can be applied to each of the different metals that could be present in the 2D MOF.

3. Applications of 2D MOFs

This section aims to narrate the recent developments in the use of 2D MOF nanosheets as solid materials in various fields like heterogeneous catalysis, electrocatalysis and photocatalysis. The available data are grouped based on the type of reaction that has been reported with 2D MOFs. Emphasis has been made to demonstrate the enhanced performance of 2D MOFs compared to their 3D bulk MOFs and their respective homogeneous catalysts by providing the conversion/selectivity data and TON/TOF values. Special attention has been paid to comment on the catalyst stability under the reaction conditions. Finally, the possible reasons for the enhanced activity of 2D MOFs compared to other solid/homogeneous catalysts are outlined with adequate evidence from characterization data.

3.1. Heterogeneous Catalysis

Table 2 summarizes the list of 2D MOFs that have been reported as heterogeneous solid catalysts for a wide range of reactions. This table aims to provide an overview of reactions that have been studied using 2D MOFs as catalysts, activity data and evidence to support their stability under the reaction conditions.

As noted earlier, with respect to conventional 3D bulk solids 2D materials present a larger accessibility of the active sites and also a larger density of defects and exchangeable coordination positions. These factors make 2D materials especially suited as heterogeneous catalysts.

In one of the earlier examples on the use of 2D MOFs as heterogeneous catalysts, Co^{2+} metal ions were reacted with 1,4-benzenedicarboxylate (BDC) ligands, resulting in the formation of a 2D MOF with $[Co_3(BDC)_3(DMF)_2(H_2O)_2]$ as the formula. The structure of the MOF is composed of CoO_6 octahedra coordinated in a plane to BDC ligands (**Figure 1**). The catalytic activity of this 2D Co MOF was studied for the oxidation of olefins using t-butylhydroperoxide (TBHP) as the

Table 2. List of 2D MOFs as heterogeneous solid catalysts, including preparation procedure, the reaction catalyzed, and activity and stability data.

2D MOFs	Preparation method	Reaction	Activity	Stability evidence	Ref.
$[Co_3(BDC)_3(DMF)_2(H_2O)_2]$	Hydrothermal	Oxidation of styrene	96% conversion	ICP, XRD, reuse	[81]
NUS-8(Zr)	Hydrothermal	Oxidation of thioanisole	100% conversion and selectivity	XRD, SEM, BET reuse	[82]
$[In_2(dpa)_3(1,10\text{-phen})_2]\cdot H_2O$	Hydrothermal	CO_2 cycloaddition with epoxides	91% conversion	reuse	[83]
$(NH_4)_3[In_3Cl_2(BPDC)_5]$	Solvothermal	CO_2 cycloaddition with epoxides	98% conversion (TON: 980)	XRD, reuse, leaching	[84]
$[Cu(ima)_2]_n$		N-Arylation of imidazole	86% yield	ICP-AES, XRD, reuse	[85]
$[Cd(PBA)(DMF)]\cdot DMF$	Solvothermal	Knoevenagel condensation	91% yield	XRD, reuse, leaching	[86]
$[Sc_2(pydc)_3\cdot(H_2O)_4]\cdot 5H_2O$	Hydrothermal	Cyanosilylation of benzaldehyde	99% conversion	Reuse, leaching	[87]
$[(Nd_2(TATMA)_2\cdot 4DMF\cdot 4H_2O]_n$		Knoevenagel condensation	95% yield	ICP, XRD, reuse	[88]
Fe-TPY-MOL	Solvothermal	Hydrosilylation of olefins	TON > 5000	reuse	[77]
$CoCl_2\cdot TPY\text{-}MOL$	Solvothermal	C–H borylation of methylarenes	42% yield	XRD, ICP-MS, reuse, leaching	[89]
Pd@ZIF-L	Assembly method	Hydrogenation of alkenes	78% conversion	Reuse, SEM, leaching	[90]
Au-1@Ni-NMOF	Surfactant-assisted	Reduction of 4-nitrophenol	Rate constant: 0.404 min^{-1}	TEM, reuse, leaching	[91]
Cu_2O@MOF	Hydrothermal	Huisgen 1,3-dipolar cycloaddition	98% yield	XRD, TEM, reuse	[92]
Au/Cu-TCPP(M) (M: Fe, Co)	Surfactant-assisted	Glucose oxidase and peroxidase-like activity	–	–	[93]
Ru/UiO-66	Surfactant-mediated	Hydrogenation of levulinic acid	TOF: 349 h^{-1}	Reuse, SEM, TEM	[94]

terminal oxidant.[81] The oxidation of styrene using $[Co_3(BDC)_3(DMF)_2(H_2O)_2]$ as catalyst with TBHP as oxidant at 75 °C resulted in the formation of styrene oxide with 45% selectivity at 96% conversion (**Scheme 4**). In comparison, under similar conditions, 1-octene, cyclooctene and cyclohexene reached 75%, 67%, and 90% conversions with 100, 100 and 95% selectivity toward their respective epoxides. *Cis*- and *trans*-stilbenes were also converted at 30% and 62% conversion to their respective epoxides with 100% selectivity. A quenching experiment with 2,6-di-tertbutyl-*p*-cresol as a radical scavenger largely inhibited the oxidation of styrene (5%) and cyclohexene (2%), confirming a radical reaction mechanism. ICP analysis determined the presence of less than 2% of the initial Co content of the solid in the solution. This small Co^{2+} amount leached to the solution was found to not be relevant regarding catalysis of the reaction. The catalyst was recycled three times with no decay in its activity. Comparison of the powder XRD patterns of the fresh 2D MOF with the three times used sample showed no

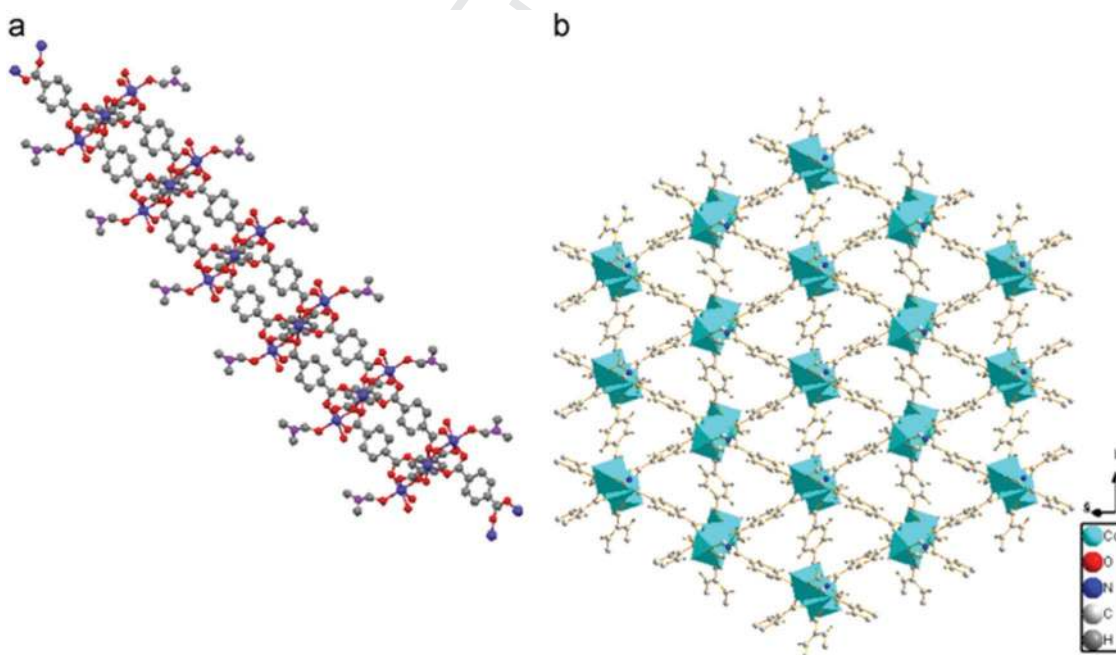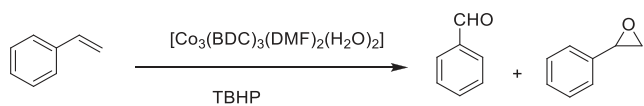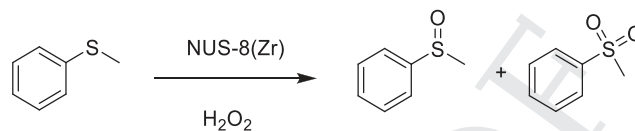**Figure 1.** Secondary building units along the [101] direction a) and 2D structure in the (101) plane of $[Co_3(BDC)_3(DMF)_2(H_2O)_2]$ with Co shown as the polyhedral linked together via BDC ligands b). Reproduced with permission.[81] Copyright 2015, Elsevier.

Scheme 4. Styrene oxidation by TBHP as the oxidant catalyzed by 2D Co MOF.

Scheme 5. Oxidation of thioanisole with H_2O_2 catalyzed by NUS-8(Zr).

differences, thus confirming the stability of the catalyst. It should be commented, however, that a comparison of the activity of 2D Co-MOF with that of the 3D analog was lacking and, therefore, the advantages of the 2D morphology due to easy accessibility of active sites by substrates and the higher density of active sites cannot be directly drawn.

The reaction between $ZrOCl_2\cdot 8H_2O$ or $HfCl_4$ and 1,3,5-benzenetribenzoic acid (H_3BTB) under solvothermal conditions resulted, respectively, in NUS-16(Zr) or NUS-16(Hf) with a 3D structure. This 3D framework arises from the interpenetration of 2D porous grids containing BTB^{3-} ions linked by 6-connected $M_6O_4(OH)_4$ clusters (M: Zr or Hf) (**Figure 2**).[82] In comparison, 2D materials named NUS-8(Zr) or NUS-8(Hf) can be obtained by employing modulators in the hydrothermal syntheses. Powder XRD patterns indicate the presence of a 2D planar structure in NUS-8 by inhibition of the interpenetration. FE-SEM images showed the nanosheet morphology for NUS-8 MOFs with a thickness of ≈10–20 nm and a lateral size up to 500–1000 nm, resulting in high aspect ratios of 20–100. Furthermore, AFM measurements confirmed the nanosheet morphology of a thickness of 3 and 4 nm for NUS-8(Zr) and NUS-8(Hf), respectively, implying the stacking of merely two or three layers of atoms. The activity of NUS-8 (2D) and NUS-16 (3D) for the oxidation of thioanisole to the corresponding sulfone by H_2O_2 was compared (**Scheme 5**). The 2D NUS-8 nanosheets exhibited higher activity and higher sulfone selectivity than the 3D NUS-16 counterpart. Specifically, NUS-8(Zr)

exhibited the highest activity affording 100% conversion and 100% sulfone selectivity at ambient temperature. This superior activity was attributed mainly to its strong Lewis acidity as proved by the stronger CO_2 affinity and NH_3 thermoprogrammed desorption (TPD) measurements. Furthermore, NUS-8 exhibited faster kinetics than NUS-16 under identical conditions which was due to the facile diffusion of substrates to the active sites facilitated by the 2D nature of NUS-8 (**Figure 3**). Interestingly, NUS-8(Zr) and NUS-8(Hf) showed the highest stability in boiling in water without undergoing any changes in crystallinity and porosity, while 3D NUS-16 MOFs was unstable under these stability tests as evidenced by powder XRD, thermogravimetric analysis and gas adsorption studies. These results clearly demonstrate the promising applications of 2D MOFs in terms of activity and selectivity. Hot filtration test revealed the heterogeneity of the catalysis (Figure 3). NUS-8(Zr) was recycled three times without any decay in the yield (100%) and selectivity (100%). Similarly, NUS-8(Hf) also retained its activity for three cycles without any loss of its activity. Although the NUS-8 nanosheet samples that was reused three times maintained high crystallinity and similar morphology as evidenced by powder XRD and SEM, respectively, gas adsorption measurements showed some decrease in the surface area that was proposed to be due to the blocking of residual porosity by strong adsorption of reagents or products. If this were the case, one of the effective strategies that have been frequently used to restore the original activity of MOFs is through removal of the adsorbed
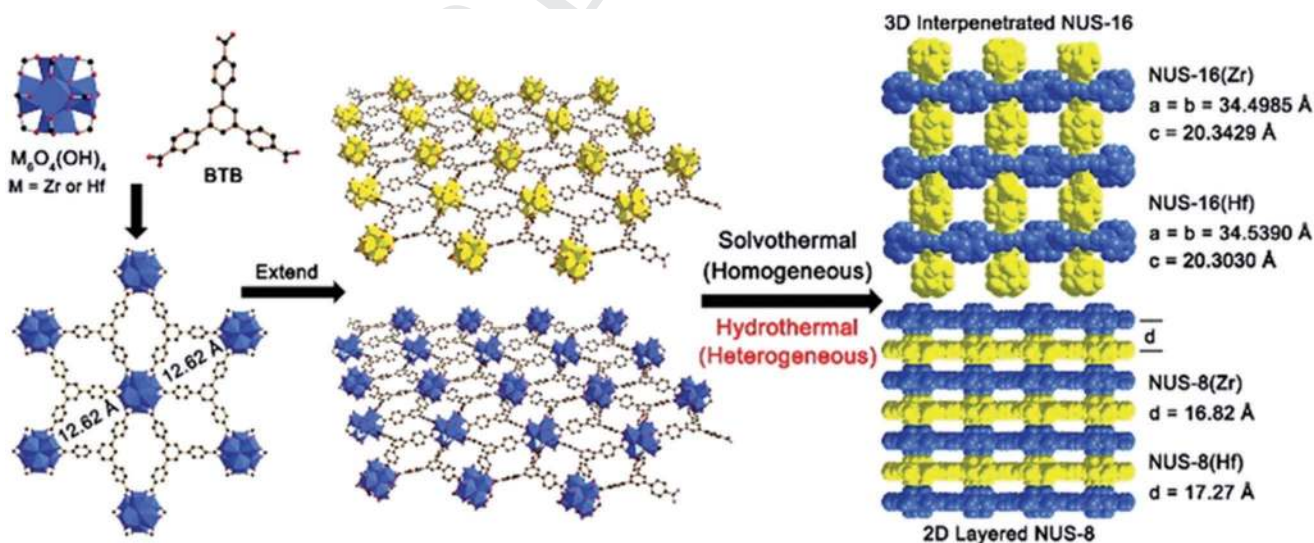
Figure 2. Schematic illustration of the synthesis of 2D MOF nanosheets (NUS-8) and 3D interpenetrated MOFs (NUS-16) (M = Zr or Hf), using hydrothermal and solvothermal methods, respectively. The homogeneous condition of solvothermal synthesis promotes interpenetration of individual 2D nanosheets into a 3D network, while the heterogeneous condition of modulated hydrothermal synthesis disfavors such interpenetration by fast precipitation of intermediate 2D MOF nanosheets.

Figure 3. Kinetic profile for the oxidation of thioanisole by NUS-8 or NUS-16 at room temperature: a) kinetic studies; b) PhSCH₃ conversion and PhSO₂CH₃ selectivity versus time; c) cycle performance. Reproduced with permission.[82] Copyright 2017, Royal Society of Chemistry.
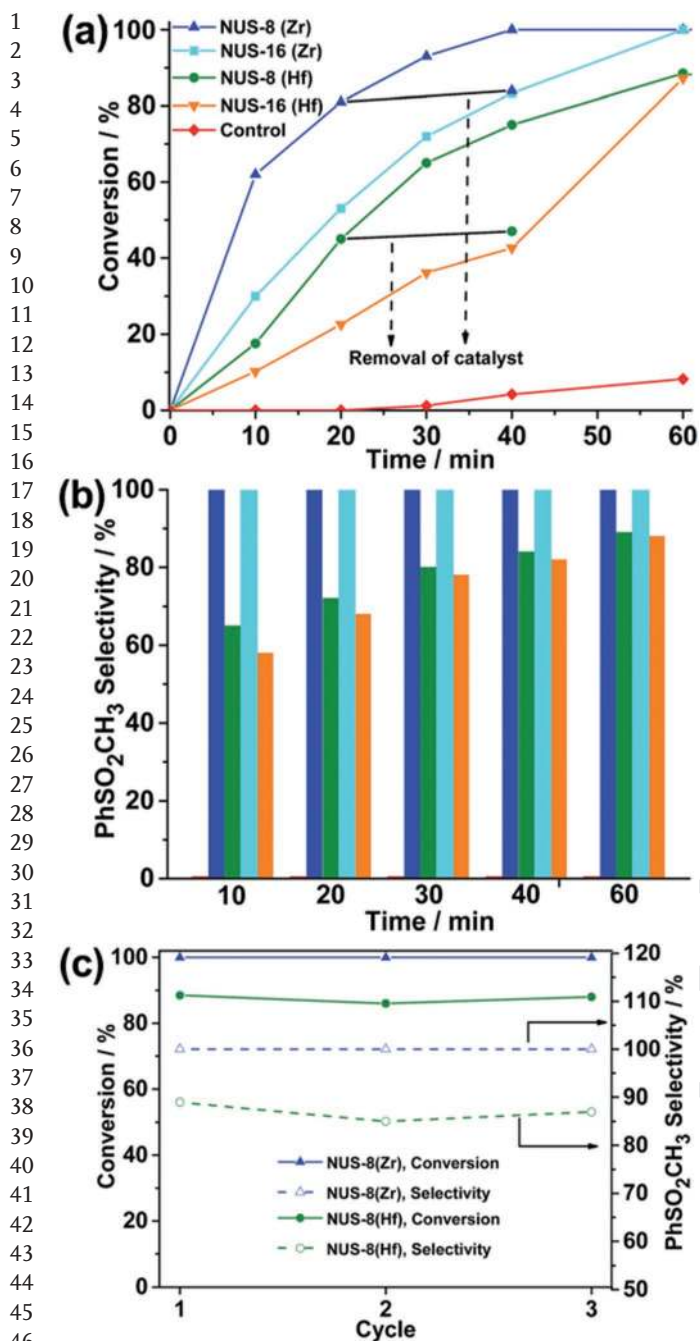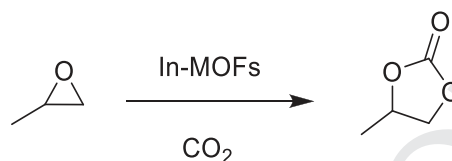

Scheme 6. Cycloaddition of propylene oxide and CO₂ using In-MOFs as solid catalysts.

relationship between dimensionality and catalytic activity, with the most active MOF being 1D, then 2D and finally the 3D sample. These results were rationalized as being derived from the presence of abundant coordinatively unsaturated metal centers in 1D MOFs and show the importance of decreasing solid dimensionality while preserving stability on the catalytic activity. The experimental results presented in Table 3 suggested that the presence of more unsaturated metal centers in the 1D MOF enabled easier interaction with the substrates, while at the same time the 1D MOF has larger site density, affording high yield (entry 7, Table 3). In contrast, a 1D MOF with eight-coordinated In³⁺ centers having less number of unsaturated metal sites (entry 8, Table 3) provided nearly twofold lower activity. Therefore, these data nicely illustrate that the important prerequisites to achieve higher activity is to have high population of unsaturated metal sites with lesser diffusion limitations as in the case of 1D MOFs. Furthermore, the energy barrier of the rate-determining step is reduced to 11.5 kcal mol⁻¹ with In³⁺/Br⁻, thus suggesting the bifunctional role of In(III)/TBAB (TBAB: tetrabutylammonium bromide) as the acid (In³⁺) and basic (Br⁻) catalyst in this reaction. In addition, chemical analysis showed that the concentration of metal leached during the reaction is very low and the In-MOF was stable under the reaction conditions. Hence, they could be recycled many times without any noticeable decay in their activity. These studies have shed light on how the dimensionality of the MOF materials may influence the catalytic activity by increasing the presence of coordinatively unsaturated and accessible active sites in MOFs.

In another precedent, four 2D In MOFs, namely, (Me₂NH₂) [In(SBA)₂], (Me₂NH₂)[In(SBA)(BDC)], (Me₂NH₂)[In(SBA)(BDC-NH₂)], and (NH₄)₃[In₃Cl₂(BPDC)₅] (**Figure 4**) (H₂SBA:4,4′-sulfonyldibenzoic acid; H₂BDC-NH₂: 2-amino-1,4-benzenedicarboxylic acid; H₂BPDC: 4,4′-biphenyldicarboxylic acid), were prepared under solvothermal reaction conditions.[84] The powder XRD patterns of these 2D MOFs showed coincident diffraction patterns with their respective patterns simulated for their ideal structure, thus implying the phase purity of the bulk sample. The catalytic performance of these 2D MOFs was studied in the cycloaddition of CO₂ and propylene oxide with n-Bu₄NBr as the cocatalyst at 80 °C. The order of reaction of these MOFs was (NH₄)₃[In₃Cl₂(BPDC)₅] > (Me₂NH₂) [In(SBA)(BDC-NH₂)] > (Me₂NH₂)[In(SBA)(BDC)] > (Me₂NH₂) [In(SBA)₂] under identical conditions (**Scheme 7**). Among these MOFs, (NH₄)₃[In₃Cl₂(BPDC)₅] exhibited 98% propylene carbonate yield with a TON value of 980. The conversion rate of (Me₂NH₂)[In(SBA)(BDC-NH₂)] was 92%, which is higher than its isostructural (Me₂NH₂)[In(SBA)(BDC)] MOF. The superior performance of (Me₂NH₂)[In(SBA)(BDC-NH₂)] was interpreted

species over MOF catalysts either by washing or by thermal treatment without affecting the structural integrity of MOFs.

Recently, a report studied the influence of MOF dimensionality (1D, 2D, and 3D) on the catalytic activity of a series of In-based MOFs for the CO₂ cycloaddition to epoxides (**Scheme 6**).[83] **Table 3** shows the dimensionality of In-MOFs and the conversion and product selectivity under the optimized reaction conditions. These data clearly indicate a direct

Q5

Table 3. Comparison of the catalytic activity of seven In-containing MOFs for the cycloaddition reaction of propylene oxide and CO_2 (data taken from ref. [83]).

S. No.[a]	Catalyst	In coordination number	Dimensionality	Con. [%][b]	Sel. [%][b]
1	TBAB	–	–	<15	–
2	$In_2(OH)_3(BDC)_{1.5}$	6	3D	50	>99
3	$In(BDC)_{1.5}(bipy)$	8	2D	30	>99
4	$In_2(OH)_2(BDC)_2(phen)_2$	6	2D	80	>99
5	$In(H_2O)(BTC)\cdot(H_2O)(bipy)_{0.25}$	6	2D	75	>99
6	$In(H_2O)(BTC)(phen)$	6	2D	78	>99
7	$[In_2(dpa)_3(1,10\text{-phen})_2]\cdot H_2O$	8, 7	1D	91	>99
8	$[In_2(dpa)(2,2'\text{-bipy})]\cdot 0.5H_2O$	8	1D	48	>99

[a]Reaction conditions: propylene oxide = 42.8 mmol (3 mL), temperature = 50 °C, 1.2 MPa CO_2, 12 h, 600 rpm, catalyst mol% = 0.35, TBAB mol% = 0.35, and semibatch; [b]Determined by GC; phen: phenanthroline; 1,10-phen: 1,10-phenanthroline; 2,2'-bipy: 2,2'-bipyridyl.

considering that NH_2-BDC as an organic linker possesses Lewis basicity complementing In^{3+} Lewis acidity, resulting in a bifunctional catalyst. The higher activity of $(NH_4)_3[In_3Cl_2(BPDC)_5]$ MOF compared to others in the series may be due to its unusual geometrical configuration with octa-coordinate and hepta-coordinate In^{3+} centers. The unsaturated hepta-coordinate In centers in this MOF are proposed to be responsible for activating substrates efficiently and thereby increasing the catalytic activity. However, the structural stability of this 2D MOF should also be investigated by performing repeated cycles, analyzing metal leaching and checking the crystallinity of the spent sample by powder XRD analysis.

A 2D $[Cu(ima)_2]_n$ (ima: imidazole) MOF was synthesized and its activity was examined for the N-arylation of imidazole in methanol at room temperature.[85] Structural analysis of $[Cu(ima)_2]_n$ shows that the coordination around each Cu^{2+} ion is square-planar geometry bound to two monodentate carboxylate groups and two imidazole nitrogen atoms with axial positions left uncoordinated. Also, each ima ligand uses both the carboxylate oxygen and imidazole nitrogen atoms to bridge two Cu^{2+} ions, providing a (4, 4) 2D wavelike rhombic layer (**Figure 5**). N-Arylation of imidazole with phenylboronic acid (**Scheme 8**) was effectively promoted using $[Cu(ima)_2]_n$ MOF catalyst to achieve 86% yield of N-phenylimidazole. In contrast, the use of homogeneous copper salts such as CuI, CuBr, and $Cu(OAc)_2\cdot 2H_2O$ showed 25%, 27%, and 14% yields under identical conditions. Thus, the enhanced activity of $[Cu(ima)_2]_n$ MOF in N-arylation of imidazole was due to the presence of higher density of coordinatively unsaturated Cu^{2+} ions and to their easy accessibility. ICP-AES analysis indicated the occurrence of a minor extent of Cu leaching (0.05 ppm). $Cu(ima)_2$ did not show any decay in its activity until the fourth cycle. Powder XRD of the catalyst used four times showed a pattern that was identical to the pattern of the fresh material, in

Figure 4. a) Coordination environment around In(III) ions in $(NH_4)_3[In_3Cl_2(BPDC)_5]$. b) Planar pentagon connection in $(NH_4)_3[In_3Cl_2(BPDC)_5]$. c) Two interpenetrated pentagon layers viewed from two different perspectives. d) Thickness of the interpenetrated 2D framework structure of $(NH_4)_3[In_3Cl_2(BPDC)_5]$. Reproduced with permission.[84] Copyright 2018, Royal Society of Chemistry.

**ADVANCED
SCIENCE NEWS**

www.advancedsciencenews.com

**ADVANCED
MATERIALS**

www.advmat.de

Scheme 7. Comparison of the activity of $(Me_2NH_2)[In(SBA)_2]$, $(Me_2NH_2)[In(SBA)(BDC)]$, $(Me_2NH_2)[In(SBA)(BDC-NH_2)]$, and $(NH_4)_3[In_3Cl_2(BPDC)_5]$ In MOFs in the cycloaddition of CO_2 to propylene oxide.

agreement with the stability of this catalyst. Regarding the reaction scope, a variety of *N*-arylimidazoles were synthesized using this 2D $Cu(ima)_2$ catalyst under these mild reaction conditions (**Scheme 8**).

A 2D MOF, namely, $[Cd(PBA)(DMF)] \cdot DMF$ (Cd-PBA) (PBA: 5-(4-pyridin-3-ylbenzoylamino)isophthalic acid), with limited porosity in the thin platelets was synthesized by the reaction between PBA as the ligand and Cd^{2+} ions under solvothermal conditions.[86] Structural analysis indicated that the Cd^{2+} ion is six-coordinated, exhibiting an octahedral geometry surrounded by one N atom, four carboxylate oxygen atoms of three different ligands (PBA^{2-}), and one oxygen atom from a coordinated DMF molecule. Furthermore, the neighboring Cd^{2+} ions are coordinated to the carboxylate groups of the ligands to form a 1D infinite chain (**Figure 6**b), and these 1D chains are further linked by PBA^{2-} ligands using the N atoms to give rise to a 2D layer
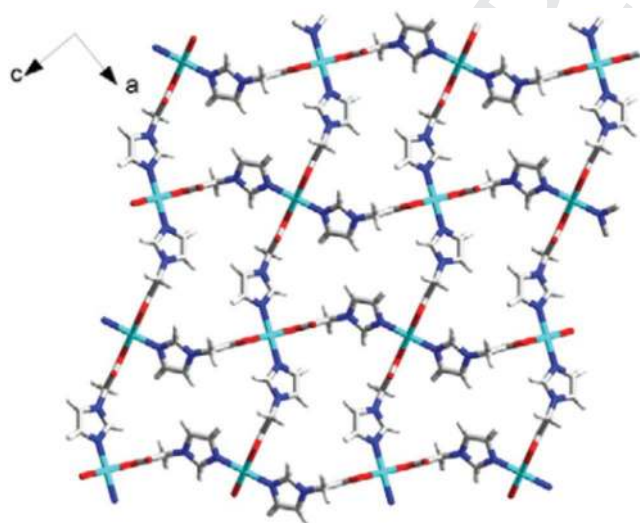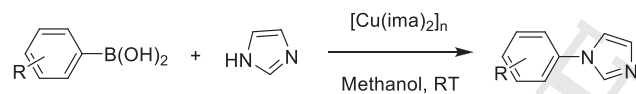
Scheme 8. Reaction of phenylboronic acid with imidazole catalyzed by 2D $[Cu(ima)_2]_n$ MOF and its activity performance with other substrates.

network. Powder XRD of Cd-PBA showed coincident patterns with simulated data, thus implying the formation of 2D MOF as pure phase.

The activity of Cd-PBA was tested in the Knoevenagel condensation between benzaldehyde and malononitrile in ethanol at room temperature, reaching 91% yield (**Scheme 9**). A negligible conversion (3%) was achieved with $Cd(NO_3)_2 \cdot 4H_2O$ as homogeneous catalyst, whereas 39% yield of the condensation product was obtained under identical conditions using PBA as catalyst. In addition, the physical mixture of $Cd(NO_3) \cdot 4H_2O$ and PBA resulted in 31% yield. These control experiments provided direct evidences that the activity is due to the presence of amide functionality in the linker with ready accessibility. Furthermore, the reaction of benzaldehyde with ethyl cyanoacetate with Cd-PBA afforded 37% yield, but the reaction between benzaldehyde and *tert*-butyl cyanoacetate fails under similar conditions. Also, the condensation between 1-naphthaldehyde and malononitrile yields only 42% of the corresponding condensation product. These experiments are compatible with the operation of size selective catalysis under these conditions. Leaching experiments confirmed the heterogeneity of the reaction. Cd-PBA was recycled for four runs without considerable changes in the yield. Furthermore, powder XRD of the Cd-PBA solid reused four times did not show any difference in crystallinity with respect to the fresh sample, thus suggesting the robustness of the material.

Regarding the scope of the catalyst, a series of substituted benzaldehydes with electron donating and withdrawing groups was smoothly reacted with malononitrile leading to the formation of the corresponding condensation product in yields ranging from 61% to 99% under similar conditions. This catalyst was also effective at promoting the cyanosilylation of benzaldehyde with trimethylsilyl cyanide (Scheme 9), affording 99% yield in *n*-hexane at room temperature. A series of control experiments clearly proved that this reaction is promoted by the existence of a high population of coordinatively unsaturated open metal centers.

In another work, a series of Sc-MOFs with 1D, 2D, and 3D structures was prepared under hydrothermal conditions by
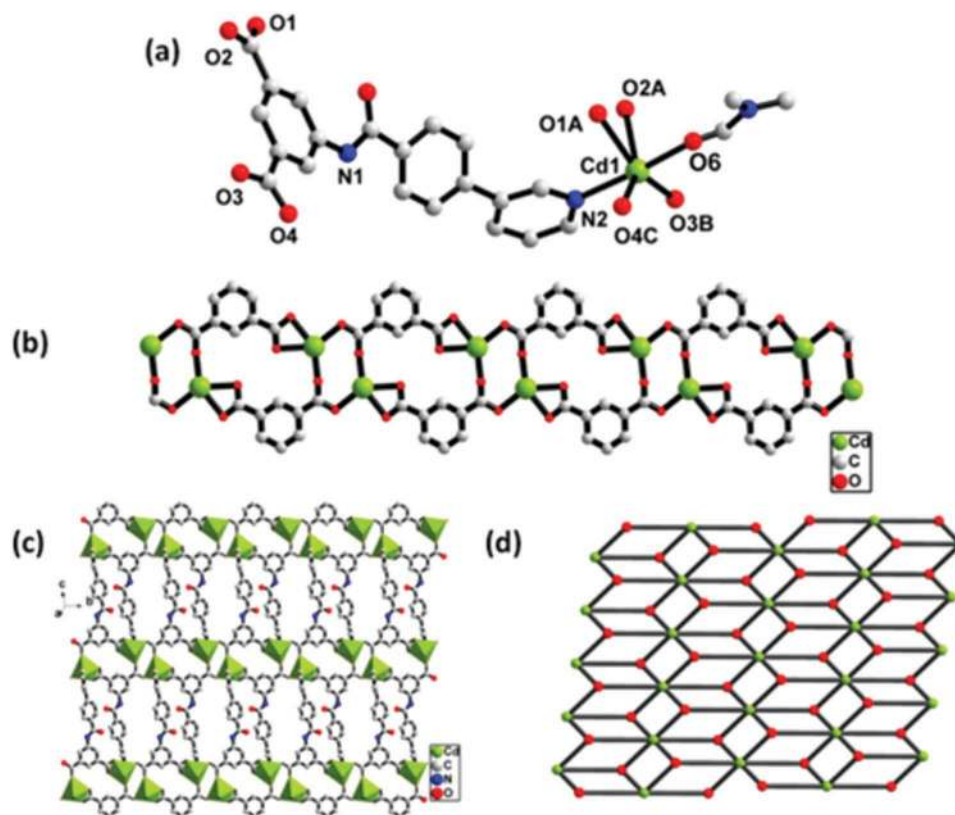

Figure 5. Crystal structure of the 2D $Cu(ima)_2$ MOF exhibiting four-coordinate Cu^{2+} centers. Reproduced with permission.[85] Copyright 2013, Elsevier.

Figure 6. Crystal structure of Cd-PBA showing the a) coordination environment of Cd(II), b) 1D chain connected through the carboxylate groups in Cd-PBA, c) polyhedral view of 2D network, and d) view of the 3,6-connected kgd net topology. Reproduced with permission.[86] Copyright 2018, American Chemical Society.

using identical $Sc_2(pydc)_2$ building units (pydc: 2,3-pyridinedicarboxylic acid) to obtain $[Sc(pydc)(Hpydc)(H_2O)] \cdot H_2O$, $[Sc_2(pydc)_3\text{-}(H_2O)_4] \cdot 5H_2O$ and $[Sc(pydc)(H_2O)(NO_3)]$ MOFs with 1D, 2D, and 3D topologies, respectively.[87] The catalytic performance of these MOFs was examined in the cyanosilylation of 4-nitrobenzaldehyde in acetonitrile. The 2D MOF afforded 99% conversion within 1.5 h, while 1D and 3D MOFs required 8 and 24 h under similar reaction conditions. These results illustrate again that the dimensionality plays a crucial role in determining the activity of the as-synthesized MOFs. Of note is that in this example, the 2D morphology was even more efficient than the 1D. This relationship between dimensionality and catalytic activity arises from the density of coordinatively unsaturated Sc(III) metal ions and easy accessibility of these sites
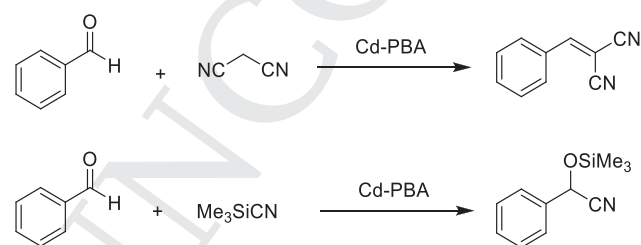
Scheme 9. Cd-PBA catalyzed Knoevenagel condensation and cyanosilylation of benzaldehyde by reacting it with malononitrile and trimethylsilyl cyanide, respectively.

combined with the high thermal and water stability of the 2D MOF. Although 2D MOF retained its activity for three cycles reaching 99% conversion, the conversion decreased to 92% in the fourth cycle. However, a heterogeneity test confirmed the absence of leaching of Sc under these experimental conditions. Therefore, since all the data support catalyst stability, the reasons for the moderate catalyst deactivation remain unclear.

The reaction of 4,4′,4″-s-triazine-1,3,5-triyltri-m-aminobenzoate (H_3TATMA) with Nd(III) resulted in the formation of 2D $[(Nd_2(TATMA)_2 \cdot 4DMF \cdot 4H_2O]_n$ (Nd-TATMA) MOF.[88] Nd-TATMA exhibited a powder XRD pattern identical to the pattern simulated for the theoretical structure, thus confirming the formation of MOF with phase purity. The catalytic performance of Nd-TATMA was examined in the Knoevenagel condensation between benzaldehyde and malononitrile, reaching 95% yield in toluene at 80 °C. The Knoevenagel condensation reaction was promoted by Nd-TATMA through the Lewis basic sites in the linker that can interact with the substrates without spatial restriction. The catalyst retained its activity for four cycles with no drop in its activity. ICP analysis did not show the presence of Nd^{3+} ions in solution, and powder XRD of the reused solid showed that the structural integrity is maintained during multiple reuses. Therefore, all the available data so far indicate the stability of Nd-TATMA under reaction conditions. 4-Fluoro-, 4-nitro-, and 4-methoxybenzaldehydes also condensed with malononitrile efficiently to afford 99%, 99%, and 84% yields, respectively, under identical conditions. Further,
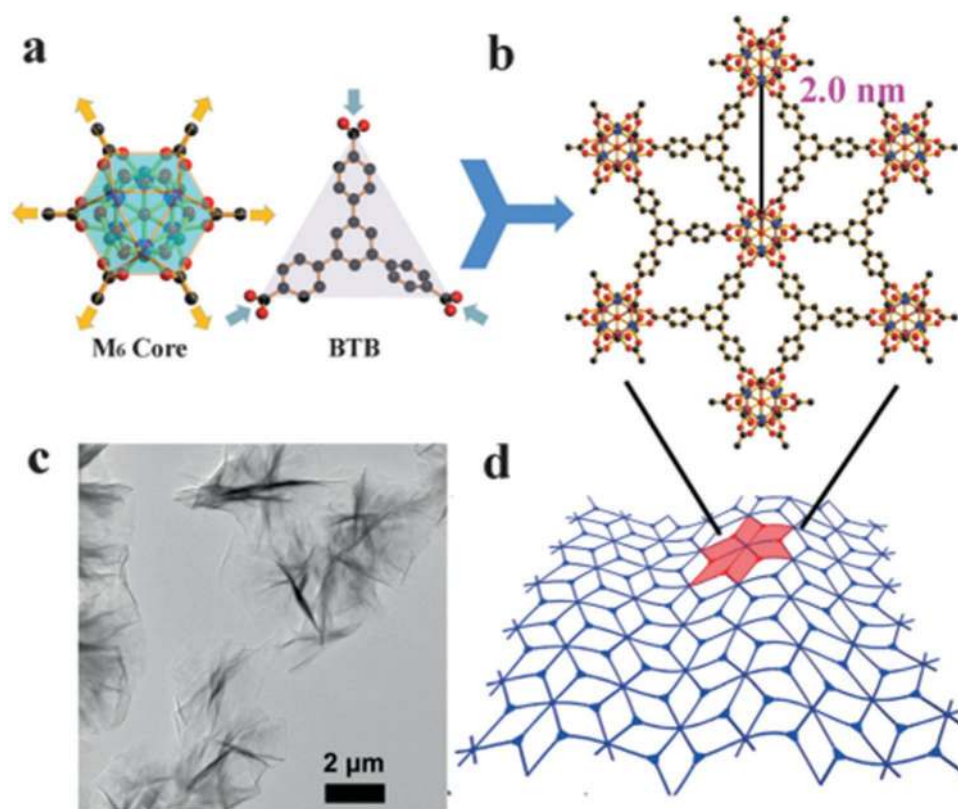
Figure 7. A) Structures of the [Hf$_6$O$_4$(OH)$_4$(HCO$_2$)$_6$(carboxylate)$_6$] SBU and HBTB ligand in MOLs with the connectivity indicated by golden or light blue arrows, respectively. b) Formation of the 2D kgd lattice from 6-connected SBUs and 3-connected BTB ligands. c) TEM image of Hf$_6$O$_4$(OH)$_4$-(HCO$_2$)$_6$(BTB)$_3$ nanosheets. d) Structural representation of the ruffled sheet with kgd topology. Reproduced with permission.[77] Copyright 2016, Wiley-VCH.

3,4-dimethoxybenzaldehyde was also condensed with malononitrile using Nd-TATMA in 76% yield under identical conditions.

In a seminal contribution, Lin and co-workers have reported the synthesis of metal-organic layers (MOLs) comprising secondary building units of [Hf$_6$O$_4$(OH)$_4$(HCO$_2$)$_6$] connected to six BTB ligands forming an infinite 3,6-connected 2D network of Hf$_6$(μ$_3$-O)$_4$(μ$_3$-OH)$_4$(HCO$_2$)$_6$(BTB)$_2$ with kgd topology under solvothermal conditions (**Figure 7**).[77] TEM images revealed the existence of MOLs as wrinkled ultrathin films with an average sheet area of 4 μm × 4 μm (Figure 7). Powder XRD indicated that the pattern for the as-synthesized MOLs is coincident with the pattern of a model having one or two layers of MOLs. Gas adsorption measurements showed a BET surface area of 661.7 m^2 g^{-1} for these MOLs. AFM images showed that the thickness of the MOLs was predominantly 1.2 ± 0.2 nm, although nanosheets with thicknesses of 2.2 ± 0.2 and 3.2 ± 0.2 nm corresponding to two and three layers were also observed.

Hf$_6$(μ$_3$-O)$_4$(μ$_3$-OH)$_4$(HCO$_2$)$_6$(BTB)$_2$ MOL was doped with 4′-(4-benzoate)-(2,2′,2″-terpyridine)-5,5″-dicarboxylate (TPY) as the ligand to obtain TPY-MOL with 30% TPY. This TPY-MOL was further metallated with FeBr$_2$ followed by activation with NaBHEt$_3$, resulting in Fe-TPY-MOL. Although the experimental results indicate that the activation by NaBHEt$_3$ is crucial, the role of this reduction procedure is yet to be disclosed. Powder XRD and TEM studies confirmed that the structure of the MOL was not affected during the doping and metallation steps. Similarly, 3D-interlocked Fe-TPY-MOF1 and 3D-stacked Fe-TPY-MOF2 were also prepared as control catalysts. The activity of Fe-TPY-MOL was investigated in the hydrosilylation of olefins (**Scheme 10**). Fe-TPY-MOL promoted complete hydrosilylation of styrene, affording selectively the anti-Markovnikov product with a TON of >5000. In contrast, no activity was noticed for the interlocked 3D Fe-TPY-MOF1 sample, while the stacked 3D Fe-TPY-MOF2 showed 30% anti-Markovnikov product under
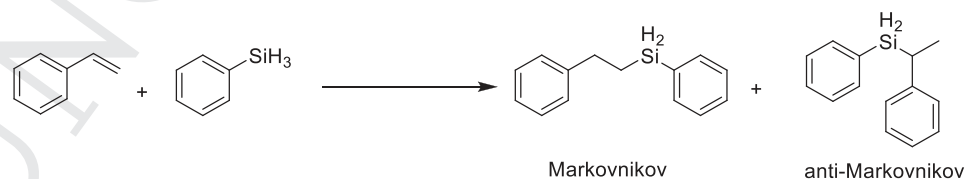
Scheme 10. Hydrosilylation of styrene with phenylsilane.
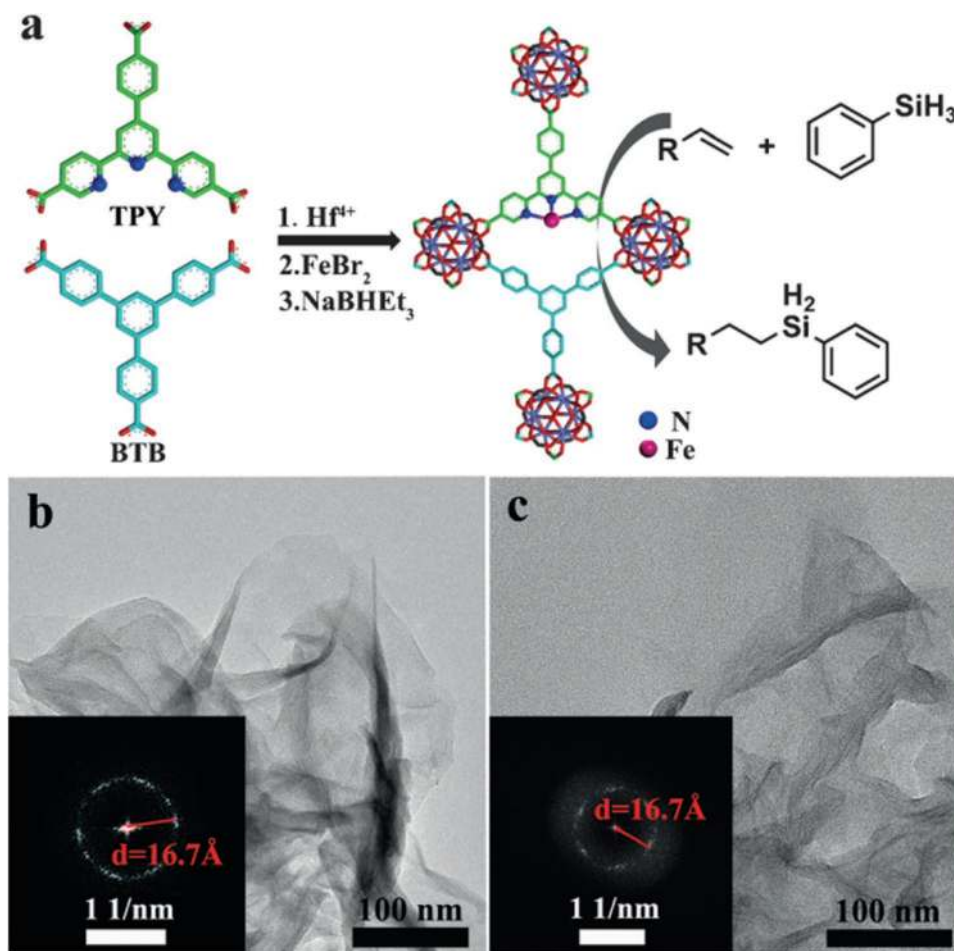
Figure 8. a) Preparation of Fe-TPY-MOL catalyst; HRTEM and FFT images of Fe-TPY-MOL before b) and after catalysis c). Reproduced with permission.[77] Copyright 2016, Wiley-VCH.

identical conditions. The lack of activity or the poor performance of the 3D MOFs was believed to be due to the restricted diffusion of substrates and product within the MOF channels, thus explaining the better performance of the 2D MOF with a larger percentage of exposed active sites without diffusional constraints for reactants and products. Interestingly, the homogeneous Fe-TPY complex showed the formation of the Markovnikov product with approximately ten times lower activity than Fe-TPY-MOL. This lower activity of the homogeneous complex was attributed to the decomposition of the complex, resulting in the formation of metallic iron that is a less efficient hydrosilylation catalyst. The reaction was heterogeneous in nature. The activity of Fe-TPY-MOL was retained for four reuses (**Figure 8**)

without the need for repeated NaBHEt$_3$ activation. However, comparison of the fresh Fe-TPY-MOL with four times reused catalysts by powder XRD, TEM and AFM must have provided sufficient evidence to ascertain its stability during the catalytic reactions. Regarding the scope of Fe-TPY-MOL, a series of olefins was also hydrosilylated in high yields (85–100%) with very high selectivity toward the formation of the anti-Markovnikov product.

In another example, CoCl$_2$·TPY-MOL was analogously prepared and its catalytic activity tested in the benzylic C–H borylation of methylarenes using B$_2$pin$_2$ (**Scheme 11**).[89] CoCl$_2$·TPY-MOL was activated with NaEt$_3$BH, promoting *m*-xylene borylation in 42% yield with a 4.2:1 selectivity toward the benzylic position. In contrast, borylation was unsuccessful
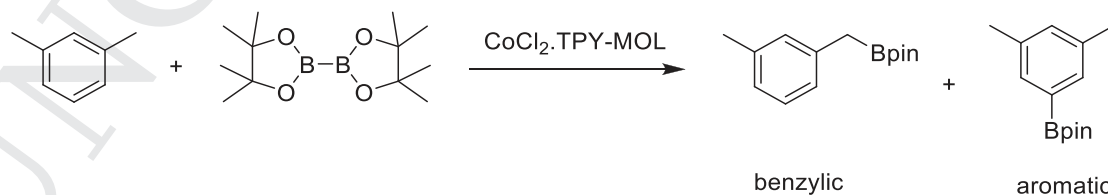
Scheme 11. C–H borylation of *m*-xylene using B$_2$pin$_2$ by the CoCl$_2$·TPY-MOL catalyst.

Table 4. Co·TPY-MOL-catalyzed C–H borylation of arenes ().

Entry[a]	Substrate	Product	Yield (%) (Bn:Ar)
1			95 (4.6:1) (73:14)[c]
2			93 (88)[c]
3[b]			91
4			91 (84)[c]
5[b]			86 (59:6:1)
6			92 (0.91:1.4:1)

[a][Co] = Co(THF)$_2$·TPY-MOL, NMR spectroscopy yield employing CH$_3$NO$_2$ as internal standard; [b]4 mol% [Co]; [c]Isolated yields are shown in parentheses.

in the absence of CoCl$_2$·TPY-MOL activation with NaEt$_3$BH. Furthermore, homogeneous CoCl$_2$·TPY showed only 2% *m*-xylene C–H borylation product under similar conditions. These results indicate that active site isolation in MOLs not submitted to diffusional constraints enhances the TON about 20 times compared to the homogeneous catalyst. Also, spectroscopic studies and DFT calculations have indicated unprecedented formation of MOL-stabilized M^{II}-(TPY$^{••}$)$^{2-}$ species featuring divalent metals and TPY diradical dianions which can be readily accessed by the reactants for the unique and enhanced catalytic activity in C–H borylation. In addition, it also provides unusual borylation selectivity toward the benzylic C—H bond. Using CoCl$_2$·TPY-MOL as the heterogeneous catalyst, a series of methylarenes was converted to their respective borylated products in high yields under the optimized reaction conditions (**Table 4**). Interestingly, the activity of CoCl$_2$·TPY-MOL was retained for at least ten cycles without the need of repeated NaBHEt$_3$ activation and with no drop in its activity in the C–H borylation of *p*-xylene. Powder XRD of the recovered CoCl$_2$·TPY-MOL showed a pattern identical to the pattern of the fresh material. The reaction was heterogeneous, and ICP-MS indicated that Co and Hf leaching in the catalytic process was 0.092% and 0.037%, respectively.

In addition to the intrinsic activity of compositional metal ions in the 2D MOFs, these layered materials can also be used as large area supports to deposit metal NPs as active sites. In one of these examples, Pd@ZIF-L (L: 2-methylimidazole) was synthesized via the assembly method shown in **Figure 9** using Zn^{2+} and 2-methylimidazole, and its activity was tested in the size-selective hydrogenation of alkenes.[90] Powder XRD revealed that the crystalline patterns of Pd@ZIF-L and ZIF-L are identical, thus confirming the formation of ZIF-L around Pd NPs. TEM images indicated that the average particle size of Pd was 3 nm. However, SEM images showed that ZIF-L crystals have a unique crosshair-star shape with a size of ≈20 µm. The morphology of these ZIF-L crystals was, however, highly dependent on the molar ratio between Zn^{2+} and 2-methylimidazole. The loading of Pd in Pd@ZIF-L was determined to be 0.5 wt%. The BET surface area of ZIF-L was 118 m^2 g^{-1}, which is much lower than the BET surface area of ZIF-8 due to the smaller pore size and higher framework density of ZIF-L. Furthermore, the BET surface area of Pd@ZIF-L entrapping Pd NPs was even reduced to 65 m^2 g^{-1}. XPS analysis showed the presence of Pd(0) and Pd(II), which may be due to the incomplete reduction of Pd(II) during the synthesis or may indicate surface oxidation of Pd NPs. Pd@ZIF-L catalyst exhibited
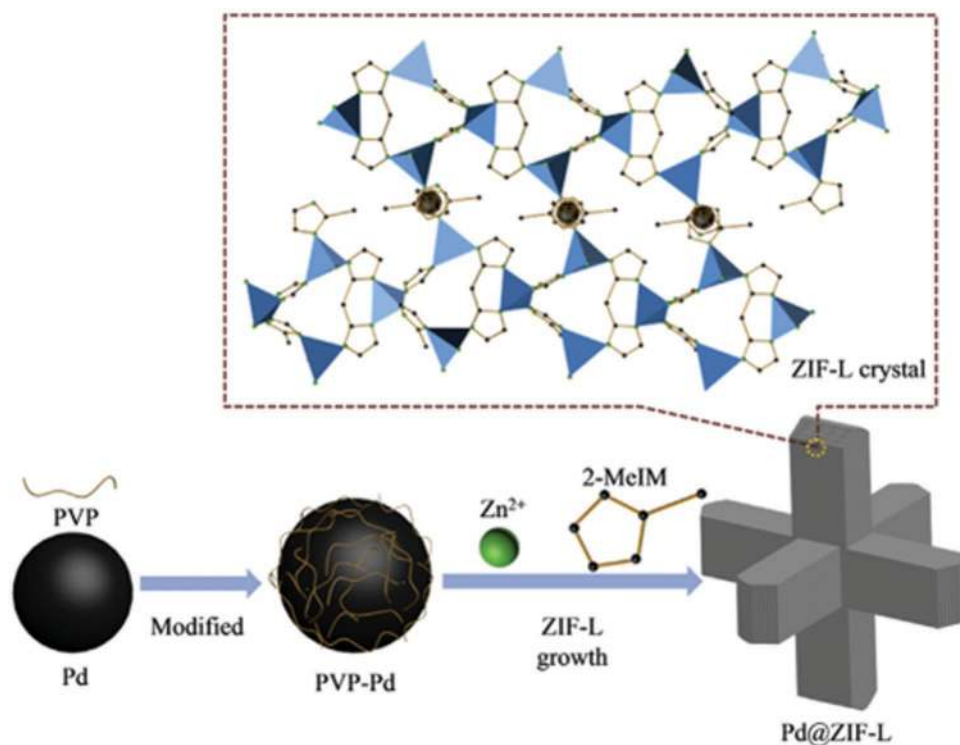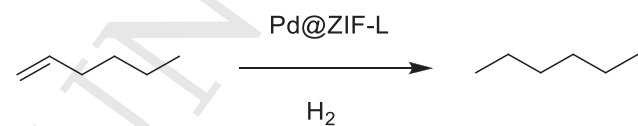
**ADVANCED
SCIENCE NEWS**

www.advancedsciencenews.com

**ADVANCED
MATERIALS**

www.advmat.de

Figure 9. Preparation of Pd@ZIF-L catalyst containing Pd NPs within 2D ZIF-L sheets and forming agglomerates with cross hair star shape. Pd NPs were confined homogeneously within the framework of ZIF-L as evidenced by HRTEM and shown schematically as an inset. Excess PVP was removed before ZIF-L growth. Reproduced with permission.[90] Copyright 2016, Elsevier.

different catalytic activity for alkene hydrogenation (**Scheme 12**) depending on the kinetic dimension of the substrate, following the order of 1-hexene (78%) > cyclohexene (32.6%) > cyclooctene (7.4%) > tetraphenylethylene (0%). As a control, ZIF-L showed no conversion for any of these alkenes under identical conditions (**Figure 10**). The relative reactivity of these alkenes is in accordance with their kinetic diameters that for 1-hexene, cyclohexene and cyclooctene are 1.7, 4.2, and 5.5 Å, respectively. Since ZIF-L has unique cushion-shaped cavities of 6.64 Å size, it is proposed that the diffusion of reagents to the active Pd NPs is the main factor controlling substrate activity.[95] Hence, 1-hexene should exhibit much higher reactivity compared to cyclooctene due to its easier diffusion to reach Pd NPs, while cyclooctene should experience some diffusion limitations. Further, attempts to hydrogenate tetraphenylethylene were unsuccessful since its molecular size of 6.7 Å is larger than the pore size of ZIF-L (6.64 Å). Hence, tetraphenylethylene cannot reach the active Pd sites incorporated in ZIF-L, resulting in no activity. Although Pd@ZIF-L still showed more than 60% conversion in the hydrogenation of 1-hexene after three cycles, structural and

morphological characterization revealed that upon use as a catalyst, ZIF-L transforms into 3D ZIF-8. Nevertheless, chemical analyses showed the absence of Pd leaching during the reaction. These results indicate that the stability of the 2D catalyst is an important issue to be addressed for extended use of ZIF-L in catalysis.

A novel 2D Ni MOF nanosheet was synthesized (**Figure 11**) by employing 5-(4-pyridyl)-methoxyl isophthalic

Scheme 12. Conversion of 1-hexene to hexane using Pd@ZIF-L as the hydrogenation catalyst.
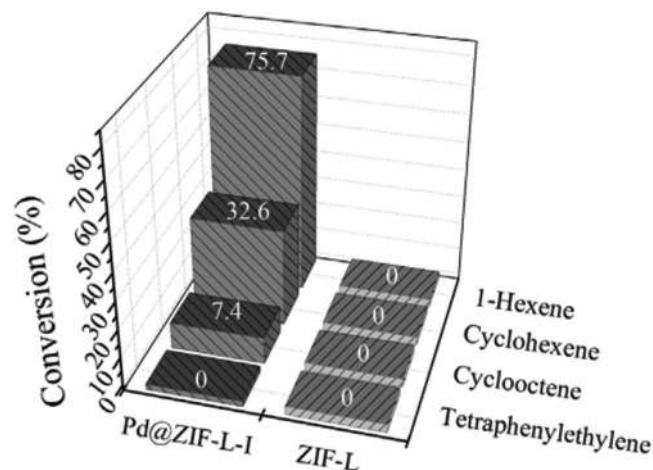

Figure 10. Comparison of the catalytic performance of Pd@ZIF-L and ZIF-L for the liquid-phase hydrogenation of 1-hexene, cyclohexene, cyclooctene, and tetraphenylethylene. Reproduced with permission.[90] Copyright 2016, Elsevier.
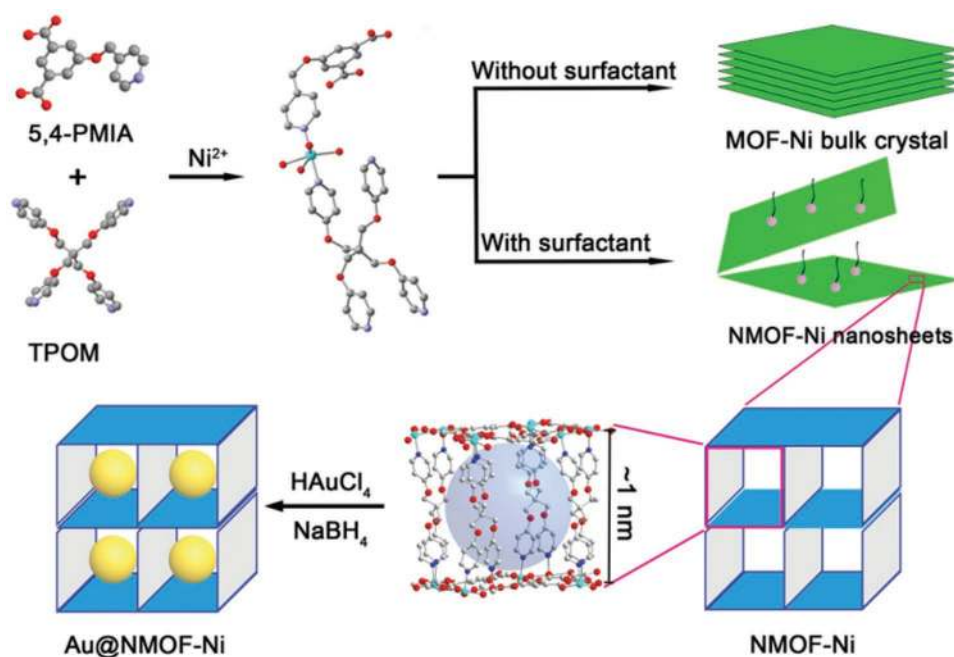
**ADVANCED
SCIENCE NEWS**

www.advancedsciencenews.com

**ADVANCED
MATERIALS**

www.advmat.de

Figure 11. Illustration of the preparation procedure for bulk Ni-MOF crystals, Ni-NMOF nanosheets, and Au@Ni-NMOF (the light blue sphere represents the cavity of MOF, and the yellow spheres are Au NPs). Reproduced with permission.[91] Copyright 2018, Wiley-VCH.

acid (5,4-PMIA) and tetrakis(4-pyridyloxymethylene)methane (TPOM) as organic linkers and Ni(II) as metal nodes in the presence of surfactants resulting in the formation of mixed-ligand MOF (Ni-NMOF).[91] For comparison, bulk $[Ni_2(5,4-PMIA)_2(TPOM)_{0.5}]_n \cdot x$ solvent (Ni-MOF) MOF was also similarly synthesized. The bulk 3D Ni MOF structure consists of a non-interwoven 3D porous network of large quadrilateral 1D channels with dimensions of $\approx 6.0 \times 11.3$ Å^2 running along the b-axis. Subsequently, Au NPs were loaded on Ni-NMOF and Ni-MOF, and the activity of these Au-containing materials was tested in the reduction of 4-nitrophenol using an excess of NaBH$_4$ as the reducing agent. Au was loaded on Ni-NMOF at three different levels to obtain three Au-X@Ni-NMOF nanocomposites (where X is related to the initial amount of HAuCl$_4$). Au loadings determined by ICP analysis were 3.22, 7.27, and 13.23% for Au-1@Ni-NMOF, Au-2@Ni-NMOF, and Au-4@Ni-NMOF nanocomposites, respectively. XPS demonstrated the reduction of Au(III) to Au(0) without affecting the valence state of Ni. TEM images indicated that the mean diameters of Au NPs increase with the Au content in Au-X@Ni-NMOF, estimating sizes of 0.94, 1.15, and 1.58 nm for these three samples. These small NP dimensions are compatible with the entrapment of Au particles within MOF pores. In contrast, the average size of Au NPs in Au@Ni-MOF was 2.37 nm, which is comparatively higher than the average size achieved for the Au-X@Ni-NMOF nanocomposites. Under a specific set of conditions, the reduction of 4-nitrophenol to 4-aminophenol was completed within 6 min using Au-1@Ni-NMOF as the catalyst, while a much longer reaction time was necessary for Au-4@Ni-NMOF (10 min) and pure Au NPs (20 min) (**Figure 12**). Due to the first-order kinetics of the 4-nitrophenol reduction when there is a large excess of NaBH$_4$, the rate constant can be taken as a quantitative value of the relative performance

of the catalyst. The rate constant value for Au-1@Ni-NMOF was 0.404 min^{-1}, which is much superior than those of other Au-based catalysts.[96,97] This enhanced activity of Au-1@Ni-NMOF was attributed to the synergistic effects of the small size of Au NPs (0.94 nm) and the morphological characteristics of 2D Ni-NMOF free from diffusion constraints for accessibility of reagents to the active sites. Interestingly, no significant decay in the activity of Au-1@Ni-NMOF was observed even after ten successive recycles, whereas a notable decrease (<20%) in the activity was observed for pure Au NPs after being subjected to ten cycles (Figure 12). These results clearly indicate that Ni-NMOF enjoys long-term stability without a decrease in its catalytic activity. This catalytic stability should reflect the favorable metal–support interaction for the Au-Ni-NMOF and also effective encapsulation of Au NPs within the cavities, restricting migration and agglomeration of Au NPs. TEM images confirmed that the morphology and average particle size of Au NPs supported on Ni-NMOF remain identical after ten cycles (Figure 12). As indicated above, Au-1@Ni-NMOF required 6 min to reduce 4-nitrophenol (size: 2.4×6.1 Å^2), while the reduction of the nitro group in Mordant Green 17 (MG 17) (7.2×14.0 Å^2) needed more than 60 min (**Figure 13**). This activity difference was considered a consequence of the diffusion limitations through the small pore apertures of Au-1@Ni-NMOF. In contrast, pure Au NPs (20 nm) exhibited no discrimination between the reduction of 4-nitrophenol and MG 17 (Figure 13). These results illustrate the occurrence of size-selective catalysis and support the assumption that the reduction reaction occurs within the pores of few-layered 2D MOFs.

The 2D MOF was synthesized in DMF under hydrothermal conditions by employing Zn^{2+}, 4,5-imidazoledicarboxylic acid (imdc) and bpy to obtain $\{[Zn(Himdc)(bpy)_{0.5}] \cdot DMF\}$. The structure of this MOF showed that hexagonal $\{Zn_6(Himdc)_6\}$
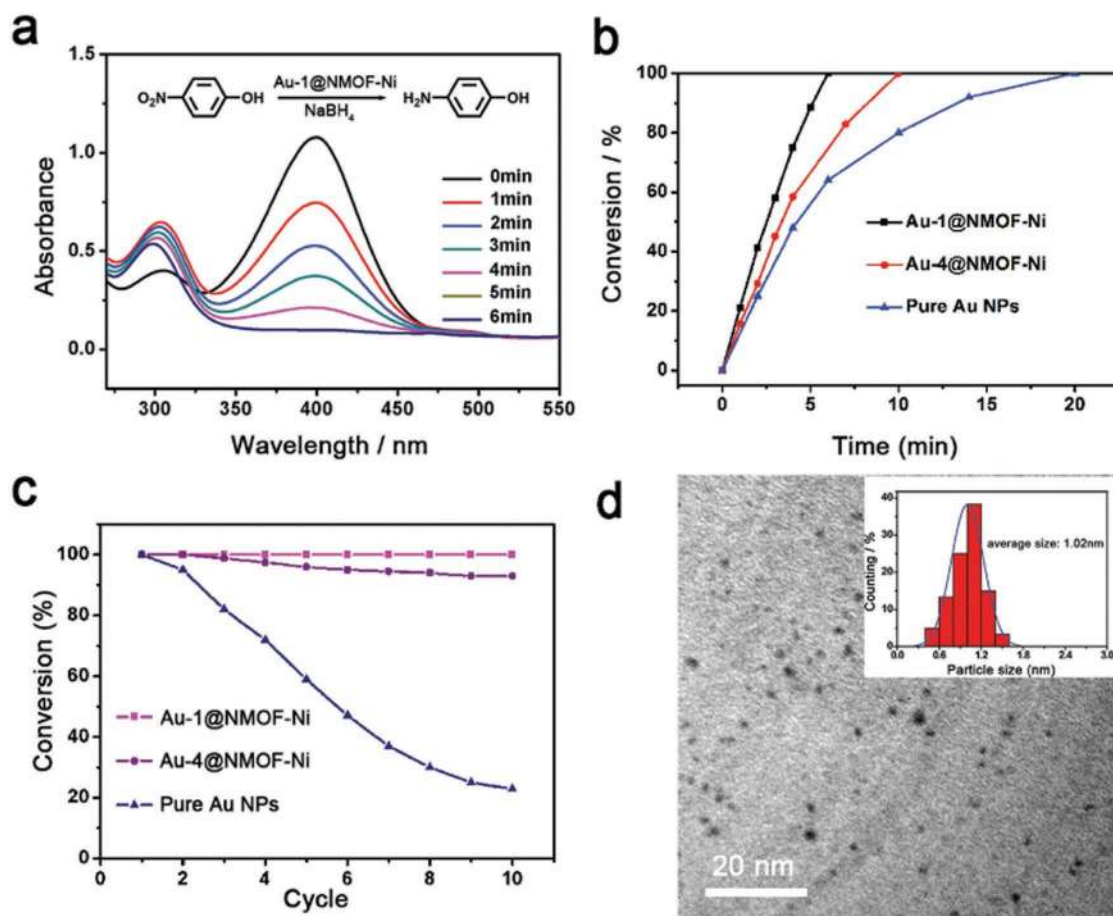
Figure 12. a) UV–vis absorption spectra recorded during the catalytic reduction of 4-nitrophenol over Au-1@Ni-NMOF in aqueous solution at room temperature. b) Comparative time conversion plots and c) catalytic recycles for Au-1@Ni-NMOF, Au-4@Ni-NMOF, and pure Au NPs. d) TEM image and particle size histogram of Au NPs in Au-1@Ni-NMOF after ten cycles. Reproduced with permission.[91] Copyright 2018, Wiley-VCH.

units are coordinated to bpy linkers in the *ab* plane, forming a 2D net. In addition, the free carboxylate oxygen atoms of Himdc ligands provide a highly polar pore surface. The desolvated form of 2D MOF was used as a support to stabilize cuprous oxide (Cu_2O) NPs ($Cu_2O@MOF$) (**Figure 14**).[92] The carboxylate oxygen atoms were proposed to be available on MOF, interacting electrostatically with Cu_2O NPs controlling their size. Powder XRD indicated that the crystalline structure of the 2D Zn MOF is not disturbed during the loading of Cu_2O NPs. XPS analysis revealed that the proportion of the Cu(I) oxidation state on the surface of $Cu_2O@MOF$ is 78%. TEM images showed the presence of spherical Cu_2O NPs with a size ranging between 2 and 4 nm with uniform distribution. ICP-OES analysis indicated that the loading of Cu_2O is 3.46%. The catalytic activity of $Cu_2O@MOF$ was studied in the Huisgen 1,3-dipolar cycloaddition between 1,3,5-methylazidobenzene and phenylacetylene to form the desired cycloaddition product in 98% yield at 50 °C. $Cu_2O@MOF$ retained its activity for three cycles with no decay in its activity. TEM analysis of the reused sample indicated no agglomeration of Cu_2O NPs, showing the stability of this catalyst regarding the size distribution and location of Cu_2O NPs. This was mainly due to the confinement of Cu_2O NPs with the polar pores of the 2D Zn-MOF scaffold. Furthermore, powder

XRD of the fresh and three times used $Cu_2O@MOF$ showed no significant changes in their crystalline pattern. The scope of the cycloaddition was screened by carrying out a series of reactions using different alkyne derivatives as substrates that were coupled with the aromatic tris-azide to form the corresponding adduct in higher than 95% yield under identical conditions.

The reaction between $Cu_2(COO)_4$ paddle-wheel clusters as metal nodes and *meso*-tetra(4-carboxyphenyl)porphyrin [TCPP(M)] (M: Fe, Co) as ligands resulted in the formation of water-stable 2D metalloporphyrinic MOF nanosheets (Cu-TCPP(M)). These hybrid nanosheets were used as templates to grow Au NPs to afford Au/Cu-TCPP(M). The structure of as-prepared 2D heterobimetallic Cu-TCPP(Fe) nanosheet confirmed that the porphyrin metal and paddle-wheel metal are different. The 2D motif of TCPP(Fe) units was coordinated to four $Cu_2(COO)_4$ paddle wheels for each layered sheet, and the layered sheets were stacked in an AB packing pattern. The crystalline nature of 2D Cu-TCPP(Fe) was proved by powder XRD, whereby three diffraction peaks indexed as (110), (001), and (002) were recorded. These peaks correspond to bulk Cu-TCPP(Fe). Furthermore, TEM images indicated that the as-prepared 2D nanosheets range in size between hundreds of nanometers to a few micrometers. AFM images indicate that

ADVANCED
SCIENCE NEWS
www.advancedsciencenews.com

ADVANCED
MATERIALS
www.advmat.de
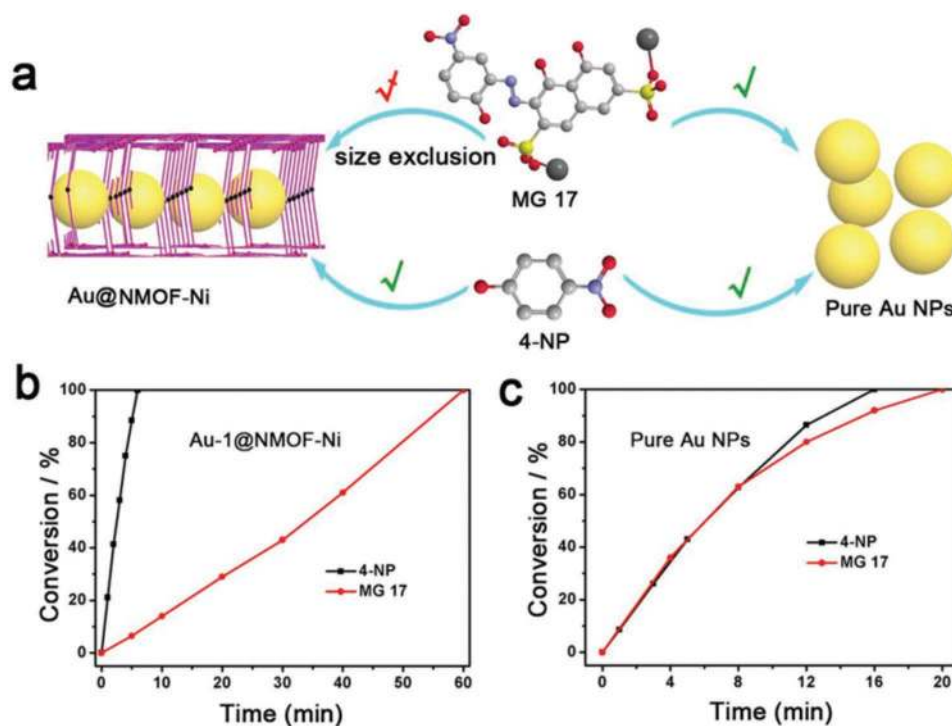
Figure 13. a) Sketch justifying the size selective reduction of 4-nitrophenol and MG 17 for Au-1@NMOF-Ni versus pure Au NPs; b) time-conversion plot for the reduction of MG 17 and 4-nitrophenol over Au-1@NMOF-Ni; c) catalytic conversion of MG 17 and 4-nitrophenol over pure Au NPs. Reproduced with permission.[91] Copyright 2018, Wiley.

the thickness of 2D Cu-TCPP(Fe) nanosheets are 4.1 ± 1.3 nm. TEM images show that the size of Au NPs as 2.1 ± 0.5 nm on Cu-TCPP(Fe) nanosheets. The SAED pattern confirmed that the crystal structure of Cu-TCPP(Fe) nanosheet was not affected during the growth of Au NPs over the nanosheets. XPS analysis indicates the existence of Au in the metallic state in the heterometallic nanosheets. In another analogous sample of Cu-TCPP(Co), the size of the Au NPs was 2.2 ± 0.6 nm as evidenced by TEM images. The catalytic activity of Au/Cu-TCPP(M) heterometallic nanosheets was investigated in enzyme-mimicking cascade reactions, where Au NPs and 2D

Cu-TCPP(M) nanosheets exhibited intrinsic glucose oxidase (GOx) and peroxidase-like activity, respectively.[93] Thus, Au/Cu-TCPP(M) nanosheets were able to catalyze glucose to gluconic acid oxidation by O_2. The process seems to involve the intermediacy of H_2O_2. The in situ generated H_2O_2 can also be used as an oxidant to oxidize 3,3′,5,5′-tetramethylbenzidine (TMB) to oxTMB (**Figure 15**). Ox-TMB exhibits a blue color with the absorption peak maximum at 652 nm, allowing monitoring of the course of the oxidation (Figure 15). In this regard, the activity of Au/Cu-TCPP(M) is analogous to the oxidase–peroxidase-coupled enzyme system, as revealed by the oxidation

Figure 14. Stabilization of Cu_2O NPs in holey 2D layered MOF and the catalytic activity of the resulting material in a triple azide–alkyne cycloaddition reaction. Reproduced with permission.[92] Copyright 2015, Royal Society of Chemistry.

Figure 15. a) Enzyme-mimicking cascade reaction catalyzed by Au/Cu-TCPP(M) hybrid nanosheets (M = Fe, Co). b,c) Time-dependent absorption spectra of the solution obtained after the reaction of TMB in the presence of glucose and Au/Cu-TCPP(M) hybr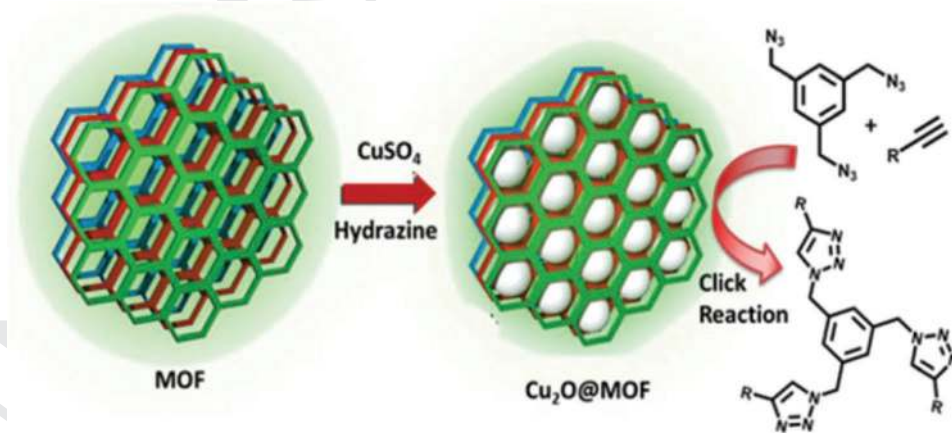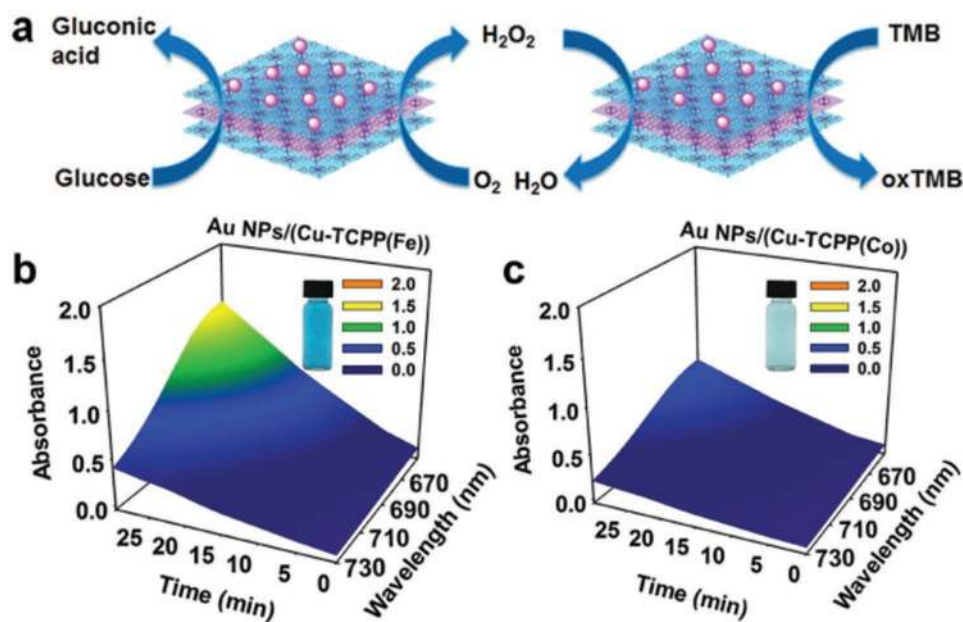id nanosheets incubated for different times. Au/CuTCPP(M) hybrid nanosheets were removed by centrifugation before the spectra were measured. Inset: The photographs correspond to the solutions after 30 min of reaction. Reproduced with permission.[93] Copyright 2017, Wiley-VCH.

of TMB to the corresponding oxTMB. Formation of oxTMB implies the occurrence of a cascade reaction. However, control experiments revealed that neither glucose nor Au/Cu-TCPP(M) heterometallic nanosheets in the presence of TMB could catalyze the cascade reaction. These results clearly indicate that 2D nanosheets can effectively behave advantageously as a support for the stabilization of metal NPs such as Au in this case. The enzyme-mimicking activity is a rare example, and it can trigger the development of other novel "artificial enzymes" for mimicking the catalytic activity of many other complex natural systems. It would have been, however, convenient to characterize the used catalyst to verify its structural integrity as well as the maintenance of the Au particle size.

A strategy shown in **Figure 16** was developed for the synthesis of ultrathin 2D MOF nanosheets through surfactant-mediated synthesis.[94] A bio-based surfactant sorbitol-alkylamine was used for the synthesis of this 2D MOF, which possesses polyhydroxy and amine groups in the head group (SAAS-Cm), acting as competitive coordinating agents to covalently attach to the defective sites of UiO-66 MOF. The synthesis requires a precise control of the surfactant-to-ligand ratio to obtain the intercalated MOFs. The intercalated bulk MOFs assembled with the surfactant due to the interaction of the hydrophobic chains could be exfoliated through a disassembly process, resulting in the formation of ultrathin nanosheets of 3–4 nm. Furthermore, the thickness of the 2D nanosheets was tuned facilely from 3 to 60 nm by varying the alkyl chain length of the surfactants. The use of surfactants with longer alkyl chains (SAAS-C$_{14}$ and SAAS-C$_{16}$) favored the formation of 2D nanosheets with a thickness of 3–4 nm, while surfactants having shorter alkyl chains (SAAS-C$_{10}$ and SAAS-C$_8$) facilitated the growth of the nanosheets in the perpendicular

direction, reaching a thickness of ≈28–60 nm. No nanosheets were formed for those surfactants with an alkyl chain length shorter than C$_8$. Furthermore, 2D layered morphology was confirmed by AFM measurements revealing homogeneous thickness and narrow lateral size distribution, as shown in Figure 16 D and E for one particular case. Ultra-small Ru NPs were supported on 2D MOFs to obtain Ru/UiO-66 nanosheets with Ru particle size of sub-2 nm. The catalytic performance of Ru/UiO-66 nanosheets was examined in the hydrogenation of levulinic acid to γ-valerolactone (GVL) (**Scheme 13**) at 90 °C under 3 MPa of hydrogen. The activity of Ru/UiO-66 nanosheets (349 h^{-1}) was nearly ten times higher than that with Ru NPs loaded on the bulk UiO-66 MOFs (38 h^{-1}). The activity of Ru/UiO-66 nanosheets was also superior to commercial Ru/C (34 h^{-1}) and the reported Ru/ZrO$_2$ (178 h^{-1} at 130 °C) catalysts (**Table 5**). The enhanced activity was attributed to the high density of well dispersed Ru active sites exposed on the 2D structure easily accessible by reactants in such a way that the reaction occurs without geometric constraints. In addition, Ru/UiO-66 nanosheets were reusable for six cycles with no decay in its activity. No significant changes were observed in the structure and morphology after being used six times, thus indicating a high stability under hydrogenation conditions.

3.2. Electrocatalysis

As indicated in the introduction, the more appropriate suitability of 2D MOFs to form thin films, diminishing electrical resistance of the electrode, makes these materials promising in electrocatalysis, an area in which the potential of MOFs is clearly under-exploited. The following section summarizes
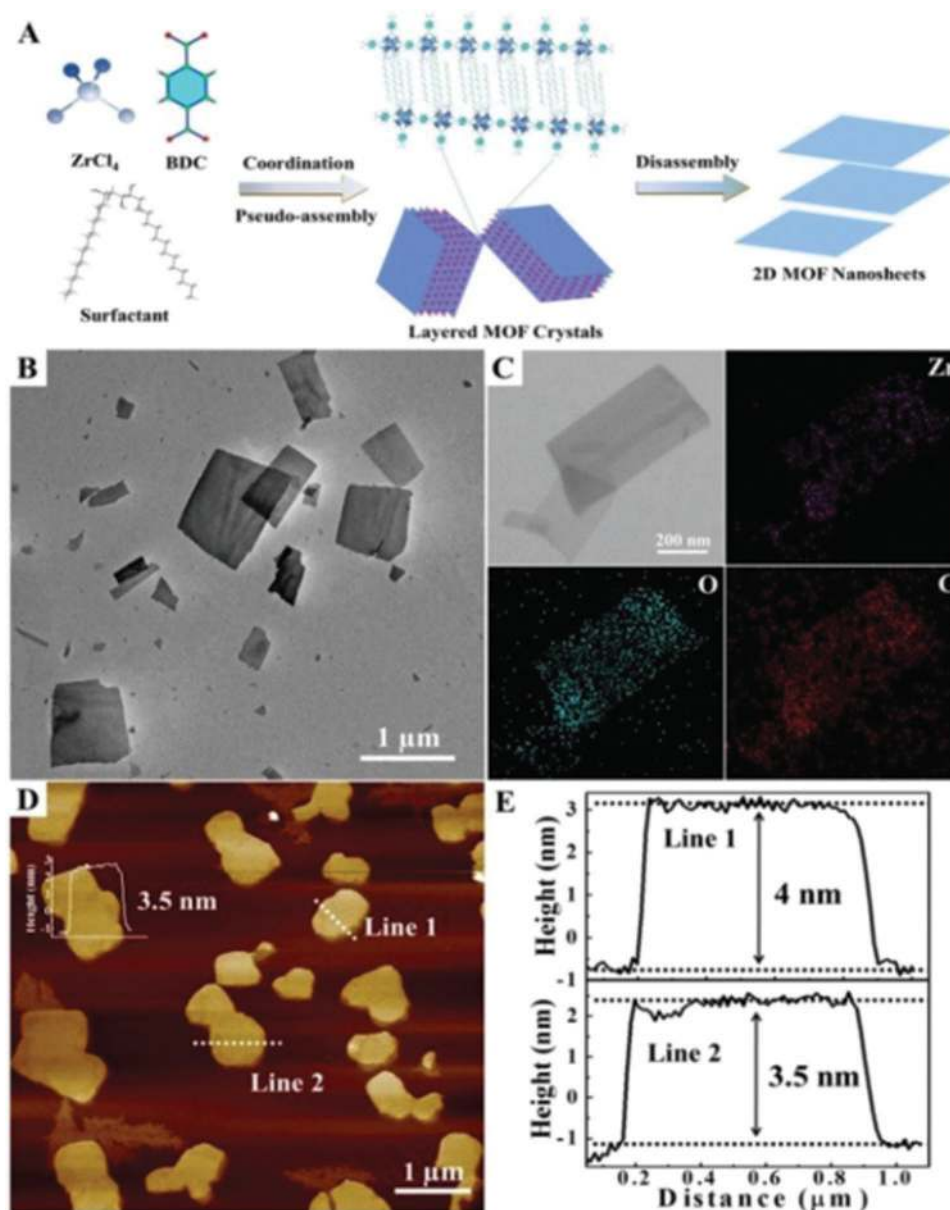
Figure 16. A) Schematic illustration of the process developed to produce 2D UiO-66 nanosheets via a surfactant-mediated method; B) representative TEM image; C) EDX elemental mapping; D) AFM image; and E) the corresponding height profiles of the 2D UiO-66 MOF. Reproduced with permission.[94] Copyright 2018, Royal Society of Chemistry.

recent developments on the use of 2D MOFs as electrocatalysts. **Table 6** provides the summary of the various MOFs that have been reported as electrocatalysts.

Ultrathin 2D MOF nanosheets prepared by joining metal ions with organic ligands exhibit high percentages of coor-
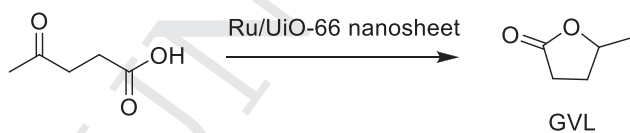
Scheme 13. Conversion of levulinic acid to GVL catalyzed by Ru/UiO-66 nanosheet.

dinatively unsaturated exposed metal atoms over the surface. The presence of these metal sites with exchangeable coordination positions is one of the prerequisites also for exhibiting improved performance in electrocatalysis.[42]

In this context, a recent study has shown the synthesis of 2D MOF comprising nickel ions and BDC as the organic ligand to form ultrathin nickel MOF nanosheets (Ni-MOF) (**Figure 17**).[98] XPS studies revealed the existence of Ni in high oxidation states. Powder XRD of Ni-MOF was consistent with the simulated pattern, presenting a diffraction peak appearing at 8.81° attributable to the 200 plane with the lattice spacing value of 1.05 nm. AFM images (**Figure 18**) confirmed the successful formation of nanosheets by showing heights of ≈4.3–4.4 nm.

Table 5. Levulinic acid hydrogenation to GVL promoted by different catalysts (Reproduced with permission.[94] Copyright 2018, Royal Society of Chemistry).

Catalyst[a]	T [°C]	t [h]	C [%]	Y [%]	TOF [h^{-1}]
Ru/Zr-BDC nanosheets[b]	60	3	>99	>99	116
Ru/Zr-BDC nanosheets[b]	90	1	>99	>99	349
Ru/Zr-BDC bulk[c]	90	3	>99	28.0	38.1
Zr-BDC nanosheets	90	3	<1	<1	–
UiO-66	130	3	28.1	12.2	–
Ru/C[d]	90	3	>99	90.8	34.7
Ru/ZrO$_2$	130	2	99.9	99.9	178

[a]Reaction conditions: 15 mg catalyst, 0.86 mmol levulinic acid, and 3 MPa H$_2$; [b]Ru loading 1.66 wt%; [c]Ru loading 1.72 wt%; [d]Commercial Ru/C catalyst with 5 wt% Ru loading; metal loadings were determined by ICP-AES; the conversion (C) and yield (Y) were determined by gas chromatography.

The electrocatalytic activity of the Ni-MOF nanosheets was examined in the urea oxidation reaction. Ni-MOF was found to require 1.36 V versus the reversible hydrogen electrode (RHE) potential to drive a current density of 10 mA cm^{-2}, which is considerably lower than with Ni(OH)$_2$ (1.46 V) and Pt/C (1.64 V). In addition, Ni-MOF nanosheets exhibited stability for 36 000 s. The superior activity of Ni-MOF in urea oxidation reaction was attributed to be partially due to the high density of active sites over the 2D MOF. The active sites were considered to be nickel species in high oxidation state.

Recently, complexes with CoS$_2$N$_2$ coordination have been obtained in 2D MOFs by coupling two different building units, namely, 2,3,6,7,10,11-triphenylenehexathiol (THT) and 2,3,6,7,10,11-triphenylenehexamine (THA)] with Co^{2+} ions to form THTA-Co (**Figure 19**). As controls, 2D MOFs having exclusively CoS$_4$ or CoN$_4$ were also prepared by using either THT or THA, instead of their mixture. These 2D MOFs exhibit well-defined molecular centers, CoS$_2$N$_2$, CoS$_4$, and CoN$_4$ within the hexagonal sheets of 2D MOFs.[99] A remarkably important fact is that the available data show that these 2D MOFs can be obtained as single sheets. These Co 2D MOFs are expected to provide some advantages in electrocatalysis derived from 1) the precise arrangement of the active sites in the defined networks;

2) exposure of the catalytically active sites on the surface of 2D MOFs; and 3) increased stability by immobilization of the molecular catalytic sites onto solid-state materials. The experimental results revealed that the performance of 2D MOFs in an electrocatalytic HER with different metal complexes (Co and Ni) follows in the order of MS$_2$N$_2$ > MN$_4$ > MS$_4$ and the high activity is proposed to be due to the facile accessibility over the hexagonal networks of 2D MOFs. Furthermore, the experimental and DFT calculation data suggest that the protonation step occurs preferentially at the M@N sites in the MS$_2$N$_2$ complexes on the 2D nanosheets. These results provide a deeper understanding of the electrocatalytic active sites in these types of electrocatalysts based on MN$_x$ and MS$_x$ metal complexes and show the flexibility in the preparation of 2D MOFs with a tunable environment around the metal center.

In addition to mixed ligand MOFs as THTA-Co, 2D MOFs can also be prepared as mixed metals. The 2D bimetallic MOF nanosheets with NiFe and CoFe ultrathin nanosheets (NiFe-UMNs) were fabricated by treating the corresponding metal ions with 1,4-benzenedicarboxylic acid. The structural analysis (**Figure 20**) revealed that both Ni and Fe atoms were octahedrally coordinated by six O atoms in two different ways. In one of the two ways, the metal ions are coordinated with four O atoms from carboxylates of the linker and two O atoms from hydroxyls, while in the second fashion, four O atoms are from hydroxyls and two O atoms from carboxylates. These octahedra connect each other along the 010 direction in the lattice 200 plane but are separated by BDC ligands.

In addition, analogous bulk 3D NiFe-MOFs were synthesized by a hydrothermal method. The powder XRD pattern showed that NiFe-UMNs, CoFe-UMNs, and 3D NiFe-MOFs exhibit analogous crystal structure. Furthermore, AFM images showed that the thickness of both 2D materials, NiFe-UMNs and CoFe-UMNs, is ≈10 nm, implying an average stacking in the ultrathin nanoplatelets of ten layers approximately. The electrocatalytic activity of these catalysts was studied in the oxygen evolution reaction (OER). The Tafel slope of NiFe-UMNs was 30 mV decade^{-1}, which is comparatively lower than the slope for other materials (31 mV decade^{-1} for CoFe-UMNs, 61 mV decade^{-1} for 3D NiFe-MOFs, 70 mV decade^{-1} for commercial IrO$_2$ and 42 mV decade^{-1} for commercial RuO$_2$) (**Figure 21**).

Table 6. List of 2D MOFs reported as electrocatalysts.

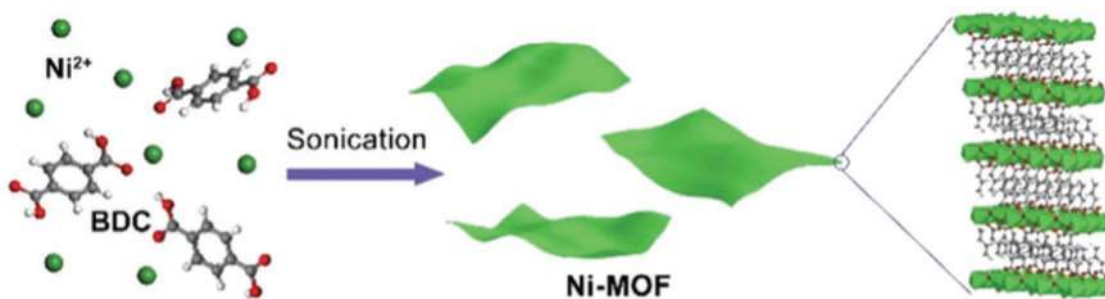| 2D MOFs	Preparation method	Reaction	Activity	Stability evidence	Ref.
Ni-MOF	Sonication-assisted	Urea oxidation	Required 1.36 V	Galvanostatic experiment up to 36 000 s	[98]
CoS$_2$N$_2$-2D MOFs	Interfacial synthesis	Hydrogen evolution reaction (HER)	2D MOFs with CoS$_2$N$_2$ linkage exhibited higher activity	Cyclic voltammetry	[99]
NiFe-UMNs	Ultrasonic oscillation method	Oxygen evolution reaction (OER)	Tafel slope was 30 mV decade^{-1}	Current density almost unchanged at 0.28 V overpotential for 10 000 s, XRD, TEM	[100]
Ni-MOF@Fe-MOF	Stepwise synthesis	OER	265 mV overpotential at 10 mA cm^{-2} current density	TEM	[101]
NiPc-MOF	Bottom-up strategy	Water oxidation reaction	onset current at 1.48 V	Chronopotentiometry measurements, SEM, and Raman spectroscopy	[102]
Zn-TCPP(BP)	Coordination chelation	Electrochemical sensing of nitrite	Detection limit of 0.26×10^{-6} M	Reuse	[103]
CuCo-UMOFNs	Ultrasonication	Hydrogen production from methanol	Lowered anodic potential of 1.365 V	Cyclic voltammetry, chronoamperometry	[104]

Figure 17. Schematic illustration of the synthesis process for Ni-MOF nanosheets. Reproduced with permission.[98] Copyright 2017, Royal Society of Chemistry.

It was claimed that this is the lowest Tafel slope achieved for OER, thus implying the superior activity of 2D MOFs as electrocatalysts.[105]

Interestingly, the much higher activity of NiFe-UMNs can be attributed to the intrinsic higher performance of Ni (compared with CoFe-UMNs), the synergistic effect between Ni and Fe active centers and the exposure of the coordinatively unsaturated active metal sites in 2D NiFe-UMNs structure (compared to bulk NiFe-MOFs).[106] Taking NiFe-UMNs as 100% relative TOF value, other materials exhibit much lower TOFs such as CoFe-UMNs (7.1%), bulk NiFe-MOFs (1.4%) and commercial RuO_2 (60.4%) (Figure 21). The current density almost remains unchanged for NiFe-UMNs (only 4.8% current loss) at an overpotential of 0.28 V for 10 000 s, which indicates a stability significantly superior to commercial RuO_2 ($\approx$19% current loss). These data clearly show the durability and stability of 2D NiFe-UMNs. Furthermore, the XRD pattern and TEM image after the use of NiFe-UMN in OER do not show noticeable changes with respect to data from the fresh material, thus demonstrating the stability of NiFe-UMNs under these experimental conditions of the OER. Overall, the excellent performance of NiFe-UMNs nicely illustrates the potential that 2D MOFs possess in electrocatalysis to overcome the activity of noble and precious metals for electrochemical reactions that may have considerable importance in the context of the ongoing change from fossil fuels to renewable electricity.

In a recent study, 2D MOF nanosheet hybrid materials were fabricated by stepwise synthesis (**Figure 22**) at room temperature and their electrocatalytic activity was tested for a water oxidation reaction.[101] The as-prepared Ni-MOF nanosheets were found by TEM to exhibit flexible ultrathin layered morphology, possessing lateral size on the micrometric scale. AFM measurements of the thickness of the Ni-MOF nanosheet give values of $\approx$5 or 6 nm, corresponding to $\approx$5–6 structural layers. Later, 2D Ni-MOF nanosheets were decorated with Fe-MOF NPs through the in situ coordination of surface-anchored Fe(III) and BDC ligands to provide Ni-MOF@Fe-MOF (Figure 22). In contrast to the results shown in Figure 22c, Fe-MOF NPs undergo extensive agglomeration in the absence of Ni-MOF nanosheet. Powder XRD revealed that Ni-MOF@Fe-MOF and pristine Ni-MOF exhibit identical crystal phases, confirming that anchoring of Fe-MOF NPs does not affect the crystallinity of the Ni-MOF support. High-angle annular dark field scanning TEM (HAADF-STEM) coupled with energy dispersive spectroscopy (EDS) elemental mapping indicated a uniform distribution of Ni, O, and C throughout the nanosheets (Figure 22e). In addition, the uniform distribution of Fe species over the Ni-MOF nanosheet confirmed the adequate dispersion of Fe-MOF on the Ni-MOF nanosheets. The Ni/Fe atomic ratio measured by ICP-OES analysis was 3.5/1. XPS revealed the existence of Ni^{2+} in the Ni-MOF@Fe-MOF hybrid catalyst. The electrocatalytic activity of Ni-MOF@Fe-MOF hybrid for OER was studied in 1 M KOH solution, and its performance was compared with the performance of bare Ni-MOF, Fe-MOF, and IrO_2 under identical experimental conditions. IrO_2 is currently considered the benchmark OER catalyst. The optimal catalytic performance of Ni-MOF@Fe-MOF hybrid was assessed by measuring 265 mV overpotential at a current density of 10 mA cm^{-2} that is lower than the state-of-the-art catalyst, IrO_2 (365 mV). Interestingly, the bare aggregated Fe-MOF NPs were inactive for the water oxidation reaction, although hybridization of Fe-MOF significantly decreased the overpotential of Ni-MOF (370 mV) by $\approx$100 mV. Furthermore, the Ni-MOF@Fe-MOF hybrid delivered a high current density of 12.8 mA cm^{-2} at a potential of 1.50 V versus RHE, which is ten times higher than that of bare Ni-MOF (1 mA cm^{-2}). In addition, the Tafel slope for OER with Ni-MOF@Fe-MOF hybrid (82 mV decade^{-1}) was also lower compared to Ni-MOF (139 mV decade^{-1}) and IrO_2 (158 mV decade^{-1}). These electrocatalytic data clearly establish a substantial enhancement of the OER performance for 2D Ni MOFs through hybridization of Fe-MOF on the Ni-MOFs nanosheets and illustrate again the potential that the 2D morphology offers in electrocatalysis to develop highly efficient electrodes, including the development of hybrid materials. TEM and HRTEM images for the Ni-MOF@Fe-MOF hybrid after 50 cycles showed the generation of well-defined mesopores ranging between 5 and 10 nm. These mesopores are proposed to originate from the structural shrinkage of the MOFs caused by the decomposition of organic ligands during water oxidation. The enhanced activity of the 2D MOF-NP hybrid was attributed to the in situ formation of abundant interconnected active NiO species, homogeneous distribution of mesopores and the lack of mass diffusion limitations.

The synthesis of a novel noble-metal-free nickel phthalocyanine-based 2D MOF (NiPc-MOF) was accomplished following a bottom-up strategy as shown in **Figure 23**.[102] The building block to construct NiPc-MOF, namely, metal-free 2,3,9,10,16,17,23,24-octaaminophthalocyanine, was prepared and treated with $NiCl_2$ to form NiPc-NH$_2$. Subsequently, the NiPc-NH$_2$ monomers were connected to each other by reacting

**ADVANCED
SCIENCE NEWS**
www.advancedsciencenews.com

**ADVANCED
MATERIALS**
www.advmat.de
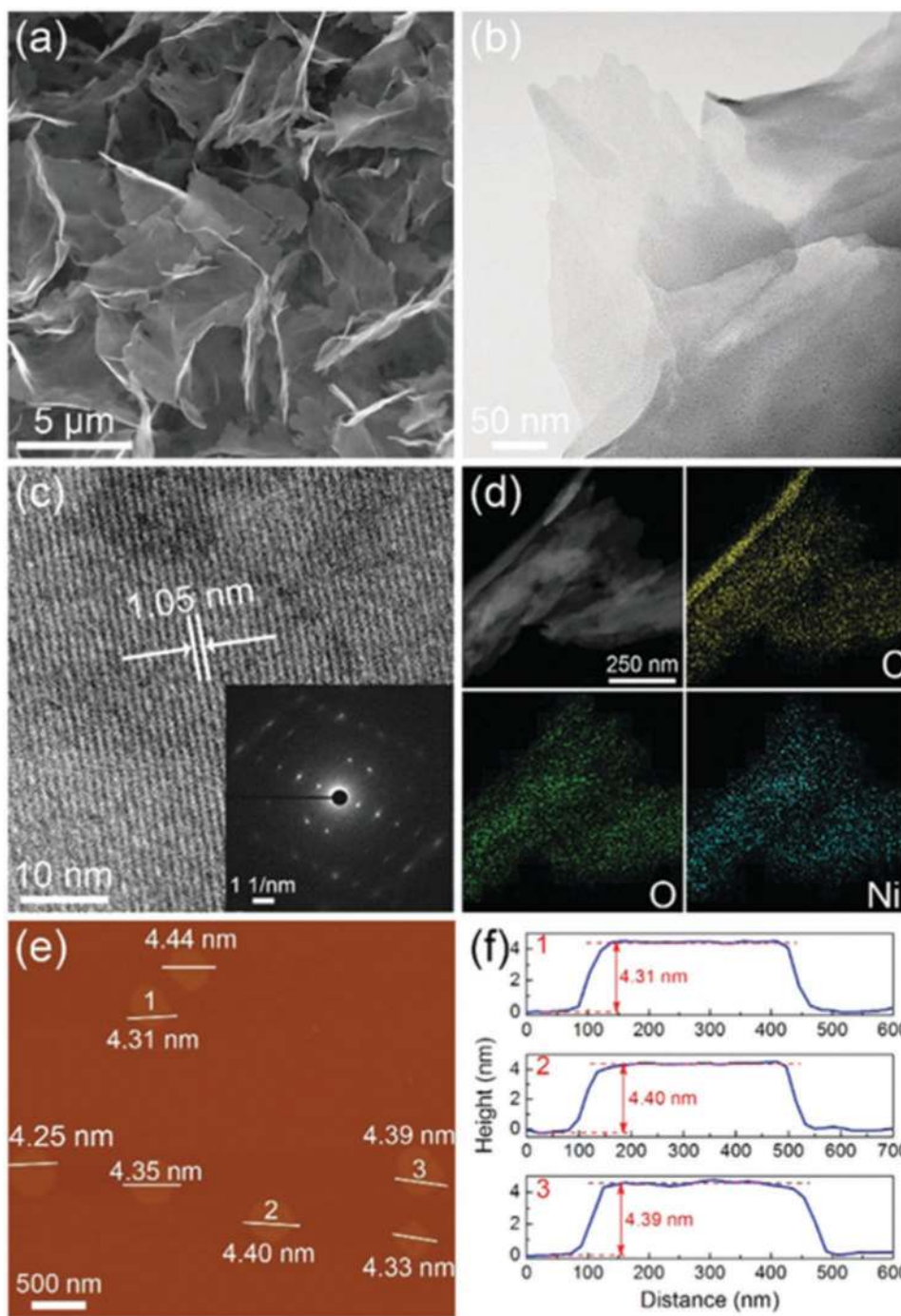
Figure 18. a,b) SEM and TEM images of Ni-MOF. c) HRTEM image and SAED pattern (inset) of Ni-MOF. d) Elemental mapping of Ni-MOF. e,f) AFM image of Ni-MOF and the corresponding height profiles along the marked white lines. Reproduced with permission.[98] Copyright 2017, Royal Society of Chemistry.

them with Ni(isq)$_2$ linkers (isq: bis(o-diiminobenzosemiqui-nonate)) to achieve NiPc-MOF as a huge π-conjugated 2D MOF with fourfold symmetry. Later, films of NiPc-MOF were grown on various supports such as fluorine-doped tin oxide (FTO), indium tin oxide (ITO), quartz glass, and silicon wafer. The thickness of the NiPc-MOF film on FTO was ≈300 nm as shown by SEM images. The catalyst loading on FTO determined by

ICP-AES analysis was found to be 7.6 μg cm^{-2}. The activity of these films was studied for the water oxidation reaction. The NiPc–MOF afforded excellent performance by showing a sharp onset current at 1.48 V that corresponds to an overpotential for OER as low as only 0.25 V. This onset potential measured for NiPc-MOF is much lower than the onset potentials reported for related molecular OER complexes as noble-metal-free

ADVANCED
SCIENCE NEWS
www.advancedsciencenews.com

ADVANCED
MATERIALS
www.advmat.de
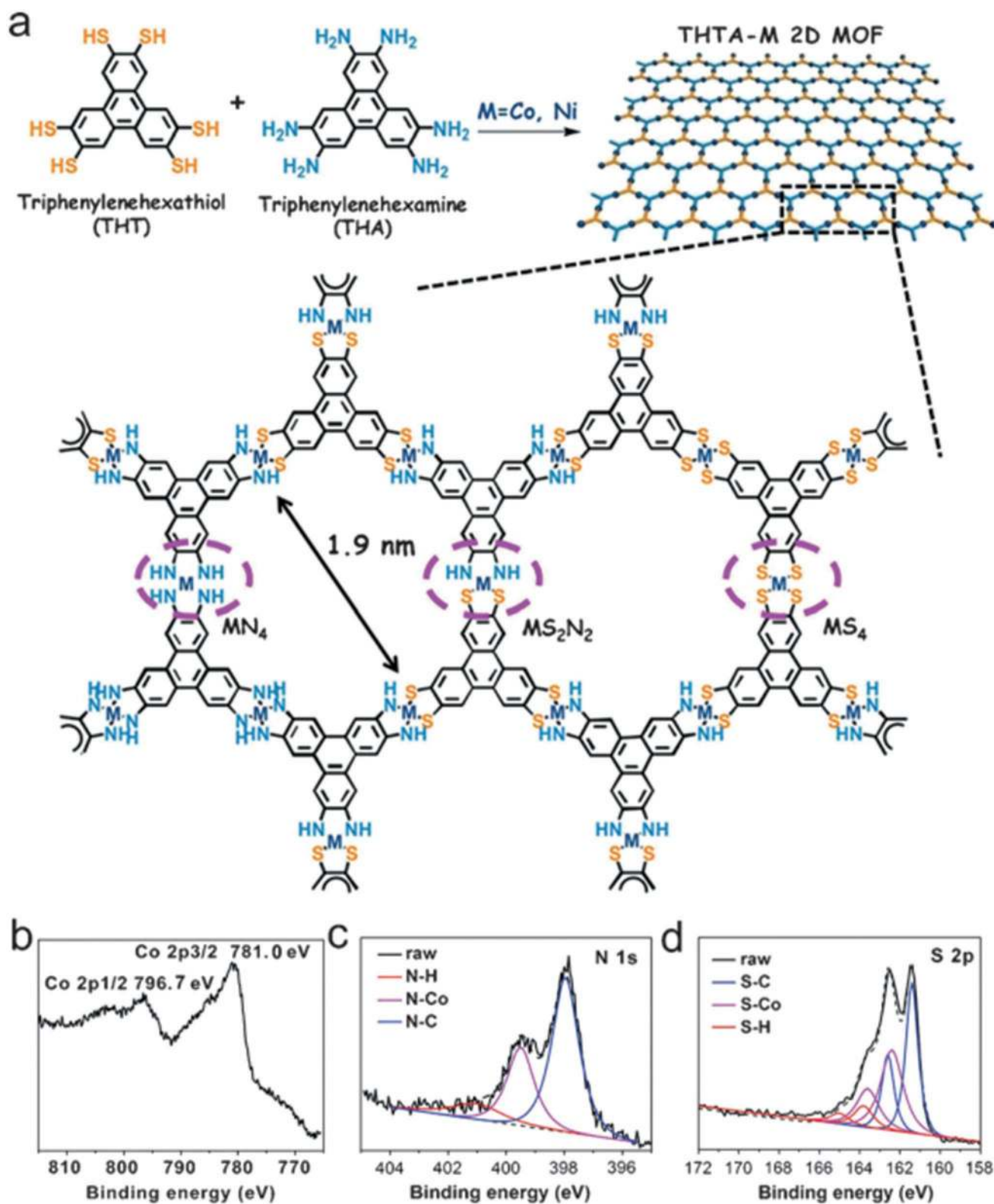
Figure 19. a) Schematic synthesis of single-layer 2D MOFs in which the MS_2N_2 complexes along with the MN_4 and MS_4 moieties were incorporated into the hexagonal networks through metal dithiolene–diamine coordination (THTAM) (M = Co and Ni); b–d) high-resolution Co 2p XPS spectra, N 1s spectra, and S 2p spectra of single-layer THTA-Co 2D MOF sheets, respectively. Reproduced with permission.[99] Copyright 2017, Wiley-VCH.

ADVANCED
SCIENCE NEWS

www.advancedsciencenews.com

ADVANCED
MATERIALS

www.advmat.de
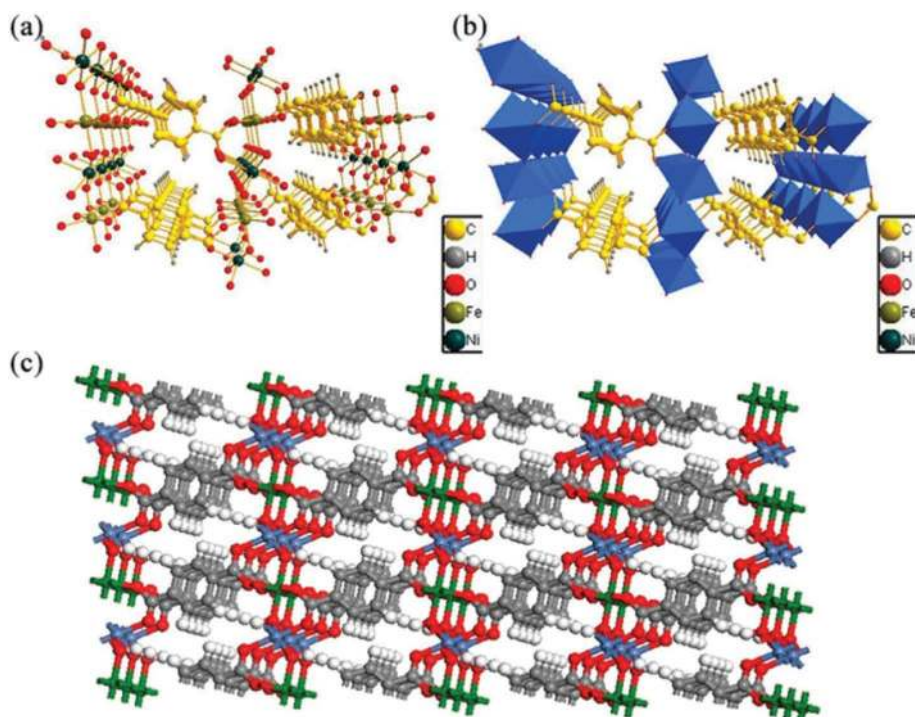
Figure 20. a) Crystal structure of NiFe-UMNs. b) Octahedral coordination mode of metal atoms exhibiting two types of octahedra. c) Atomic arrangements of NiFe-UMNs. Reproduced with permission.[100] Copyright 2018, Elsevier.
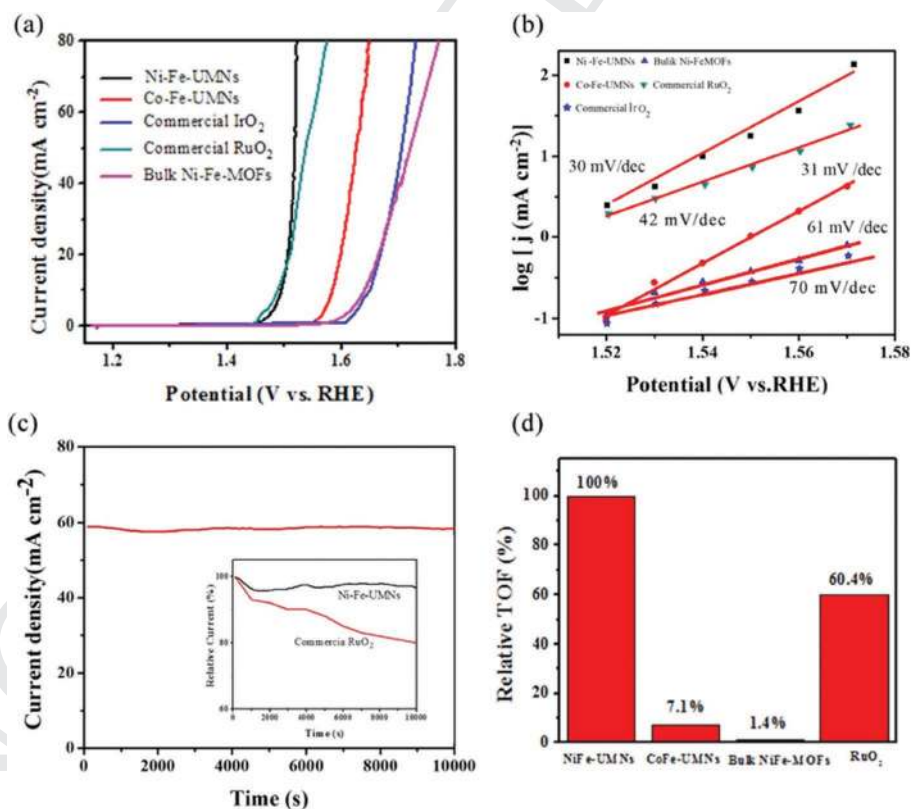
Figure 21. Comparative OER activity of NiFe-UMNs. a) LSV curves of NiFe-UMNs, CoFeUMNs, bulk NiFe-MOFs, commercial RuO_2 and commercial IrO_2 in O_2-saturated 1 M KOH solution; b) Tafel plots of NiFe-UMNs, CoFe-UMNs, bulk NiFe-MOFs, and commercial RuO_2; c) chronoamperometric curves for long-term stability tests of NiFe-UMNs at the constant overpotential of 0.28 V. The inset shows a comparison with commercial RuO_2 (red curve). d) Comparison of TOF values for NiFe-UMNs, CoFe-UMNs, bulk NiFe-MOFs, and commercial RuO_2 at the overpotential of 0.28 V. Reproduced with permission.[100] Copyright 2018, Elsevier.

ADVANCED
SCIENCE NEWS

www.advancedsciencenews.com

ADVANCED
MATERIALS

www.advmat.de
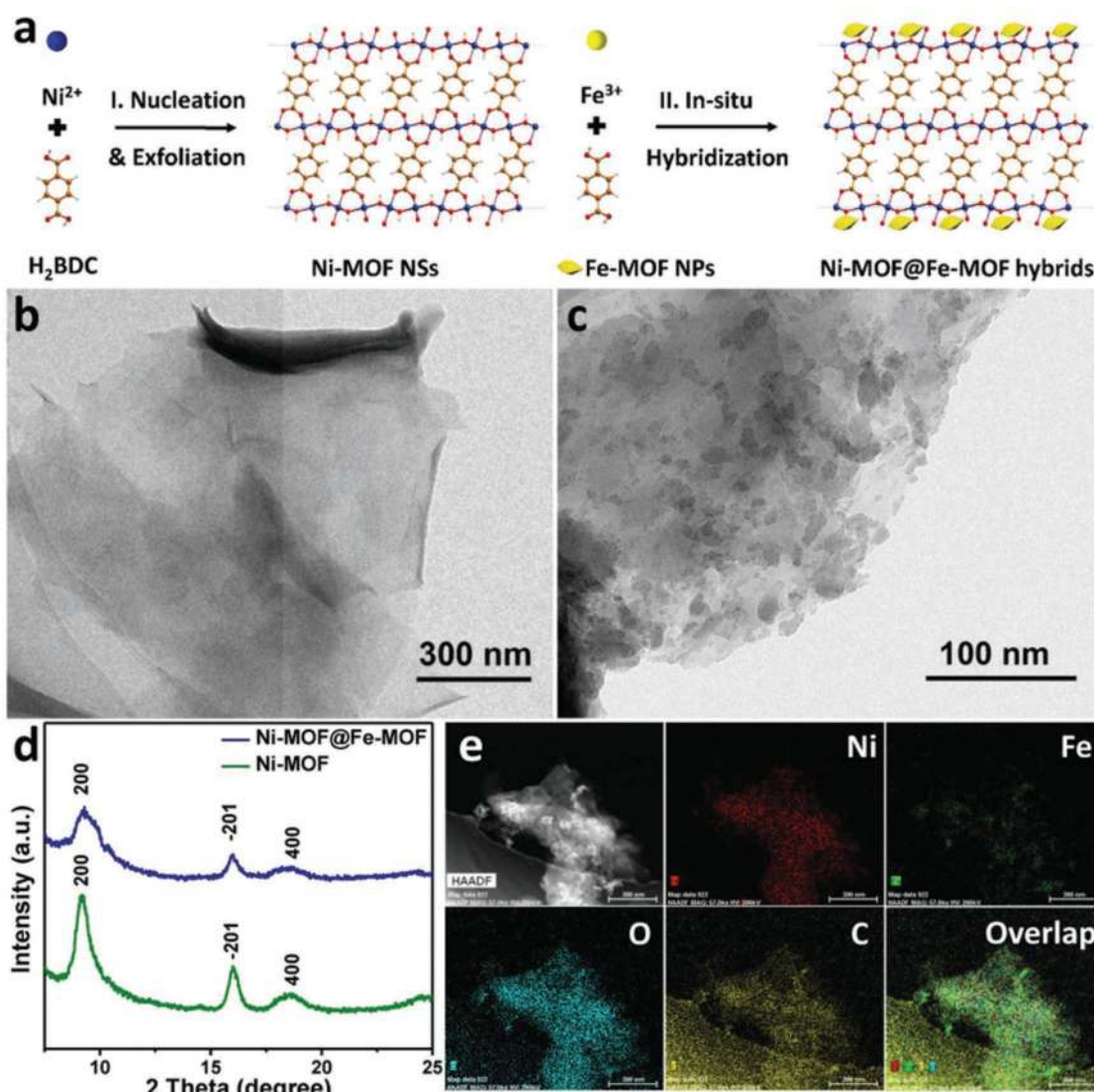
Figure 22. a) Synthesis of Ni-MOF@Fe-MOF hybrid nanosheets; TEM images of b) Ni-MOF and c) Ni-MOF@Fe-MOF hybrid; d) XRD patterns of Ni-MOF and Ni-MOF@Fe-MOF hybrid; e) HAADF-STEM image and corresponding EDS elemental mapping images of Ni-MOF@Fe-MOF hybrid. Reproduced with permission.[101] Copyright 2018, Wiley.

electrocatalysts.[107,108] Furthermore, with respect to the onset potential for the OER, NiPc-MOF catalyst showed much superior activity to the noble metal-based OER catalysts.[109,110] Control experiments using monomer 2,3,9,10,16,17,23,24-octa-tosylamidophthalocyaninato nickel(II) (NiPc-NHTs) and blank FTO show current onsets for OER at 1.65 and 1.80 V, respectively, that are much more positive than the value from NiPc-MOF. The excellent OER performance of NiPc-MOF catalyst over the molecular analog suggests unique feature derived from the conductive π-conjugated 2D MOF structure which favors good conductivity and easy accessibility. Long-term chronopotentiometry measurements using NiPc-MOF were conducted setting a current density of 1.0 mA cm^{-2}. The temporal profile data indicate that the catalytic potential decreased slightly at the beginning and subsequently is maintained almost constant at 1.50 V for nearly 50 h. Furthermore, the morphology and structure of the NiPc-MOF did not exhibit considerable changes

after the electrochemical tests as evidenced by comparison of SEM images and Raman spectra of the fresh and used samples.

A porphyrin-based 2D MOF nanodisk was synthesized by formation of a chelate between the TCPP ligand and Zn(II) resulting in the formation of paddle-wheel $Zn_2(COO)_4$ metal nodes as a secondary building unit (**Figure 24**).[103] Addition of BP (BP: 4,4′-biphenyldicarboxylic acid) during the metallation of TCPP causes the formation of a 2D Zn-TCPP(BP) MOF (Figure 24). ICP-MS analysis indicated that the molar ratio of Zn to TCPP in Zn-TCPP(BP) is ≈3:1. The as-synthesized Zn-TCPP(BP) showed a BET surface area of 483 m^2 g^{-1}. The SEM image of an analogous Zn-TCPP MOF shows nanodisk morphology with a lateral size of 5.0 ± 1.0 μm (**Figure 25**). The presence of BP as a nucleation modulator in Zn-TCPP(BP) causes the development of a well-defined 2D layered structure with a lateral size of 0.6 ± 0.2 μm. In the case of Zn-TCPP(BP), TEM images showed the existence of 2D MOF nanodisks with

**ADVANCED
SCIENCE NEWS**

www.advancedsciencenews.com

**ADVANCED
MATERIALS**

www.advmat.de
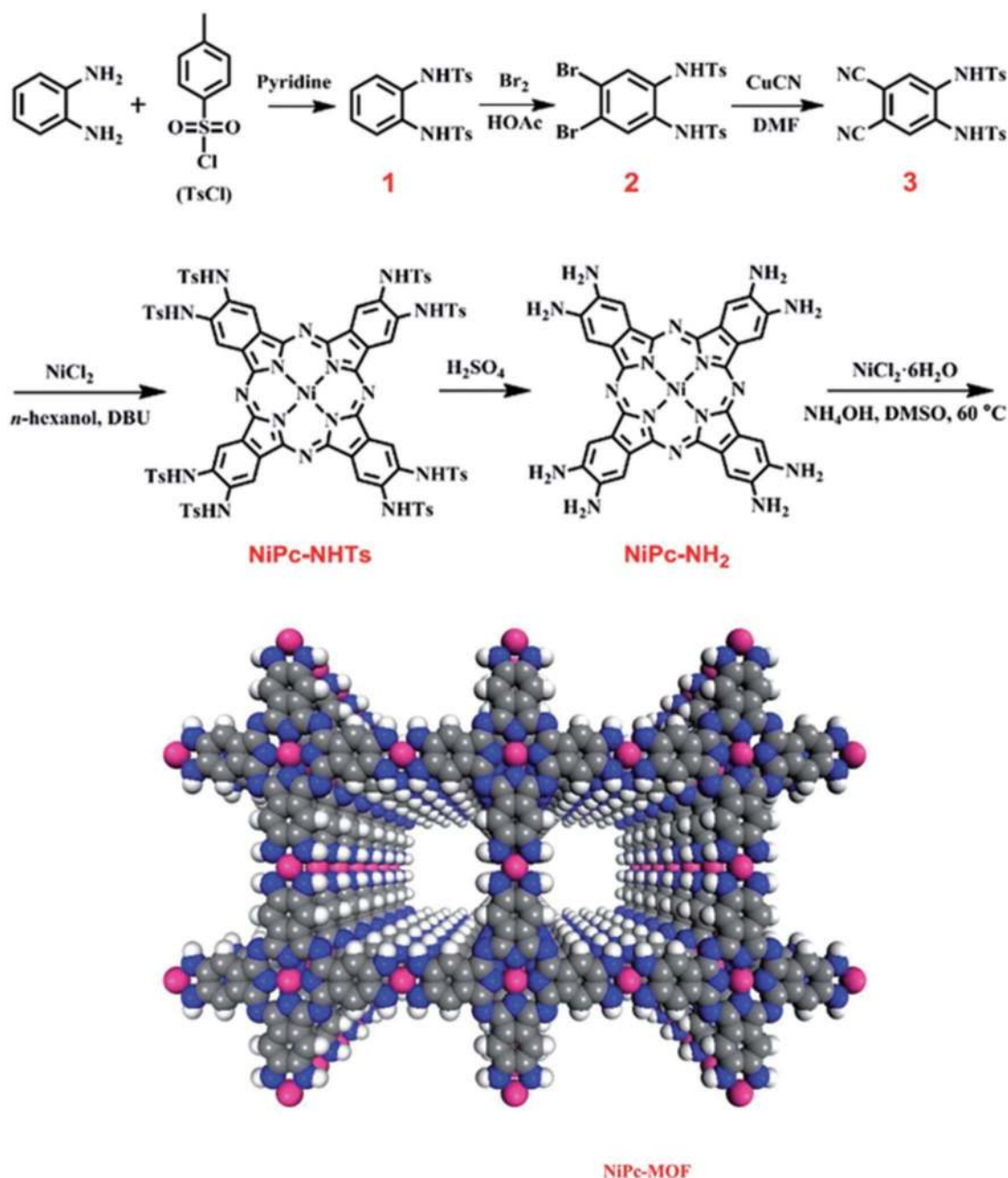
Figure 23. Synthesis route and structure of NiPc-MOF. Reproduced with permission.[102] Copyright 2018, Royal Society of Chemistry.

an average number of nanosheets in the nanodisk particles of 7 ± 3 (Figure 25). The corresponding HRTEM images indicated that the interplanar distance of the lattice fringes in Zn-TCPP(BP) is 1.63 nm with a pore size of 1.18 nm, which agrees with the (100) plane of Zn-TCPP(BP). The Zn-TCPP(BP) nanodisk exhibited very high electrochemical sensing activity toward nitrite with a detection limit of 0.26×10^{-6} M. The high sensitivity achieved by Zn-TCPP(BP) is presumably a consequence of the site isolation, the periodic distribution of porphyrin units in the framework and the sandwich structure of the Zn-TCPP(BP) nanodisk which increased the accessible active sites.

Furthermore, the low detection limit should also be due to the large contact area between the Zn-TCPP(BP) nanodisk and NO_2^- ions.

Ultrathin 2D bimetallic MOF nanosheets (UMOFNs) comprising Cu and Co with BDC as the organic linker were synthesized, and their activity for the hydrogen production from methanol as an anodic electrocatalyst was studied.[104] The SEM images of CuCo-UMOFNs clearly indicated a layered structure. Further, AFM images showed that the thickness of a single layer is ≈3 nm. Linear sweep voltammetry measurements indicated that CuCo-UMOFNs exhibit a remarkably low anodic potential

ADVANCED
SCIENCE NEWS
www.advancedsciencenews.com

ADVANCED
MATERIALS
www.advmat.de
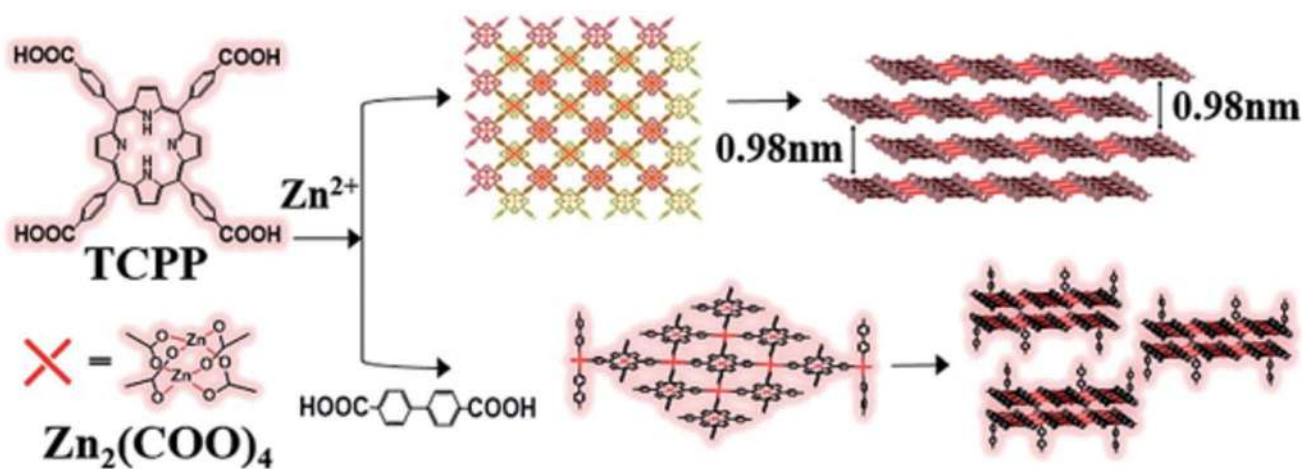
Figure 24. Preparation of the 2D MOF Zn-TCPP nanodisk with and without the assistance of BP as a nucleation modulator. As indicated in the figure, the thickness of the prepared Zn-TCPP nanodisk can be effectively regulated by the presence of BP. Reproduced with permission.[103] Copyright 2018, Royal Society of Chemistry.

of 1.365 V versus RHE at 10 mA cm^{-2} for the electrochemical decomposition of methanol. This anodic potential value measured for CuCo-UMOFNs is much lower than the anodic potential values of some analogous MOFs, particularly those

of Cu-UMOFNs (1.495 V vs RHE) and Co-UMOFNs (1.427 V vs RHE). The average TOF achieved for CuCo-UMOFNs was 19.62 s^{-1}. The stability of CuCo-UMOFNs was assessed by comparing the profiles of 2000 consecutive cyclic voltammetry
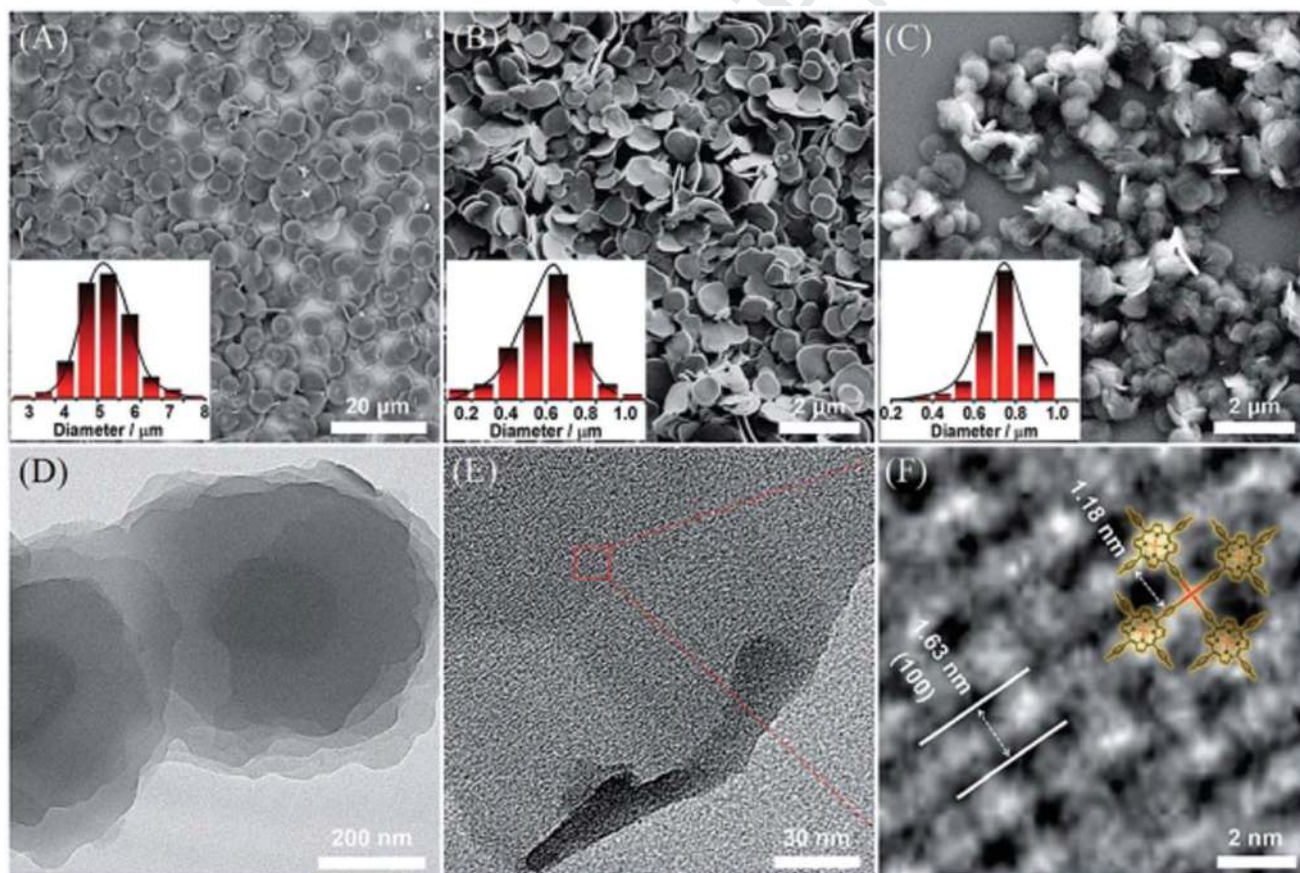
Figure 25. Morphology and lateral size of A) Zn-TCPP, B) Zn-TCPP(BP), and C) Zn-TCPP(BA) (BA: benzoic acid) MOF nanodisks. Inset: Lateral size distribution histograms of the three nanodisks. D) TEM and E,F) HRTEM images of the prepared Zn-TCPP(BP) MOF nanodisk. Reproduced with permission.[103] Copyright 2018, Royal Society of Chemistry.

ADVANCED
SCIENCE NEWS
www.advancedsciencenews.com

ADVANCED
MATERIALS
www.advmat.de

scans without observation of noticeable changes and by chrono-amperometry measurements. The enhanced activity of CuCo-UMOFN compared to its analogous 3D materials was justified by the presence of numerous coordinatively unsaturated metal sites exposed on the surfaces of the 2D structure. However, this rationalization does not consider the possible synergy derived from the bimetallic nature of CuCo-UMOFN.

In an interesting theoretical study aimed at predicting the electrocatalytic activity, first principles calculations were performed for 36 different configurations of 2D π-conjugated MOFs for electrocatalytic HER.[111] Among these MOFs, six MOF nanosheets having metal–ligand interactions like Rh–N, Ir–N, Ru–O, Rh–O, Co–S, and Pd–S were predicted to be efficient single-site catalysts to promote the HER. Specifically, Rh–N nanosheet was identified as the optimal catalyst due to its lowest activation barrier (0.53 eV). These theoretical calculations are likely to trigger experimental research to synthesize 2D MOFs with these types of single sites in their structure to confirm the theoretical model and to obtain highly active anodic catalysts for HER. Of specific interest are those based on Earth-abundant metals.

3.3. Photocatalysis

This section describes the photocatalytic applications of 2D MOFs that have been reported in recent years. **Table 7** summarizes various 2D MOFs as photocatalysts for wide range of reactions along with their activity and convincing evidences for their stability under the reported experimental conditions. As can be seen in Table 7, the number of studies on the use of 2D MOFs as photocatalysts is still limited, particularly compared with that of 3D MOFs that are widely reported in photocatalysis. It should also be commented that data about the bandgap and how the 2D/3D dimensionality affects the energy of the conduction and valence are still missing, but it will be very important for the fast progress of this area.

2D MOFs are also especially suited as photocatalysts as their morphology allows obtaining films with the optimal thickness to achieve complete illumination of all their chromophores and, at the same time, present the highest surface for interaction with substrates. In one of the examples of 2D MOFs as photocatalysts, a new metal–organic layer (MOL) with the composition $[Hf_6(\mu_3-O)_4(\mu_3-OH)_4(HCO_2)_6(TPY)_2]$ was synthesized by replacing the BTB ligand by (4′-(4-benzoate)-(2,2′,2″-terpyridine)-5,5″-dicarboxylate) (TPY) in $[Hf_6(\mu_3-O)_4(\mu_3-OH)_4(HCO_2)_6(BTB)_2]$ MOLs.[112] The presence of TPY

ligands offers the possibility of introducing other transition metals by coordination with TPY through postfunctionalization (**Figure 26**). In addition, the six formate groups in the secondary building unit of $[Hf_6(\mu_3-O)_4(\mu_3-OH)_4(HCO_2)_6]$ can also be readily exchanged with other functional molecules having carboxylate-anchoring groups. TEM images of $[Hf_6(\mu_3-O)_4(\mu_3-OH)_4(HCO_2)_6(TPY)_2]$ showed the presence of films of ≈0.2 μm with wrinkles. Powder XRD patterns were consistent with 3,6-connected kgd topology. AFM images indicated a thickness of 1.4 ± 0.2 nm, corresponding to the van der Waals height of a single layer of Hf_6 SBU. After the synthesis of $[Hf_6(\mu_3-O)_4(\mu_3-OH)_4(HCO_2)_6(TPY)_2]$, Fe(II) species were coordinated to the TPY ligand in this MOL. ICP-OES analysis showed a notable Fe loading of 10.35 wt%. The SBUs of Fe-MOLs were further modified by reacting with monocarboxylic acids varying in their hydrophilicity/hydrophobicity ratio, such as gluconic acid (GA), oleic acid (OA), caprylic acid (CA), propionic acid (PA), 5-aminovaleric acid (5-AA), 7-aminoheptanoic acid (7-AA), O-[2-(2-methoxy-ethoxy)ethyl]glycolic acid (O-GA), and protoporphyrin IX (PPIX).

The catalytic activity of the series of single layer 2D Fe^{II}MOLs was tested in oxidative C–H activation of tetrahydrofuran using a blue LED lamp (**Scheme 14**). The oxidation reaction resulted in the formation of butyrolactone (BTL) and 2-hydroxytetrahydrofuran (2-OH-THF). Fe^{II}-MOL exhibited a BTL selectivity of 57% with a total TON of $(8.2\pm0.3)\times10^2$. A control experiment was performed using MOLs lacking Fe^{II} chromophores, observing no activity, thus supporting the role of TPY-Fe^{II} complexes as the photocatalytic center. In addition, an analogous homogeneous TPY-Fe^{II} complex afforded a TON value of 45, indicating a fast deactivation of the molecular complex through intermolecular aggregation, proving the advantage of site isolation and immobilization of the molecular TPY-Fe^{II} complexes in the MOL rigid lattice. OA-Fe^{II}MOL with a hydrophobic surface showed 57% BTL selectivity, while the BTL selectivity was enhanced to 79% for O-GA-Fe^{II}-MOL having lower hydrophobicity. Interestingly, GA-Fe^{II}MOLs with high hydrophilicity exhibited 100% selectivity toward BTL with a TON of $(5.3\pm0.3)\times10^2$ under identical reaction conditions. This high product selectivity was mainly due to the optimal residence time of reaction intermediates in the hydrophilic microenvironment of catalytic centers. These results show the potential of tuning substrate and product adsorption properties on the nanosheets by the proper choice of the monocarboxylic ligand to control the selectivity of the photocatalytic reaction. Leaching analyses suggest that the reaction was heterogeneous in nature. TEM and PXRD studies indicated that the GA-Fe^{II}-MOL photocatalyst maintained identical nanosheet morphology after the reaction.

Table 7. List of 2D MOFs as photocatalysts.

2D MOFs	Preparation method	Reaction	Activity	Stability evidence	Ref.
GA-Fe^{II}MOLs	Solvothermal	C–H activation of tetrahydrofuran	TON: $(5.3\pm0.3)\times10^2$	TEM, XRD, leaching	[112]
Zr-RuBPY	Solvothermal	[2 + 2] cycloadditions of bis(enones)	82% yield with >10:1 diastereomeric ratio	ICP-MS, XRD	[113]
IrBPY-MOL	Heating assisted	Photopolymerization of methyl methacrylate	78% yield of poly(methyl methacrylate)	XRD	[114]
Zn-MOF/ZIF-67	Solvothermal	Photoreduction of CO_2	TON: 117.8 (CO) 11.6 (H_2)	Reuse, XRD, UV-vis	[115]
Zr-MOF-FA	Pseudoassembly–disassembly	Photooxidation of 1,5-dihydroxynaphthalene to juglone	Zr-MOF-FA showed higher activity than 3D analog	XRD, TEM	[116]

ADVANCED
SCIENCE NEWS
www.advancedsciencenews.com

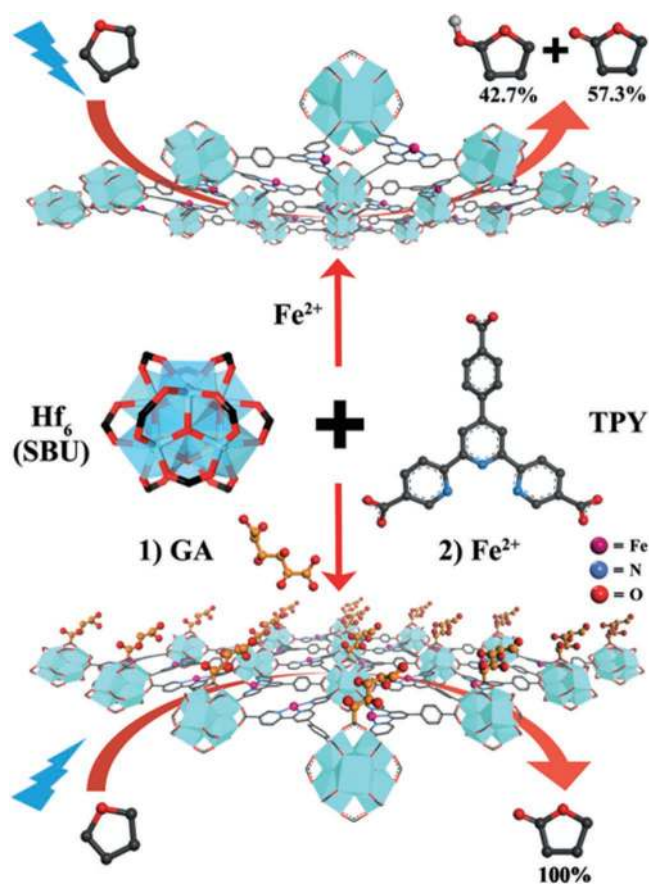ADVANCED
MATERIALS
www.advmat.de

Figure 26. Illustration of the difference in selectivity upon modification of the SBUs of Fe^{II}-MOLs with GA for the photocatalytic oxidation of tetrahydrofuran. Reproduced with permission.[112] Copyright 2017, Wiley-VCH.

The mechanism for the photocatalytic aerobic oxidation of THF was also investigated. In a control experiment, the photochemical reaction of Ru(bpy)$_3^{2+}$ with THF did not oxidize under the photocatalytic conditions and hence the involvement of singlet oxygen was ruled out since Ru(bpy)$_3^{2+}$ is a well-known photosensitizer to generate singlet oxygen. On the other hand, the involvement of other radical species, like hydroxyl or hydroperoxyl free radicals, from activated oxygen was studied by quenching experiment with 5,5-dimethyl-1-pyrroline-N-oxide (DMPO) as a radical trap, whereby no DMPO adducts could be detected by ESR spectroscopy. Considering these preliminary results and the high selectivity to BTL, a photoinduced electron transfer mechanism as indicated in **Scheme 15** was proposed. Initially, TPY-Fe^{II} 1) comes oxidized to TPY-Fe^{III} 2) oxygen in the presence of protons, followed by photochemical
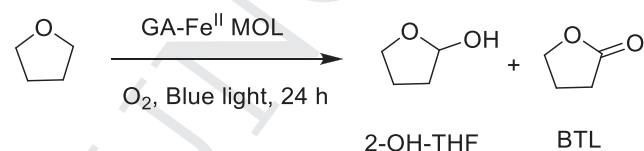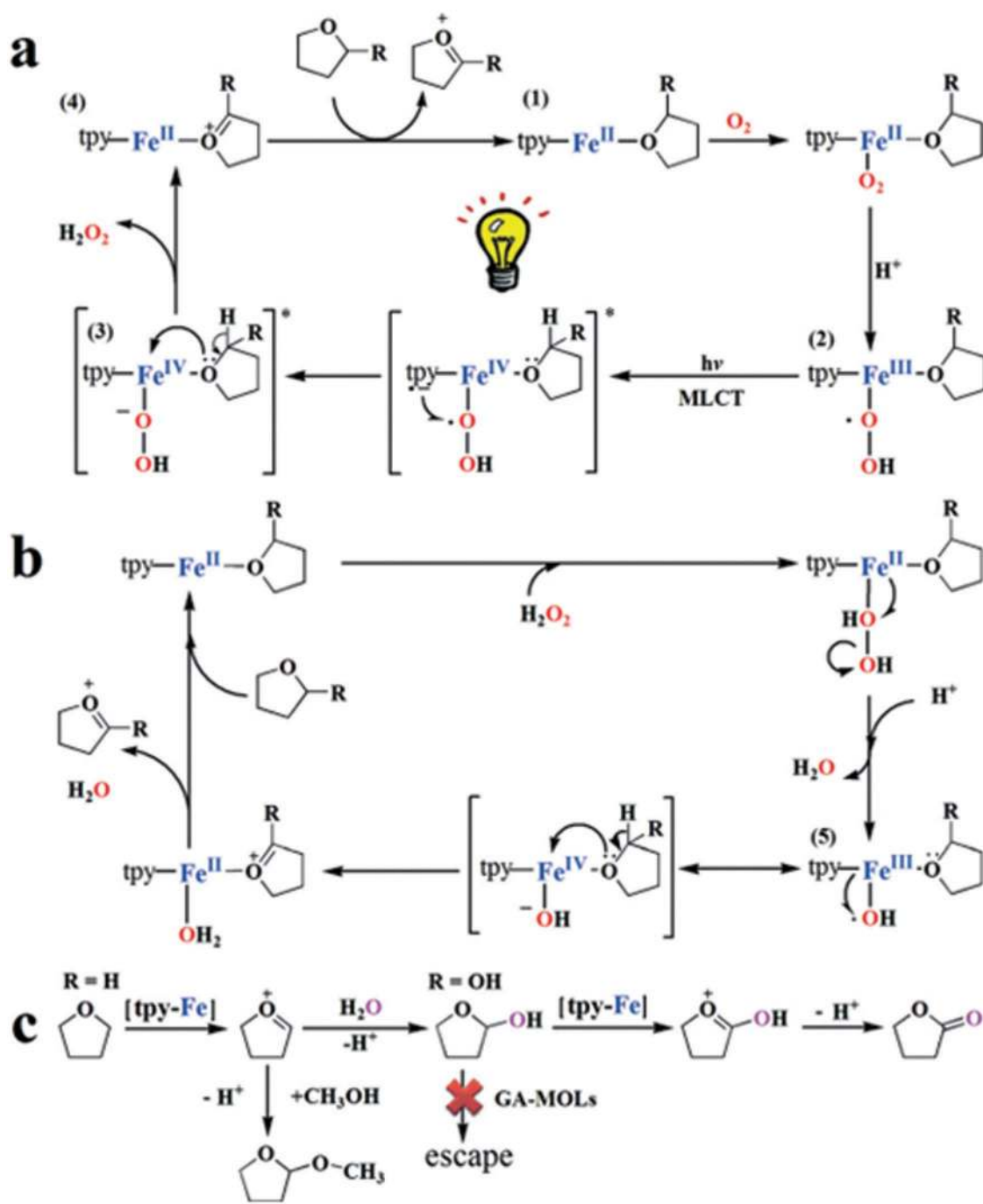

Scheme 14. Photocatalytic oxidation of tetrahydrofuran using GA-Fe^{II} MOL catalyst.

oxidation of THF by TPY-Fe^{III}-$^\bullet$OOH. The photochemical oxidation of THF by TPY-Fe^{III}-$^\bullet$OOH would occur via metal to ligand charge transfer excited state to generate TPY-Fe^{IV}-$^-$OOH 3). Subsequently, the Fe^{IV} active center would oxidize coordinated THF through two-electron transfer to form Fe^{II}-coordinated oxonium cation 4) which would be, then, attacked by water to provide 2-OH-THF (Scheme 15a).

In an alternative pathway, TPY-Fe^{II} species would react also with generated H$_2$O$_2$ via Fenton-like process to generate TPY-Fe^{III}-$^\bullet$OOH adduct which is in resonance to TPY-Fe^{IV}-$^-$OH that oxidizes THF to oxonium cation through two-electron transfer (Scheme 15b). The higher redox potential of $^\bullet$OH/$^-$OH (1.90 V vs SHE compared to that of $^\bullet$OOH/$^-$OOH (0.75 V vs SHE) favors direct oxidation of Fe^{III} to Fe^{IV} in the absence of photoexcitation. The formation of BTL can be explained from the adsorption of 2-OH-THF onto the Fe centers and subsequent further oxidation by both the TPY$^{\bullet-}$Fe^{IV}-$^-$OOH and TPY-Fe^{IV}-$^-$OH as shown in Scheme 15c.

In another example of a metal-organic layer photocatalyst, Zr-BPY MOL was prepared by reaction of ZrCl$_4$, 4′,6′-bis-(4-benzoic acid)-(2,2′-bipyridine)-5-carboxylic acid (H$_3$BPY) and formic acid in a water-DMF mixture (**Figure 27**). TEM images indicated that the Zr-BPY layer thickness was 1–2 nm with an appearance of wrinkled nanosheets. Powder XRD showed a kgd topology. Later, Zr-BPY was reacted with Ru(bpy)$_2$Cl$_2$ to obtain Zr$_6$(μ_3-O)$_4$(μ_3-OH)$_4$(HCO$_2$)$_6$(BPY)$_2$[Ru(bpy)$_2$Cl$_2$]$_{1.42}$ (Zr-RuBPY MOL).[113] This material exhibits a characteristic absorption at 460 nm due to the excitation of the Ru^{2+} polypyridyl complex. ICP-MS analysis indicated the Ru:Zr ratio of 1:4.2 that corresponds to the metallation of 71% of BPY sites. TEM and powder XRD indicated that the MOL morphology and topology were not altered by the postsynthetic metallation with Ru^{2+}. AFM images revealed the monolayer nature with an average thickness of ≈1.2 nm. The photocatalytic performance of Zr-RuBPY was examined in the intramolecular [2 + 2] cycloadditions of bis(enones) using 410 nm LED as the irradiation source (**Scheme 16**) with LiBF$_4$ as the Lewis acid to activate enone and diisopropylethylamine as the electron donor and affording the meso diastereomer of the cyclobutane bicyclic dione in 82% yield with >10:1 diastereomeric ratio. Although the activity of Zr-RuBPY was comparable to that of the homogeneous Ru(bpy)$_3^{2+}$ complex, Zr-RuBPY has the advantage of being recoverable from the reaction mixture by filtration and the possibility of reusing the material. In contrast to the photocatalytic performance of 2D Zr-RuBPY, Ru(bpy)$_3^{2+}$-doped inside UiO-67 MOF did not promote the [2 + 2] cycloaddition reaction under identical conditions due to small MOF pores precluding the formation of a sterically demanding transition state. Also, Zr-BPY was unable to catalyze this reaction. ICP-MS analysis showed no noticeable leaching of Ru and Zr. Zr-RuBPY maintained its photocatalytic activity as well as its diastereomeric ratio in three consecutive cycloaddition reactions. Powder XRD of the recovered Zr-RuBPY MOL showed no difference in the pattern. Zr-RuBPY also promotes under identical conditions [2 + 2] cycloaddition for a series of bis(enones) as substrates, with yields ranging from 73% to 92% (**Table 8**). On the contrary, the 3D analog UiO-Ru(bpy)$_3$ gave less than 10% of the desired products, thus showing the superior activity of 2D Zr-RuBPY MOL as cycloaddition photocatalyst. Furthermore, Zr-RuBPY

Scheme 15. Proposed mechanism for the photocatalytic oxidation of THF a) O_2-dependent and b) H_2O_2-dependent oxidation reactions and c) oxidation of THF into 2-OH-THF and BTL. Reproduced with permission.[112] Copyright 2017, Wiley-VCH.

catalyzed the intermolecular [2 + 2] cross cycloaddition of acyclic enones and a Michael acceptor to afford cyclobutyl diones in 75% yield with a 6:1 diastereomeric ratio. Again, the related 3D material, UiO-Ru(bpy)₃ exhibited 12% cyclobutyl dione yield, which is considerably lower than the yield obtained with Zr-RuBPY MOL. This notable difference in the activity between Zr-RuBPY and UiO-Ru(bpy)₃ was attributed to restricted diffusion of reactive intermediates within the MOF channels, while Zr-RuBPY MOLs favors free diffusion of intermediates.

The mechanism involves the generation of photoexcited Zr-RuBPY upon light irradiation which reacts with DIPEA, producing [Ru(BPY)₃]⁺ species. This Ru⁺ cation is able to transfer one electron to the Li⁺-activated enones to generate highly reactive radical anion which subsequently undergoes intermolecular [2 + 2] cycloaddition and finally transfers one electron to
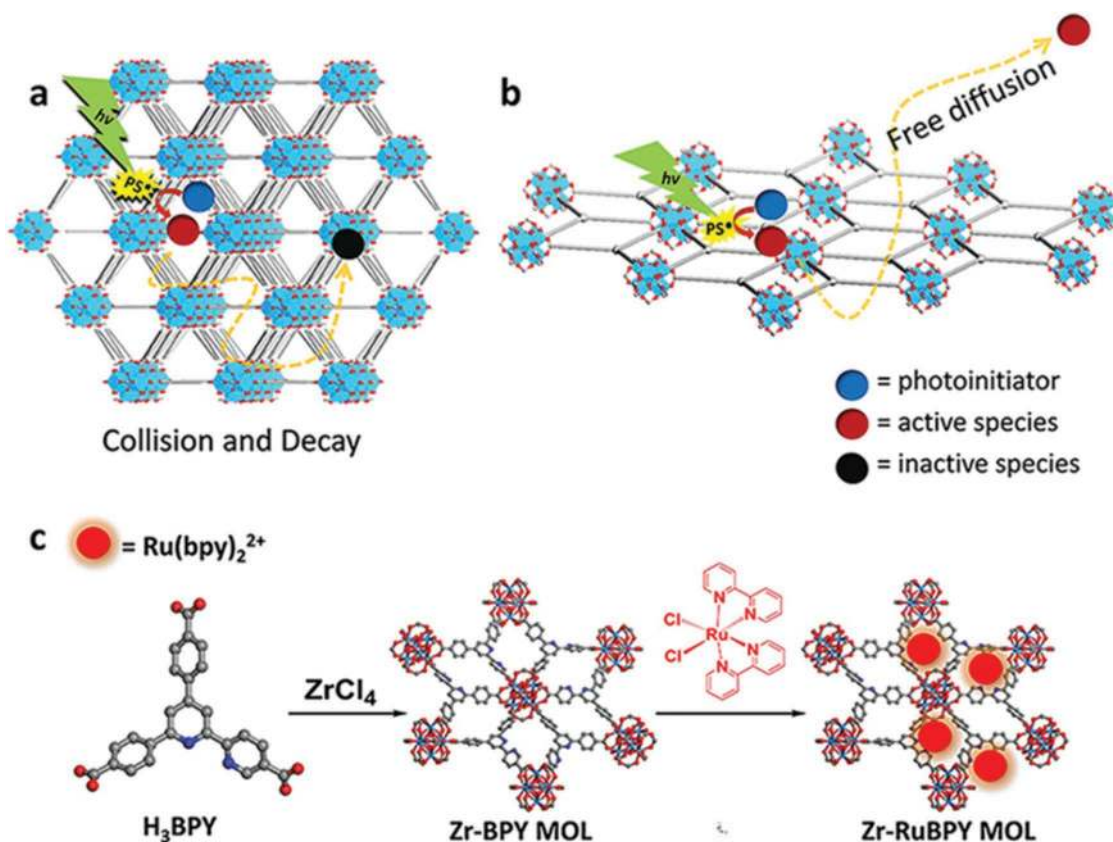
Figure 27. a) Restricted diffusion of reactive species in 3D MOFs versus free access in b) 2D MOLs for their use as photocatalysts. c) Schematic showing the synthesis of Zr-RuBPY MOL. Reproduced with permission.[113] Copyright 2018, Wiley-VCH.

the bis(enones) or other electron acceptor species present in the medium (**Scheme 17**a). A similar approach was also proposed for crossed [2 + 2] cycloadditions of acyclic enones under the present experimental conditions (Scheme 17b).

An analogous BPY-MOL containing Ir material with the formula of $Hf_6(\mu_3\text{-}O)_4(\mu_3\text{-}OH)_4(HCO_2)_6(BPY)_2[Ir\text{-}(ppy)_2Cl]_{1.56}$ (IrBPY-MOL) was prepared as shown in **Figure 28** by reaction of H_3BPY with $HfCl_4$ followed by treatment with iridium dimers, $Ir_2(ppy)_4Cl_2$.[114] TEM images indicated highly dispersed wrinkled sheets of BPY-MOL characteristic of a few hundred nanometers in size. Powder XRD patterns of BPY-MOL and IrBPY-MOL showed good crystallinity, exhibiting characteristic peaks of 2D kgd topology

(Figure 28). ICP-MS showed 78 mol% iridium loading. The catalytic activity of IrBPY-MOL was studied in the photopolymerization of methyl methacrylate using a blue light-emitting diode (410 nm) through atom-transfer radical polymerization with ethyl α-bromophenylacetate as the coinitiator. IrBPY-MOL (0.02% Ir) afforded a 78% yield of poly(methyl methacrylate) with a molecular weight of 16 200 g mol^{-1} and a low polydispersity index (PDI) of 1.27. In contrast, the activity of IrBPY (the ligand present in BPY-MOL) and IrUiO-69 with 0.02% iridium loading showed ≈66% and 40% yield of poly(methyl methacrylate), respectively, under similar conditions. These photocatalytic data showing the different performance of IrBPY-MOL with respect to its molecular or 3D analogs suggests that the reactants are able to reach active sites on 2D MOLs without diffusion barrier. Powder XRD analysis confirmed the high crystallinity of IrBPY-MOL after five cycles with minor decay in the polymerization yields and without diminution of the polymer molecular weight. It could have been convenient, however, to characterize by appropriate spectroscopic and microscopic techniques the five times used IrBPY-MOL to determine the main deactivation cause. Also, further studies are required to elucidate the reaction mechanism, particularly, the possibility of photoinduced electron
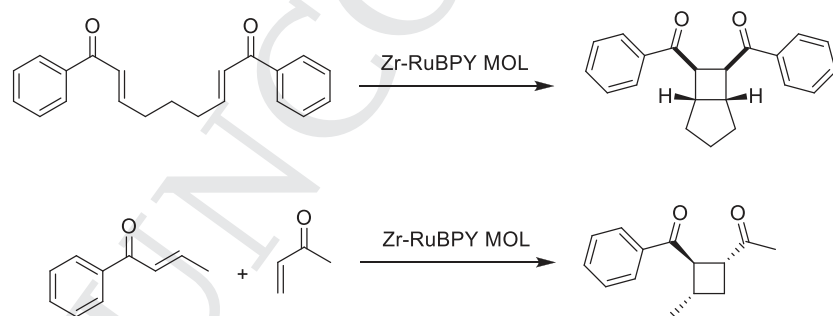
Scheme 16. Zr-RuBPY MOL-catalyzed [2 + 2] photocycloaddition.

Table 8. Activity data for the [2 + 2] intramolecular cycloadditions of bis(enones) using Zr-RuBPY and UiO-Ru(bpy)₃ as photocatalysts (Reproduced with permission.[113] Copyright 2018, Wiley-VCH).

(R = H, **a**; R = Cl, **b**; R = Br, **c**; R = tBu, **d**; R = OMe, **e**)
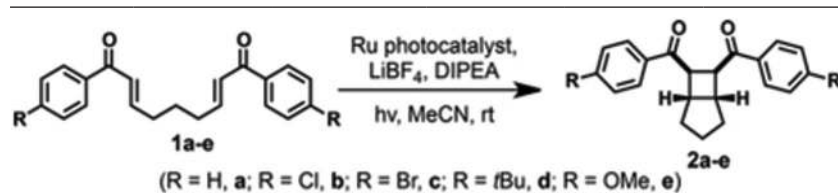
Entry[a]	R	Catalyst	Time [h]	Yield [%][b]	d.r.[c]
1	H	Zr-RuBPY	3	82	>10:1
2		UiO-Ru(bpy)₃	8	n.r.	–
3	Cl	Zr-RuBPY	3	86	>10:1
4		UiO-Ru(bpy)₃	3	9	–
5	Br	Zr-RuBPY	3	92	>10:1
6		UiO-Ru(bpy)₃	3	n.r.	–
7	tBu	Zr-RuBPY	12	79	10:1
8		UiO-Ru(bpy)₃	12	<10	–
9	OMe	Zr-RuBPY	6	73	8:1
10		UiO-Ru(bpy)₃	6	<10	–

[a]Reaction conditions: 1 mol% Zr-RuBPY or UiO-Ru(bpy)₃, 2 equiv. DIPEA, 2 equiv. LiBF₄, 6 mW cm⁻² 410 nm LED, MeCN (0.1 M); [b]Isolated yields; [c]Diastereomer ratios determined by NMR.

or energy transfer from the excited IrBPY chromophore and initiator or substrate.

An ultrathin 2D Zn-TCPP MOF was synthesized and used for the photocatalytic CO_2 reduction in combination either with a di-nuclear cobalt complex [$Co_2(OH)$ L]$(ClO_4)_3$ (L = N[$(CH_2)_2NHCH_2(m-C_6H_4)$ $CH_2NH(CH_2)$]$_3$N) or with ZIF-67 as the cocatalyst (**Figure 29**).[115] Powder XRD proved the formation of the Zn-MOF nanosheets showing a pattern identical to the bulk Zn MOFs. TEM images confirmed the existence of ultrathin Zn-MOF nanosheets. Furthermore, AFM images indicated that the average thickness of Zn-MOF nanosheets is ≈4.7 nm, indicating that the as-synthesized nanosheets are composed of approximately five layers with an interlayer distance of 0.93 nm. XPS analysis revealed the presence of Zn^{2+} in the Zn-MOF nanosheets. In one of the photocatalytic reactions, the activity of the 2D or 3D Zn-MOF was evaluated in the photoreduction of CO_2 in a MeCN/MeOH/ TEOA solution under visible light irradiation with [$Co_2(OH)L](ClO_4)_3$ as the cocatalyst. The TON measured at 6 h for bulk 3D Zn-MOF in the formation of CO and H_2 was 26.2 and 12.4, respectively, while using 2D Zn-MOF nanosheets under identical conditions, the TON value at the same time was enhanced to 68.7 and 15.6 for CO and H_2, respectively (**Figure 30**). In addition, the selectivity
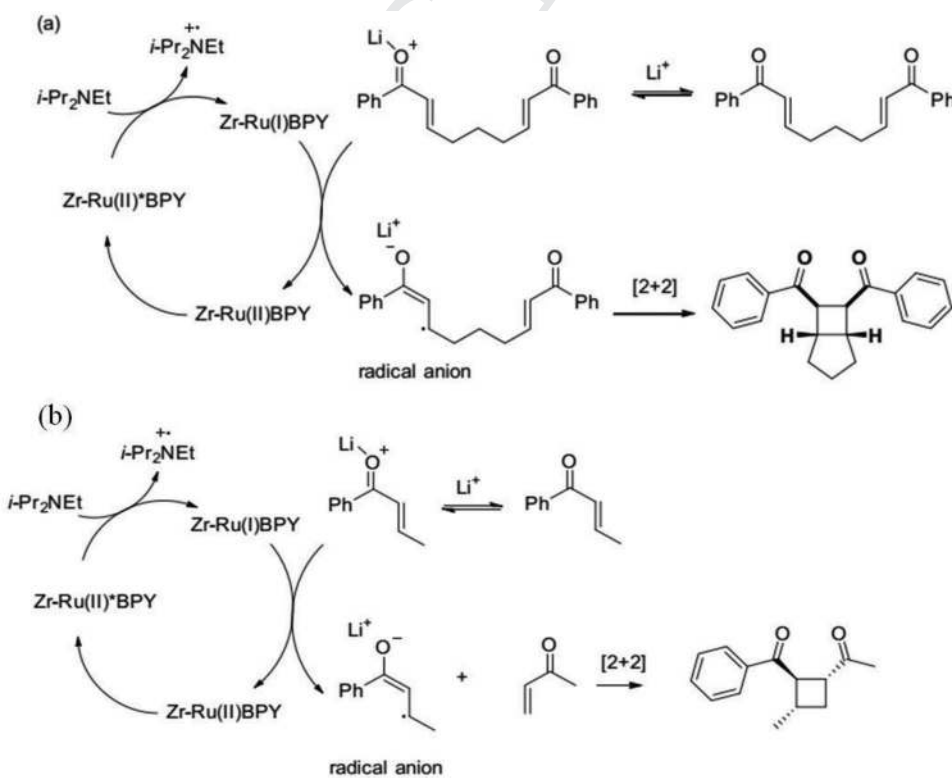
Scheme 17. Proposed mechanism using Zr-RuBPY as photocatalyst for a) intermolecular [2 + 2] cycloadditions of bis(enones) and b) crossed [2 + 2] cycloadditions of acyclic enones. Reproduced with permission.[113] Copyright 2018, Wiley-VCH.

ADVANCED
SCIENCE NEWS
www.advancedsciencenews.com

ADVANCED
MATERIALS
www.advmat.de
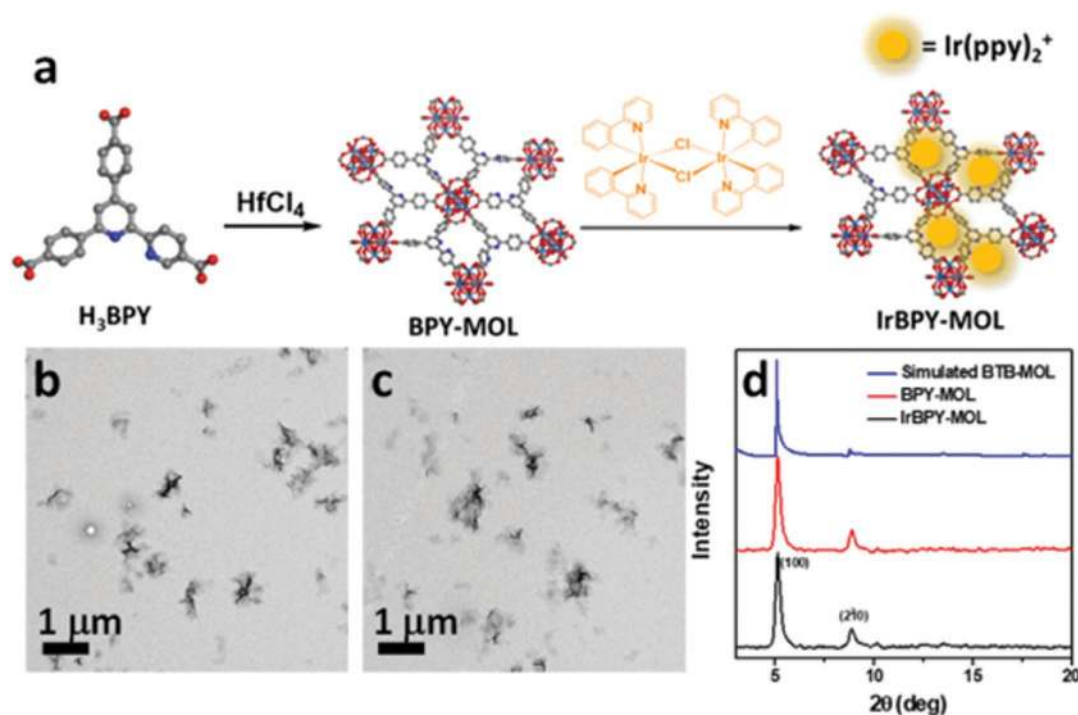
Figure 28. a) Synthesis of IrBPY-MOL photocatalyst; TEM images of b) BPY-MOL and c) IrBPY-MOL; d) powder XRD patterns of BPY-MOL and IrBPY-MOL in comparison with the simulated PXRD pattern for BTB-MOL. Reproduced with permission.[114] Copyright 2018, American Chemical Society.

toward CO_2 versus H_2O reduction was higher for 2D Zn-MOF nanosheets (81.5%) compared to bulk Zn-MOF (67.9%).

Even more, the combination of Zn-MOF nanosheets with ZIF-67 as the cocatalyst further increased the TON values

significantly to 117.8 and 11.6 for CO and H_2, respectively (Figure 30), corresponding to 91% selectivity to CO. In comparison, the use of 3D Zn-MOF with ZIF-67 provided TON values of 63.6 and 7.5 for CO and H_2, respectively, with
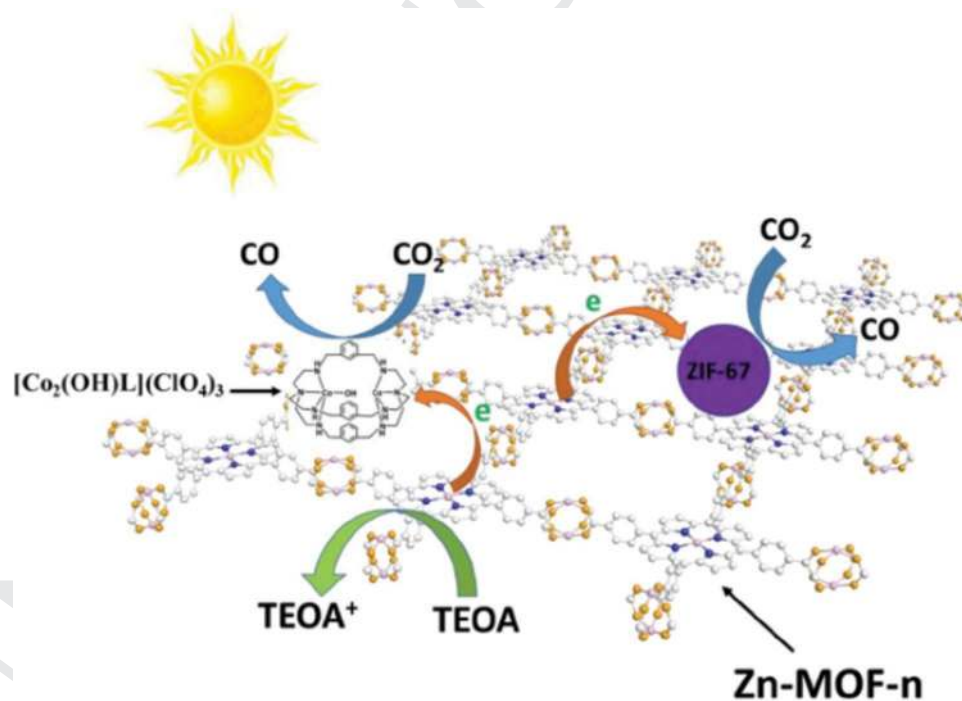
Figure 29. Zn-MOF nanosheet/complex or Zn-MOF nanosheet/ZIF-67 (represented as purple circles) system for photocatalytic CO_2 reduction under visible irradiation. Reproduced with permission.[115] Copyright 2018, Elsevier.

ADVANCED
SCIENCE NEWS

www.advancedsciencenews.com

ADVANCED
MATERIALS

www.advmat.de
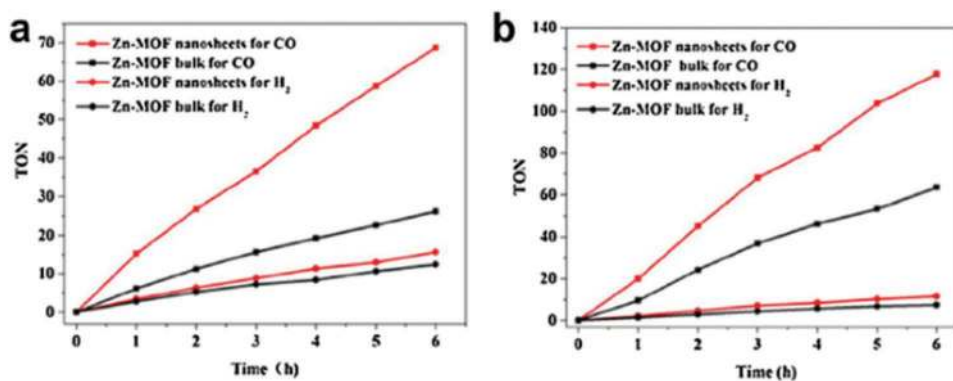
Figure 30. Photocatalytic CO_2 reduction with a) Zn-MOF nanosheet or bulk Zn-MOFs as photosensitizer $[Co_2(OH)L](ClO_4)_3$ as cocatalyst and b) Zn-MOF nanosheet or bulk Zn-MOFs as photosensitizer with ZIF-67 as cocatalyst. Reproduced with permission.[115] Copyright 2018, Elsevier.

selectivity similar to CO (89.5%). This enhanced activity of Zn-MOF nanosheets was ascribed to the more efficient charge separation, higher charge mobility and longer lifetime of photogenerated charge carriers in 2D MOF as evidenced by photoelectrochemical impedance and photoluminescence studies. The Zn-MOF nanosheets were reused for three cycles with some decay in their activity. However, no considerable difference between the fresh and reused Zn-MOF nanosheet samples was observed in powder XRD or UV-visible spectra.

A suitable mechanism was proposed for the photoreduction of CO_2 to CO using Zn-TCPP nanosheets under the present experimental conditions (**Scheme 18**). Thus, excitation of Zn-TCP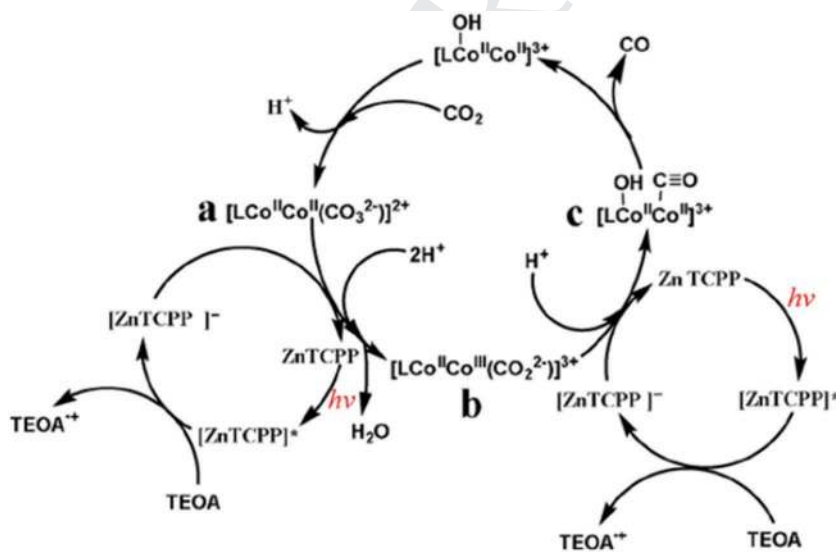P (a unit of Zn-MOF nanosheets) upon visible-light irradiation would give [Zn-TCPP]* which is later reductively quenched with TEOA to afford [Zn-TCPP].$[Co_2(OH)L]^{3+}$ having $Co_2^{II,II}$ species providing a carbonate-bridged complex **a**, as shown in Scheme 18. Complex **a** would undergo proton coupled-electron transfer reduction to generate intermediate **b** by [Zn-TCPP] since the reduction potential of [Zn-TCPP] is more negative than $Co_2^{II,II}/Co_2^{II,I}$ (-1.00 V). Later, the intermediate **b** would undergo another proton coupled electron transfer reduction by

[Zn-TCPP] to give **c** (reduction potential of $Co_2^{II,III}/Co_2^{II,II}$ is −0.85 V vs NHE). Finally, the intermediate **c** would afford CO as the final product under these experimental conditions.

A dynamic pseudoassembly–disassembly (**Figure 31**) mechanism has been employed for the synthesis of ultrathin zirconium porphyrinic MOF nanosheets (UNs) reaching atomic thickness by a one-pot solvothermal reaction between ZrCl₄, Ni-TCPP and formic acid (FA) as the modulator to obtain Zr-MOF nanosheets (UNs-FA).[116] In the pseudoassembly step, FA appears preferentially coordinated with Zr clusters due to its higher concentration compared to the porphyrin ligand (the ratio of FA:Ni-TCPP was 150:1). Over the course of the reaction, the deprotonated Ni-TCPP competed with monocarboxylic acid for coordination with the Zr clusters, forming an intermediate crystal structure containing large quantities of monocarboxylic acid occupying coordination sites that weaken interlayer interactions, making possible the disassembly. Subsequently, the disassembly step involves disaggregation of the layers in the unstable 3D particles, leading to the formation of ultrathin nanosheets. The AFM analysis of the as-prepared UNs-FA indicated the thickness to be 1.48 ± 0.22 nm (**Figure 32**).

The powder XRD pattern showed that the nanosheets exhibit three peaks that are consistent with the presence of PCN-222 single crystals. Further, UNs-FA was uniformly obtained with lateral dimensions of ≈200 nm as shown by TEM images (Figure 32). Gas adsorption measurements revealed that the BET surface area of UNs-FA was 398 m² g⁻¹. The photocatalytic activity of UNs-FA was exploited in the photooxidation of 1,5-dihydroxynaphthalene to juglone using a 300 W Xe lamp (**Scheme 19**). Juglone is an important synthetic precursor in the preparation of herbicides as well as dyes for cloths and inks and a coloring ingredient for foods and cosmetics. The formation of juglone during the reaction can easily be followed by the increase in its characteristic absorption at 419 nm (**Figure 33**). Further, UNs-FA exhibited higher activity than the related bulk 3D PCN-222 analog (Figure 33). The TEM images and powder XRD patterns of

Scheme 18. Proposed mechanism for the photocatalytic CO_2 reduction under visible light irradiation using Zn-MOF nanosheets. Reproduced with permission.[115] Copyright 2018, Elsevier.

**ADVANCED
SCIENCE NEWS**

www.advancedsciencenews.com

**ADVANCED
MATERIALS**

www.advmat.de
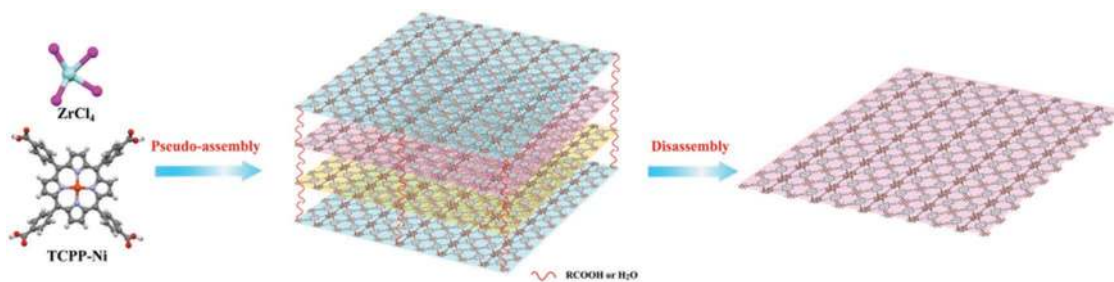
Figure 31. Illustration of the synthesis process of UNs through the pseudoassembly–disassembly strategy. Reproduced with permission.[116] Copyright 2018, Wiley-VCH.

fresh and used UNs-FA did not show any significant change, showing the stability of the nanosheets. The enhanced performance of UNs-FA was believed to derive from the nanometric thickness of the sheets that favors mass transport and a high percentage of exposed photocatalytic active sites on the surface. Further studies are still necessary to clarify the mechanism of the photocatalytic oxidation.

4. Conclusions and Outlook

Even though 2D MOFs have become available only recently, the present review has shown that there has been a surge in

exploiting the properties of these materials beyond their use in membranes, particularly as heterogeneous catalysts. The advantages in terms of higher activity and efficiency that 2D MOFs offer in the field of heterogeneous catalysis, electrocatalysis and photocatalysis have been emphasized. Our aim is to show the still limited number of examples to trigger further research using 2D MOFs in catalysis.

It is clear that the progress of 2D MOFs in catalysis is strongly dependent on the development of suitable preparation procedures of 2D MOFs in sufficient amounts and that the synthesis of 2D materials is still challenging. One of the important limitations in the synthesis of 2D MOFs using either
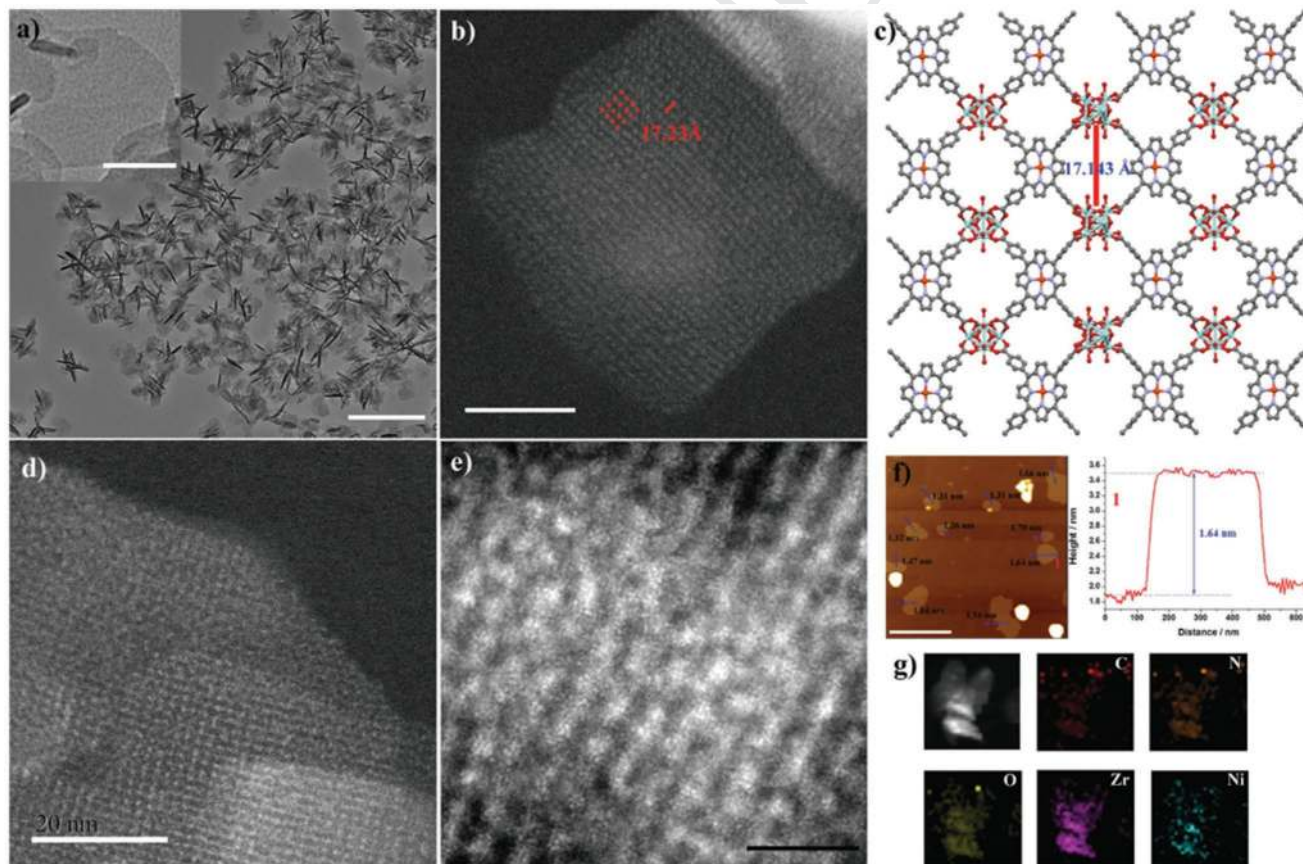
Figure 32. a) TEM image (scale bar: 500 nm) (inset, high-magnification image; scale bar: 50 nm); b,d,e) aberration-corrected HAADF-STEM image (scale bar: b,d) 20 nm; e) 5 nm); c) illustration of the grid-like structure; f) AFM image and corresponding height profile; and g) EDX elemental mapping of UNs-FA. Reproduced with permission.[116] Copyright 2018, Wiley-VCH.

ADVANCED
SCIENCE NEWS
www.advancedsciencenews.com

ADVANCED
MATERIALS
www.advmat.de

Scheme 19. Photocatalytic oxidation of 1,5-dihydroxynapthalene to juglone by UNs-FA.

top-down or bottom-up approaches is the low amount of material that can be prepared per batch that obviously is a serious limitation for any practical application. Although a considerable number of methods have been reported for the synthesis of 2D MOFs, they are still in early stage and a general, scalable method for the synthesis of multigram quantities of 2D MOFs is lacking.
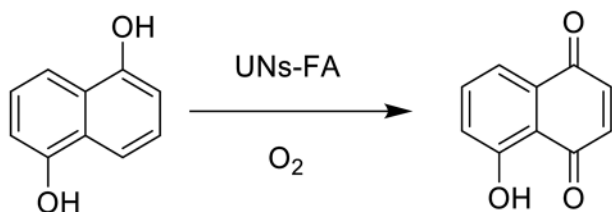
Sufficient additional information of the chemical and thermal stability of 2D MOF is still necessary to consider implementation of these materials for practical applications. Further, stabilization of the nanometric 2D MOF nanosheets is yet another challenge. Surprisingly, a very few reports have tackled this issue providing clear hints for appropriate solvents and stabilizers that can be used, while still preserving catalytic activity. This is a fundamental issue that has to be considered since one of the important structural features of 2D MOF nanosheets is the better accessibility to reactants to reach the unsaturated metal sites without any diffusion barriers and surfactants and stabilizers have to preserve this accessibility without blocking the active sites that would lead to lowering the activity of the 2D MOFs.

At the present, the current data indicate the lack of high quality 2D MOF nanosheets with high crystallinity and large lateral size for the development of device applications. Particularly relevant would be to obtain and characterize single crystals of ultrathin 2D MOFs for technological applications. Theoretical and new characterization methods have to be developed further to characterize 2D MOF nanosheets including the presence of structural defects. However, it is expected that this field will expand in the near future.

It has been commented that 2D MOFs generally show good stability comparable to that of the 3D analogs with a higher activity derived from the accessibility of the and the higher density of coordinatively unsaturated positions and defects around the transition metal nodes. However, there is still a paucity of studies showing that the structural integrity, nanosheet thickness and availability/accessibility of unsaturated metal sites are still present in the used catalyst. It is important to characterize the spent catalyst by appropriate spectroscopic and microscopic techniques to convincingly prove that these unique features of 2D MOFs are retained under the reaction conditions.

The review has presented examples showing that 2D MOFs exhibit enhanced catalytic activity in oxidation reactions, as Lewis acids and even as bifunctional acid/base catalysts. In this regard, it is always necessary to compare the activity of 2D MOF nanosheets with that of other 2D materials. The 2D MOFs can also be used as supports of metal NPs that can be coated by the thin 2D nanoplatelets or occluded within the limited interlayer porosity. In this way, operation of mechanical forces, in addition to the conventional metal–support interaction, cooperate in the stability of the metal NPs against their growth. Considering the well-known role of the support on the catalytic activity of metal nanoparticles heterogeneous catalysts, future directions expand the use of 2D MOFs as support showing how activity and selectivity can be boosted by the composition of the 2D MOF nanosheets. Even more, a cooperation of the metal NP with the 2D MOF can serve to develop multifunctional catalysts mimicking enzymes.

Beyond catalysis, the 2D morphology is clearly especially suited for the preparation of thin films and coatings of substrates with sufficient adhesion and submicrometric thickness. These features are particularly suited for electrocatalytic applications where the conductive electrode must be coated with the catalytic material. Since MOFs are electrical insulators, one way to circumvent the high Ohmic resistance is to decrease the film thickness as much as possible in the nanometric range. Examples have been shown of 2D MOF platelets of a few nanometers thickness that exhibit among the highest levels of electrocatalytic activity for OER or as electrochemical sensors. Considering the general activity of transition metal
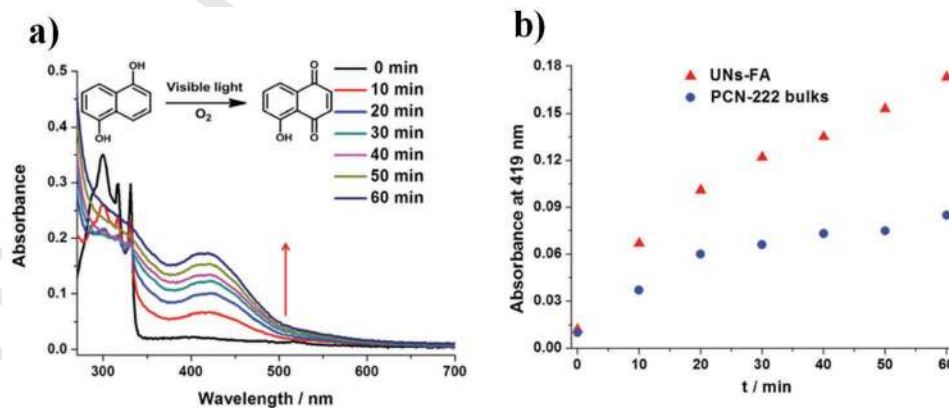

Figure 33. a) Photooxidation of 1,5-dihydroxynaphthalene catalyzed by UNs-FA and b) absorbance of juglone ($\lambda = 419$ nm) as a function of reaction time using UNs-FA and 3D MOF as photocatalyst. Reproduced with permission.[116] Copyright 2018, Wiley-VCH.

oxides and complexes as electrocatalysts, the large variety of MOFs in terms of metal composition and nature of the ligands and the possibility of synthesis by design, it can be forecast that the field of MOFs as electrocatalysts will be increasingly active in the next years. Provided that the adherence and thickness are appropriate, we can predict, based on the activity of metal complexes, that 2D MOFs will be among the most active and stable electrocatalysts for a large number of reactions with the target to become a viable alternative to noble metals as electrocatalysts for reactions that are important in the context of storage of renewable electricity.

Similarly, 2D MOFs will gain more importance in photocatalysis, where the number of examples at the moment is quite low. Since 3D MOFs are currently among the most actively studied photocatalysts, particularly for the production of solar fuels, the scarce number of photocatalytic studies with 2D MOFs is striking. Although suspended powders can be employed as photocatalysts, films immobilized on transparent supports offer advantages in photocatalysis and photo-electrocatalysis, considering the possibility of performing continuous flow irradiation, easy product separation and changing the band potentials by polarization of the photocatalyst with an external bias potential. In this context, the low attention that 2D MOFs have attracted in the area of solar energy conversion into fuels and chemicals is remarkable with just a few reports. It can be foreseen that there will be a burgeoning number of studies in the near future studying the overall water splitting and photocatalytic CO_2 reduction using 2D MOFs, but again catalyst stability should also be considered. Similarly, the combination of membranes and photoelectrodes based on 2D MOFs will be of considerable application in the field of photo-electrocatalysis. There is no doubt that development of catalytic and electro/photocatalytic applications will occur in parallel with the increase in the inventory and the synthesis of new 2D MOFs.

Conflict of Interest

The authors declare no conflict of interest.

[1] H. Li, M. Eddaoudi, M. O'Keeffe, O. M. Yaghi, *Nature* **1999**, *402*, 276.

[2] S. Kitagawa, R. Kitaura, S.-I. Noro, *Angew. Chem., Int. Ed.* **2004**, *43*, 2334.

[3] D. J. Tranchemontagne, J. L. Mendoza-Cortes, M. O'Keeffe, O. M. Yaghi, *Chem. Soc. Rev.* **2009**, *38*, 1257.

[4] G. Ferey, *Chem. Soc. Rev.* **2008**, *37*, 191.

[5] Y. Cui, B. Li, H. He, W. Zhou, B. Chen, G. Qian, *Acc. Chem. Res.* **2016**, *49*, 483.

[6] J. Y. Lee, O. K. Farha, J. Roberts, K. A. Scheidt, S. B. T. Nguyen, J. T. Hupp, *Chem. Soc. Rev.* **2009**, *38*, 1450.

[7] A. Corma, H. Garcia, F. X. Llabres i Xamena, *Chem. Rev.* **2010**, *110*, 4606.

[8] D. Farrusseng, S. Aguado, C. Pinel, *Angew. Chem., Int. Ed.* **2009**, *48*, 7502.

[9] A. H. Chughtai, N. Ahmad, H. A. Younus, A. Laypkov, F. Verpoort, *Chem. Soc. Rev.* **2015**, *44*, 6804.

[10] A. Dhakshinamoorthy, M. Alvaro, H. Garcia, *Chem. Commun.* **2012**, *48*, 11275.

[11] J. Gascon, A. Corma, F. Kapteijn, F. X. Llabres i Xamena, *ACS Catal.* **2014**, *4*, 361.

[12] P. Valvekens, F. Vermoortele, D. De Vos, *Catal. Sci. Technol.* **2013**, *3*, 1435.

[13] L. Ma, C. Abney, W. Lin, *Chem. Soc. Rev.* **2009**, *38*, 1248.

[14] M. Yoon, R. Srirambalaji, K. Kim, *Chem. Rev.* **2012**, *112*, 1196.

[15] Y. Liu, W. Xuan, Y. Cui, *Adv. Mater.* **2010**, *22*, 4112.

[16] U. Mueller, M. Schubert, F. Teich, H. Puetter, K. Schierle Arndt, J. Pastre, *J. Mater. Chem.* **2006**, *16*, 626.

[17] P.-Q. Liao, N.-Y. Huang, W.-X. Zhang, J.-P. Zhang, X.-M. Chen, *Science* **2017**, *356*, 1193.

[18] M. Zhao, K. Yuan, Y. Wang, G. Li, J. Guo, L. Gu, W. Hu, H. Zhao, Z. Tang, *Nature* **2016**, *539*, 76.

[19] D. Sheberla, J. C. Bachman, J. S. Elias, C.-J. Sun, Y. Shao-Horn, M. Dinca, *Nat. Mater.* **2017**, *16*, 220.

[20] M. Rubio-Martinez, M. P. Batten, A. Polyzos, K.-C. Carey, J. I. Mardel, K.-S. Lim, M. R. Hill, *Sci. Rep.* **2015**, *4*, 5443.

[21] K. K. Tanabe, S. M. Cohen, *Chem. Soc. Rev.* **2011**, *40*, 498.

[22] O. K. Farha, I. Eryazici, N. C. Jeong, B. G. Hauser, C. E. Wilmer, A. A. Sarjeant, R. Q. Snurr, S. T. Nguyen, A. Özgür Yazaydın, J. T. Hupp, *J. Am. Chem. Soc.* **2012**, *134*, 15016.

[23] H. Furukawa, K. E. Cordova, M. O'Keeffe, O. M. Yaghi, *Science* **2013**, *341*, 1230444.

[24] J. Kim, B. Chen, T. M. Reineke, H. Li, M. Eddaoudi, D. B. Moler, M. O'Keeffe, O. M. Yaghi, *J. Am. Chem. Soc.* **2001**, *123*, 8239.

[25] M. O'Keeffe, *Chem. Soc. Rev.* **2009**, *38*, 1215.

[26] N. Stock, S. Biswas, *Chem. Rev.* **2012**, *112*, 933.

[27] D. S. Sholl, R. P. Lively, *J. Phys. Chem. Lett.* **2015**, *6*, 3437.

[28] Z. Fang, B. Bueken, D. E. De Vos, R. A. Fischer, *Angew. Chem., Int. Ed.* **2015**, *54*, 7234.

[29] A. Dhakshinamoorthy, Z. Li, H. Garcia, *Chem. Soc. Rev.* **2018**, *47*, 8134.

[30] A. Schaate, P. Roy, A. Godt, J. Lippke, F. Waltz, M. Wiebcke, P. Behrens, *Chem. – Eur. J.* **2011**, *17*, 6643.

[31] R. J. Marshall, C. L. Hobday, C. F. Murphie, S. L. Griffin, C. A. Morrison, S. A. Moggach, R. S. Forgan, *J. Mater. Chem. A* **2016**, *4*, 6955.

[32] F. Vermoortele, B. Bueken, G. Le Bars, B. Van de Voorde, M. Vandichel, K. Houthoofd, A. Vimont, M. Daturi, M. Waroquier, V. V. Speybroeck, C. Kirschhock, D. E. De Vos, *J. Am. Chem. Soc.* **2013**, *135*, 11465.

[33] S. Li, K. Yang, C. Tan, X. Huang, W. Huang, H. Zhang, *Chem. Commun.* **2016**, *52*, 1555.

[34] M. Zhao, Y. Huang, Y. Peng, Z. Huang, Q. Ma, H. Zhang, *Chem. Soc. Rev.* **2018**, *47*, 6267.

[35] J. Zha, X. Zhang, *Cryst. Growth Des.* **2018**, *18*, 3209.

[36] J. Liu, H. Yu, L. Wang, Z. Deng, K. u. R. Naveed, A. Nazir, F. Haq, *Inorg. Chim. Acta* **2018**, *483*, 550.

[37] L. Huang, X. Zhang, Y. Han, Q. Wang, Y. Fang, S. Dong, *J. Mater. Chem. A* **2017**, *5*, 18610.

[38] Y. Peng, Y. Li, Y. Ban, H. Jin, W. Jiao, X. Liu, W. Yang, *Science* **2014**, *346*, 1356.

[39] T. Rodenas, I. Luz, G. Prieto, B. Seoane, H. Miro, A. Corma, F. Kapteijn, F. X. Llabrés i Xamena, J. Gascon, *Nat. Mater.* **2015**, *14*, 48.

[40] X. Wang, C. Chi, K. Zhang, Y. Qian, K. M. Gupta, Z. Kang, J. Jiang, D. Zhao, *Nat. Commun.* **2017**, *8*, 14460.

[41] M. Zhao, Y. Wang, Q. Ma, Y. Huang, X. Zhang, J. Ping, Z. Zhang, Q. Lu, Y. Yu, H. Xu, Y. Zhao, H. Zhang, *Adv. Mater.* **2015**, *27*, 7372.

[42] S. Zhao, Y. Wang, J. Dong, C. T. He, H. Yin, P. An, K. Zhao, X. Zhang, C. Gao, L. Zhang, J. Lv, J. Wang, J. Zhang, A. M. Khattak, N. A. Khan, Z. Wei, J. Zhang, S. Liu, H. Zhao, Z. Tang, *Nat. Energy* **2016**, *1*, 16184.

[43] E. M. Miner, T. Fukushima, D. Sheberla, L. Sun, Y. Surendranath, M. Dinca, *Nat. Commun.* **2016**, *7*, 10942.

[44] N. Kornienko, Y. Zhao, C. S. Kley, C. Zhu, D. Kim, S. Lin, C. J. Chang, O. M. Yaghi, P. Yang, *J. Am. Chem. Soc.* **2015**, *137*, 14129.

[45] C. Li, X. Hu, W. Tong, W. Yan, X. Lou, M. Shen, B. Hu, *ACS Appl. Mater. Interfaces* **2017**, *9*, 29829.

[46] Y. Ning, X. Lou, C. Li, X. Hu, B. Hu, *Chem. – Eur. J.* **2017**, *23*, 15984.

[47] K. S. Novoselov, A. K. Geim, S. V. Morozov, D. Jiang, Y. Zhang, S. V. Dubonos, I. V. Grigorieva, A. A. Firsov, *Science* **2004**, *306*, 666.

[48] H. Wang, L. L. Yu, Y. H. Lee, Y. M. Shi, A. Hsu, M. L. Chin, L. J. Li, M. Dubey, J. Kong, T. Palacios, *Nano Lett.* **2012**, *12*, 4674.

[49] K. Roy, M. Padmanabhan, S. Goswami, T. P. Sai, G. Ramalingam, S. Raghavan, A. Ghosh, *Nat. Nanotechnol.* **2013**, *8*, 826.

[50] C. L. Tan, H. Zhang, *Nat. Commun.* **2015**, *6*, 7873.

[51] H. Zhang, *ACS Nano* **2015**, *9*, 9451.

[52] A. Primo, I. Esteve-Adell, J. F. Blandez, A. Dhakshinamoorthy, M. Álvaro, N. Candu, S. M. Coman, V. I. Parvulescu, H. García, *Nat. Commun.* **2015**, *6*, 8561.

[53] Q.-L. Zhu, Q. Xu, *Chem* **2016**, *1*, 220.

[54] M. Chhowalla, H. S. Shin, G. Eda, L.-J. Li, K. P. Loh, H. Zhang, *Nat. Chem.* **2013**, *5*, 263.

[55] M. Chhowalla, Z. Liu, H. Zhang, *Chem. Soc. Rev.* **2015**, *44*, 2584.

[56] C. Tan, H. Zhang, *Chem. Soc. Rev.* **2015**, *44*, 2713.

[57] J. Zhang, Y. Chen, X. Wang, *Energy Environ. Sci.* **2015**, *8*, 3092.

[58] W.-J. Ong, L.-L. Tan, Y. H. Ng, S.-T. Yong, S.-P. Chai, *Chem. Rev.* **2016**, *116*, 7159.

[59] R. Mas-Balleste, C. Gomez-Navarro, J. Gomez-Herrero, F. Zamora, *Nanoscale* **2011**, *3*, 20.

[60] M. Xu, T. Liang, M. Shi, H. Chen, *Chem. Rev.* **2013**, *113*, 3766.

[61] M. Opanasenko, W. J. Roth, J. Čejka, *Catal. Sci. Technol.* **2016**, *6*, 2467.

[62] W. J. Roth, *Chem. Rev.* **2014**, *114*, 4807.

[63] M. Zhao, Q. Lu, Q. Ma, H. Zhang, *Small Methods* **2017**, *1*, 1600030.

[64] C. Tan, X. Cao, X.-J. Wu, Q. He, J. Yang, X. Zhang, J. Chen, W. Zhao, S. Han, G.-H. Nam, M. Sindoro, H. Zhang, *Chem. Rev.* **2017**, *117*, 6225.

[65] K. Zhao, S. Liu, G. Ye, Q. Gan, Z. Zhou, Z. He, *J. Mater. Chem. A* **2018**, *6*, 2166.

[66] Z. Kang, L. Fan, D. Sun, *J. Mater. Chem. A* **2017**, *5*, 10073.

[67] X. Yang, X. Lin, Y. Zhao, D. Yan, *Chem. – Eur. J.* **2018**, *24*, 6484.

[68] W. Zhao, J. Peng, W. Wang, S. Liu, Q. Zhao, W. Huang, *Coord. Chem. Rev.* **2018**, *377*, 44.

[69] P. Amo-Ochoa, L. Welte, R. Gonzalez-Prieto, P. J. Sanz Miguel, C. J. Gomez-Garcia, E. Mateo-Marti, S. Delgado, J. Gomez-Herrero, F. Zamora, *Chem. Commun.* **2010**, *46*, 3262.

[70] S. Benmansour, A. Abhervé, P. Gómez-Claramunt, C. Vallés-García, C. J. Gómez-García, *ACS Appl. Mater. Interfaces* **2017**, *9*, 26210.

[71] A. Kondo, C. C. Tiew, F. Moriguchi, K. Maeda, *Dalton Trans.* **2013**, *42*, 15267.

[72] T. Kambe, R. Sakamoto, K. Hoshiko, K. Takada, M. Miyachi, J. H. Ryu, S. Sasaki, J. Kim, K. Nakazato, M. Takata, H. Nishihara, *J. Am. Chem. Soc.* **2013**, *135*, 2462.

[73] E.-Y. Choi, C. A. Wray, C. Hu, W. Choe, *CrystEngComm* **2009**, *11*, 553.

[74] E.-Y. Choi, P. M. Barron, R. W. Novotny, H.-T. Son, C. Hu, W. Choe, *Inorg. Chem.* **2009**, *48*, 426.

[75] F. Cao, M. Zhao, Y. Yu, B. Chen, Y. Huang, J. Yang, X. Cao, Q. Lu, X. Zhang, Z. Zhang, C. Tan, H. Zhang, *J. Am. Chem. Soc.* **2016**, *138*, 6924.

[76] M.-H. Pham, G.-T. Vuong, F.-G. Fontaine, T.-O. Do, *Cryst. Growth Des.* **2012**, *12*, 3091.

[77] L. Cao, Z. Lin, F. Peng, W. Wang, R. Huang, C. Wang, J. Yan, J. Liang, Z. Zhang, T. Zhang, L. Long, J. Sun, W. Lin, *Angew. Chem., Int. Ed.* **2016**, *55*, 4962.

[78] G. Zhan, H. C. Zeng, *Adv. Funct. Mater.* **2016**, *26*, 3268.

[79] S. Sakaida, K. Otsubo, O. Sakata, C. Song, A. Fujiwara, M. Takata, H. Kitagawa, *Nat. Chem.* **2016**, *8*, 377.

[80] J. Duan, S. Chen, C. Zhao, *Nat. Commun.* **2017**, *8*, 15341.

[81] M. Bagherzadeh, F. Ashouri, M. Đaković, *J. Solid State Chem.* **2015**, *223*, 32.

[82] Z. Hu, E. Mahmoud Mahdi, Y. Peng, Y. Qian, B. Zhang, N. Yan, D. Yuan, J.-C. Tan, D. Zhao, *J. Mater. Chem. A* **2017**, *5*, 8954.

[83] R. Babu, R. Roshan, Y. Gim, Y. H. Jang, J. F. Kurisingal, D. W. Kim, D.-W. Park, *J. Mater. Chem. A* **2017**, *5*, 15961.

[84] Y.-H. Li, S.-L. Wang, Y.-C. Su, B.-T. Ko, C.-Y. Tsai, C.-H. Lin, *Dalton Trans.* **2018**, *47*, 9474.

[85] Z.-H. Li, L.-P. Xue, L. Wang, S.-T. Zhang, B.-T. Zhao, *Inorg. Chem. Commun.* **2013**, *27*, 119.

[86] L. Hu, G.-X. Hao, H.-D. Luo, C.-X. Ke, G. Shi, J. Lin, X.-M. Lin, U. Y. Qazi, Y.-P. Cai, *Cryst. Growth Des.* **2018**, *18*, 2883.

[87] Y. Cao, Z. Zhu, J. Xu, L. Wang, J. Sun, X. Chen, Y. Fan, *Dalton Trans.* **2015**, *44*, 1942.

[88] F. Guo, B. Yuan, W. Shi, *Inorg. Chem. Commun.* **2017**, *86*, 285.

[89] Z. Lin, N. C. Thacker, T. Sawano, T. Drake, P. Ji, G. Lan, L. Cao, S. Liu, C. Wang, W. Lin, *Chem. Sci.* **2018**, *9*, 143.

[90] S. Xue, H. Jiang, Z. Zhong, Z.-X. Low, R. Chen, W. Xing, *Microporous Mesoporous Mater.* **2016**, *221*, 220.

[91] R. Yan, Y. Zhao, H. Yang, X.-J. Kang, C. Wang, L.-L. Wen, Z.-D. Lu, *Adv. Funct. Mater.* **2018**, *28*, 1802021.

[92] K. Jayaramulu, V. M. Suresh, T. Kumar Maji, *Dalton Trans.* **2015**, *44*, 83.

[93] Y. Huang, M. Zhao, S. Han, Z. Lai, J. Yang, C. Tan, Q. Ma, Q. Lu, J. Chen, X. Zhang, Z. Zhang, B. Li, B. Chen, Y. Zong, H. Zhang, *Adv. Mater.* **2017**, *29*, 1700102.

[94] X. Zhang, P. Zhang, C. Chen, J. Zhang, G. Yang, L. Zheng, J. Zhang, B. Han, *Green Chem.* **2019**, *21*, 54.

[95] Z. X. Low, J. F. Yao, L. Qi, M. He, Z. Y. Wang, A. K. Suresh, J. Bellare, H. T. Wang, *Cryst. Growth Des.* **2014**, *14*, 6589.

[96] J. Lee, J. C. Park, H. Song, *Adv. Mater.* **2008**, *20*, 1523.

[97] F. Ke, J. F. Zhu, L. G. Qiu, X. Jiang, *Chem. Commun.* **2013**, *49*, 1267.

[98] D. Zhu, C. Guo, J. Liu, L. Wang, Y. Du, S.-Z. Qiao, *Chem. Commun.* **2017**, *53*, 10906.

[99] R. Dong, Z. Zheng, D. C. Tranca, J. Zhang, N. Chandrasekhar, S. Liu, X. Zhuang, G. Seifert, X. Feng, *Chem. – Eur. J.* **2017**, *23*, 2255.

[100] G. Hai, X. Jia, K. Zhang, X. Liu, Z. Wu, G. Wang, *Nano Energy* **2018**, *44*, 345.

[101] K. Rui, G. Zhao, Y. Chen, Y. Lin, Q. Zhou, J. Chen, J. Zhu, W. Sun, W. Huang, S. X. Dou, *Adv. Funct. Mater.* **2018**, *28*, 1801554.

[102] X. Jia, Y. Yao, J. Zhao, Y. Gao, Z. Luo, P. Du, *J. Mater. Chem. A* **2018**, *6*, 1188.

[103] Y. Zhao, L. Jiang, L. Shangguan, L. Mi, A. Liu, S. Liu, *J. Mater. Chem. A* **2018**, *6*, 2828.

[104] X. Wei, S. Wang, Z. Hua, L. Chen, J. Shi, *ACS Appl. Mater. Interfaces* **2018**, *10*, 25422.

[105] M. W. Louie, A. T. Bell, *J. Am. Chem. Soc.* **2013**, *135*, 12329.

[106] K. Fan, H. Chen, Y. Ji, H. Huang, P. M. Claesson, Q. Daniel, B. Philippe, H. Rensmo, F. Li, Y. Luo, *Nat. Commun.* **2016**, *7*, 11981.

[107] D. K. Dogutan, R. McGuire, D. G. Nocera, *J. Am. Chem. Soc.* **2011**, *133*, 9178.

[108] H. X. Jia, Z. J. Sun, D. C. Jiang, P. W. Du, *Chem. Mater.* **2015**, *27*, 4586.

[109] J. J. Concepcion, J. W. Jurss, P. G. Hoertz, T. J. Meyer, *Angew. Chem., Int. Ed.* **2009**, *48*, 9473.

[110] F. Li, B. B. Zhang, X. N. Li, Y. Jiang, L. Chen, Y. Q. Li, L. C. Sun, *Angew. Chem., Int. Ed.* **2011**, *50*, 12276.

[111] Y. Ji, H. Dong, C. Liu, Y. Li, *Nanoscale* **2019**, *11*, 454.

[112] W. Shi, L. Cao, H. Zhang, X. Zhou, B. An, Z. Lin, R. Dai, J. Li, C. Wang, W. Lin, *Angew. Chem., Int. Ed.* **2017**, *56*, 9704.

[113] R. Xu, T. Drake, G. Lan, W. Lin, *Chem. – Eur. J.* **2018**, *24*, 15772.

[114] R. Xu, Z. Cai, G. Lan, W. Lin, *Inorg. Chem.* **2018**, *57*, 10489.

[115] L. Ye, Y. Gao, S. Cao, H. Chen, Y. Yao, J. Hou, L. Sun, *Appl. Catal., B* **2018**, *227*, 54.

[116] T. He, B. Ni, S. Zhang, Y. Gong, H. Wang, L. Gu, J. Zhuang, W. Hu, X. Wang, *Small* **2018**, *14*, 1703929.

1900617 (40 of 40)

ADVANCED MATERIALS

Reprint Order Form 2019
- please return with your proofs -

Manuscript No. _____

Please send me and bill me for

☐ no. of **reprints** via ☐ airmail (+ 25 Euro)
☐ surface mail

☐ no. of **copies of this issue**
(1 copy: 28 Euro)
via ☐ airmail (+ 25 Euro)
☐ surface mail

☐ **high-resolution PDF file** (330 Euro).
My e-mail address:

_____

Please note: It is not permitted to present the PDF file on
the internet or on company homepages

★**Special Offer**★ If you order 200 or more reprints you
will get a PDF file for half price.

Information regarding VAT
Please note that from German sales tax point of view, the charge for
Reprints, Issues or Posters is considered as **"supply of goods"** and
therefore, in general, such delivery is a subject to German sales tax. However,
this regulation has no impact on customers located outside of the
European Union. Deliveries to customers outside the Community are
automatically tax-exempt. Deliveries within the Community to institutional
customers outside of Germany are exempted from the German tax (VAT)
only if the customer provides the supplier with his/her VAT number.
The VAT number (value added tax identification number) is a tax registration
number used in the countries of the European Union to identify corporate
entities doing business there. It starts with a country code (e.g. FR for
France, GB for Great Britain) and follows by numbers.

Cover Posters

Posters are available of all the published covers and
frontispieces in two sizes

☐ DIN A2 42 x 60 cm / 17 x 24in (one copy: **39 Euro**)
☐ DIN A1 60 x 84 cm / 24 x 33in (one copy: **49 Euro**)

Postage for shipping posters overseas by airmail:
+ 25 Euro

Postage for shipping posters within Europe by surface mail:
+ 15 Euro

Mail reprints /cover posters / copies of the issue to:

_____
_____
_____
_____
_____

Invoice address:

_____
_____
_____
_____
_____

_____
Date, Signature **Stamp**

VAT no.: _____
(institutes / companies in EU countries only)

Purchase Order No.: _____

Credit Card Payment

VISA, MasterCard, AMERICAN EXPRESS
Please use the Credit Card Token Generator located at the
website below to create a token for secure payment. The token
will be used instead of your credit card number.

Credit Card Token Generator:
https://www.wiley-vch.de/editorial_production/index.php

Please transfer your token number to the space below.

Credit Card Token Number:

Price list for reprints (The prices include mailing and handling charges. All Wiley-VCH prices are exclusive of VAT)

No. of pages	Price (in Euro) for orders of					
	50 copies	100 copies	150 copies	200 copies	300 copies	500 copies
1-4	345	395	425	445	548	752
5-8	490	573	608	636	784	1077
9-12	640	739	786	824	1016	1396
13-16	780	900	958	1004	1237	1701
17-20	930	1070	1138	1196	1489	2022
for every additional 4 pages	147	169	175	188	231	315

★ **Special Offer** ★ If you order 200 or more reprints you will get a PDF file for half price.

WILEY-VCH